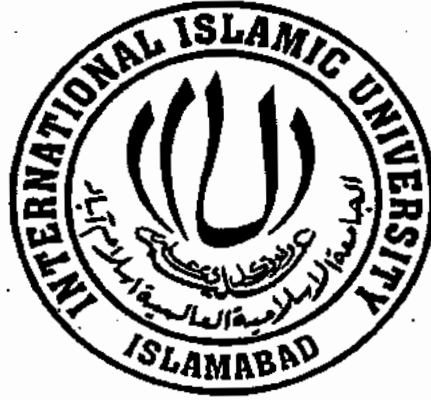


**Synthetic Aperture Radar Based Imaging System
using L1/L5 Reflected GPS Signals**



By

Tahir Saleem

Reg. No. 41-FET/PHDEE/F10

Supervised By

Dr. Mohammad Usman

Co-Supervisor

Dr. Ihsan ul Haq

A dissertation submitted to I.I.U. in partial fulfillment of
the requirements for the degree of

DOCTOR OF PHILOSOPHY

**Department of Electrical Engineering
Faculty of Engineering and Technology
INTERNATIONAL ISLAMIC UNIVERSITY
ISLAMABAD**

2018



Accession No TH20528

PID

623.893

TAS

1. Thesis
2. GNSS
3. Direct global navigation
4. Satellite system
5. GPS signals

Copyright © 2018 by Tahir Saleem

All rights reserved. No part of the material protected by this copyright notice may be reproduced or utilized in any form or by any means, electronic or mechanical, including photocopying, recording or by any information storage and retrieval system, without the permission from the author.

DEDICATED TO
My Loving Parents,
Wife, Kids,
Sisters and Brothers

CERTIFICATE OF APPROVAL

Title of Thesis: Synthetic Aperture Radar based Imaging System using L1/L5 reflected GPS signals

Name of Student: Tahir Saleem

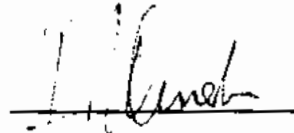
Registration No: 41-FET/PHDEE/F10

Accepted by the Department of Electrical Engineering, Faculty of Engineering and Technology, International Islamic University, Islamabad, in partial fulfillment of the requirements for the Doctor of Philosophy degree in Electronic Engineering.

Viva voce committee:

Prof. Dr. Ijaz Mansoor Qureshi (External Examiner-I)

Department of Electrical Engineering
Air University, Islamabad,



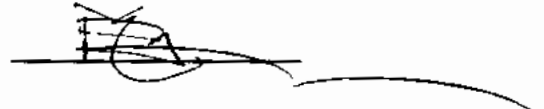
Dr. Rab Nawaz (External Examiner-II)

Principal Scientist NESCOM, Islamabad.



Prof. Dr. Muhammad Amir (Internal Examiner)

Dean, FET, IIU, Islamabad, Pakistan.



Dr. Mohammad Usman (Supervisor)

Adjunct Faculty Member,
Department of Electrical Engineering,
FET, IIU, Islamabad, Pakistan.



Dr. Ihsan ul Haq (Co-Supervisor)

Asst. Professor,
Department of Electrical Engineering,
FET, IIU, Islamabad, Pakistan.



Dr. Suheel Abdullah

Chairman,
Department of Electrical Engineering,
FET, IIU, Islamabad, Pakistan.



ABSTRACT

Direct Global Navigation Satellite System (GNSS) signals are mainly used for navigation and positioning purposes by a diverse set of users. However, this research employs a method for utilizing reflected GNSS signals to form an image of targets within a region of interest. The principle is based upon a type of bistatic synthetic aperture radar (SAR) in which a matched filter technique is utilized to perform the image reconstruction. The most promising non-cooperative transmitter, among the existing GNSS, for the practical SAR applications is: Global Positioning System (GPS) specially its newly introduced L5 signal. The method presented in this thesis relies upon the fact that each component of the received signal resulting from a reflection of an individual target is subjected to a unique chirp. A major challenge is the appalling signal to noise ratio associated with the received reflected GPS signals. Another difficulty was the masking of the reflected signals by power in the tails of the autocorrelation function of the direct signals which cannot be totally suppressed. Moreover, the reconstruction method resulted in an undesirable point spread function (PSF) which degraded the reconstructed image.

The entire GPS signal generation and image reconstruction process has been simulated as faithfully as possible within the limitations of the available computational resources. The smeared image obtained due to poor quality PSF was improved by means of a Wiener filter and Particle Swarm Optimization based deconvolution method.

There can be three different types of imaging scenarios based on the location of GPS receiver and the source that generates the requisite change in geometry. The imaging hardware can be kept airborne, placed on a ground vehicle or simply remain static. Whereas, all three scenarios have been simulated, an imaging system based on a static receiver has practically demonstrated with the successful identification of 0.5 m^2 spherical target. The necessary change in synthetic aperture is provided by the orbiting GPS satellite by integrating the signal over a longer period of time.

LIST OF PUBLICATIONS AND SUBMISSIONS

- [1] **Saleem T**, Usman M, Elahi A, Gul N. "Simulation and Performance Evaluations of the New GPS L5 and L1 Signals". (*Wireless communication and Mobile computing, Hindawi Publishing Corporation*) Vol. 2017, Article ID 7492703, 4 pages, <https://doi.org/10.1155/2017/7492703> (IF = 1.899)
- [2] **Saleem T**, Usman M. "Analysis and Mitigation of Tropospheric Error Effect on GPS positioning using Real GPS Data". (*International Journal of Electronics and Electrical Engineering*) Vol.2, No. 3 page 249-253, 2014).
- [3] **Saleem T**, Usman M, Armitage DW. "Design, Assembly and Testing of a High Gain LHCP Helical Antenna for Reception of Reflected GPS Signals". (*Journal of Progress in Electromagnetic Research (PIERC)*) Vol. 44, page 161-174, 2013) (ISI indexed)
- [4] Elahi A, Qureshi IM, Zaman F, Gul N, **Saleem T**. "Suppression of Mutual Interference in Non-Contiguous Orthogonal Frequency Division Multiplexing Based Cognitive Radio Systems" *Wireless communication and Mobile computing, Hindawi Publishing Corporation* (IF = 1.899)
- [5] **Saleem T**, Bahadar K, Usman M. "Initial Design and Analysis of Indigenous Synthetic Aperture Radar (SAR) Demonstrator" *IEEE 14th International Bhurban Conference on Applied Sciences and Technology (IBCAST), 2017. (Accepted)*
- [6] Gul N, Naveed A, Elahi A, **Saleem T**, Qureshi IM. "A combination of double sided neighbor distance and genetic algorithm in cooperative spectrum sensing against malicious users". *Proceedings of IEEE 14th International Bhurban Conference on Applied Sciences and Technology (IBCAST), 2017.*
- [7] Elahi A, **Saleem T**, Qureshi IM, Gul N. "Application of Differential and Cuckoo Search Algorithms in Reduction of sidelobes". *Proceedings of 19th International. IEEE Multi-topic Conference, 2016. (INMIC 2016)*
- [8] Naqvi A, **Saleem T**, Rehan W, Elahi A. " A Novel Model for Face Recognition" *Proceedings of The Eleventh International Conference on Pattern Recognition and Information Processing. May 18-20, 2011 Minsk, Belarus, pp. 84-87.*

SUBMITTED PAPERS:

- [1] **Saleem T**, Usman M, Haq I, Zaman F, Elahi A. “Design, Assembly and Testing of a High Gain LHCP Helical Antenna Array for Reception of Reflected GPS Signals”
International Journal of IEEE Access (Submitted, IF = 3.224)

- [2] **Saleem T**, Usman M, Haq I, Uddin I, Khan H, “Experimental demonstration of BSAR imaging using new L5 GPS signal”
Wiley, Intl. Journal of Satellite Communication and Networking (Submitted, IF = 1.079)

- [3] **Saleem T**, Usman M, Haq I, Uddin I, Daraz A. “De-convolution of SAR images using Heuristics Techniques”
Elsevier, Journal of Swarm and Evolutionary Computation (Submitted, IF = 3.893)

- [4] **Saleem T**, Usman M, Uddin I, Khan MA. “Results of an Imaging System Utilizing Reflected GPS Signals with Stationary GPS Receiver”
Springer, Intl Journal of Wireless Personal Communications (Submitted, IF = 0.951)

ACKNOWLEDGEMENTS

First and foremost, I humbly thank Allah (Subhanahu Wa Ta'ala) who has given me the courage, strength and determination to undertake this final step towards the pinnacle of my academic career.

I am truly grateful to my supervisor Dr. Mohammad Usman, whose inspiration, ideas and efforts make it possible for me to complete my higher studies. His sincere spirit of cooperation, his positive attitude and understanding were always there to help me.

I am also thankful to Dr. Ihsan ul Haq for his valuable suggestions as co-supervisor. I would like to acknowledge the support of Higher Education commission of Pakistan for awarding me Indigenous Scholarship during my MS and PhD studies. It was a great support from Higher Education commission of Pakistan. I am also thankful to administration at department as well as at university level for their kind support.

My deepest thanks go to my father, mother, sisters and brothers for their love and support throughout my life. I am also very thankful to my wife for her patience, encouragement and prayers during every stage of my PhD degree, and to our kids, Safwan and Zayyan for bringing so much joy into our life. Finally, I would like to thank my research fellow at PhD lab especially Atif Elahi, Amil Daraz, Hayat Ullah, Shah Fahad and other PhD scholars for giving me company and keeping the atmosphere alive.

(Tahir Saleem)

ACKNOWLEDGEMENTS

First and foremost, I humbly thank Allah (Subhanahu Wa Ta'ala) who has given me the courage, strength and determination to undertake this final step towards the pinnacle of my academic career.

I am truly grateful to my supervisor Dr. Mohammad Usman, whose inspiration, ideas and efforts make it possible for me to complete my higher studies. His sincere spirit of cooperation, his positive attitude and understanding were always there to help me.

I am also thankful to Dr. Ihsan ul Haq for his valuable suggestions as co-supervisor. I would like to acknowledge the support of Higher Education commission of Pakistan for awarding me Indigenous Scholarship during my MS and PhD studies. It was a great support from Higher Education commission of Pakistan. I am also thankful to administration at department as well as at university level for their kind support.

My deepest thanks go to my father, mother, sisters and brothers for their love and support throughout my life. I am also very thankful to my wife for her patience, encouragement and prayers during every stage of my PhD degree, and to our kids, Safwan and Zayyan for bringing so much joy into our life. Finally, I would like to thank my research fellow at PhD lab especially Atif Elahi, Amil Daraz, Hayat Ullah, Shah Fahad and other PhD scholars for giving me company and keeping the atmosphere alive.

(Tahir Saleem)

Table of Contents

ABSTRACT	v
LIST OF PUBLICATIONS AND SUBMISSIONS	vi
ACKNOWLEDGEMENTS	viii
LIST OF TABLES	xiv
LIST OF FIGURES	xv
LIST OF ABBREVIATIONS	xviii
Chapter 1	1
Introduction	1
1.1 Background.....	1
1.2 Objective and Research Contributions.....	2
1.3 Organization of the Thesis.....	2
Chapter 2	4
Basic Theory of SAR (Synthetic Aperture Radar)	4
2.1 Brief History of SAR	4
2.2 Concept of SAR (Synthetic Aperture Radar)	5
2.3 Types of SAR	5
2.3.1 Mono-static SAR	6
2.3.2 Bistatic SAR (BSAR)	6
2.3.3 Multistatic SAR	7
2.4 SAR Imaging and Allied concepts.....	7
2.4.1 BSAR Imaging Scenarios.....	10
2.4.2 FM Chirp Signal	13
2.4.3 Matched Filter	13
2.4.4 Doppler Frequency	14
Chapter 3	16

GPS Signals for SAR Application	16
3.1 GNSS (Global Navigation Satellite System) Signal Frequency Bands	16
3.2 General Description of GPS	18
3.3 Elements of GPS	18
3.3.1 Space Segment.....	18
3.3.2 Control Segment.....	19
3.3.3 User Segment.....	19
3.4 Structure of GPS Signals.....	20
3.4.1 Carrier	20
3.4.2 Spreading codes.....	21
3.4.3 Navigation data.....	23
3.5 GPS Signals Modulation	24
3.6 GPS Error sources.....	26
3.6.1 Orbital error.....	27
3.6.2 Satellite clock error.....	28
3.6.3 Ionospheric errors	28
3.6.4 Troposphere error	29
3.6.5 Receiver clock error.....	30
3.6.6 Multipath error.....	30
3.7 Analysis of GPS Signals.....	31
3.7.1 Autocorrelation.....	32
3.7.2 Power Budget Analysis	35
3.7.3 Power Level.....	38
Chapter 4.....	40
Literature Review	40
4.1 Different types of GNSS Remote Sensing	40
4.1.1 Ocean Remote Sensing	40

4.1.2 Hydrology and Vegetation Remote Sensing	43
4.1.3 Cryospheric Remote Sensing	45
4.1.4 Atmospheric Remote Sensing	46
4.2 Initial Research regarding GPS Imaging.....	47
4.3 A Review of Relevant Hardware	52
4.4 Experimental Results for Image Formation	55
4.5 Alternate Source of Signals	57
Chapter 5.....	59
Experimental Imaging Hardware	59
5.1 Hardware Description	60
5.1.1 Design and Development of Antennas	60
5.1.1.1 Basic Design Parameters	62
5.1.1.2 Input Impedance.....	64
5.1.1.3 Gain of the antenna	65
5.1.1.4 Assembly of the Four Elements Antenna Array	67
5.1.1.5 Testing and Gain Measurements.....	68
5.1.1.6 Field Trials.....	69
5.1.2 Front End.....	70
5.1.2.1 Signal Conditioning	72
5.1.2.2 Down Conversion	72
5.1.3 Data Acquisition Card.....	72
5.1.3.1 SdrNav20 Circuit Components.....	73
5.2 Experiment for Data Acquisition	74
Chapter 6.....	80
Simulations and Results.....	80
6.1 Initial Simulation	80
6.2 Detailed Description of the Simulation.....	82

6.2.1 Computation of satellite coordinates	82
6.2.2 C/A Code Generation.....	83
6.2.3 Calculation of signal delay	83
6.2.4 Determination of code offset.....	84
6.2.5 Extraction of the base-band I and Q components.....	86
6.2.6 Attenuation and noise.....	87
6.2.7 Display of image.....	88
6.2.8 Image reconstruction and matched filter processing	89
6.2.9 Simplifications and assumptions	90
6.3 Modifications and Improvements to the Code	90
6.4 Preliminary Results	93
6.4.1 Case I.....	93
6.4.2 Case II	95
6.4.3 Case III.....	95
6.4.4 Case IV.....	96
6.5 Simulation Results for Different Imaging Scenarios	98
6.5.1 Ground vehicle borne (low velocity) receiver.....	98
6.5.2 Results for static receiver simulation.....	101
6.6 Further Simulation for enhancing Resolution	104
6.6.1 Image generation	105
6.6.2 Image restoration	106
6.6.2.1 The Wiener filter.....	108
6.6.2.2 De-convolution using PSO (Particle swarm optimization)	112
6.7 Analysis of GPS Data.....	115
6.7.1 Acquisition and Tracking algorithms.....	116
6.8 Results for Actual GPS Data	120
Chapter 7.....	123

Conclusion and Future Work.....	123
7.1 Conclusion.....	123
7.2 Future Work.....	124
References	126

LIST OF TABLES

Table 2. 1 Spatial Resolution Functional Relationships.....	10
Table 3. 1 Tropospheric Delay on Measured Range	29
Table 3. 2 Summary of GPS errors	31
Table 3. 3 L1 and L5 Comparison Parameters	39
Table 5. 1 Comparison of Different Antennas	62
Table 5. 2 Design Parameters	63
Table 5. 3 Main Components of SdrNav20.....	73
Table 6. 1 Simulation Parameters.....	93
Table 6. 2 Optimum time for static receiver simulation.....	101
Table 6. 3 Performance evaluation of Restoration techniques	114

LIST OF FIGURES

Figure 2. 1 The concept of synthetic aperture operation.....	5
Figure 2. 2 Mono-static SAR Configuration.....	6
Figure 2. 3 Bistatic SAR configuration.....	6
Figure 2. 4 Multistatic SAR configuration.....	7
Figure 2. 5 Resolution of target.....	8
Figure 2. 6 Airborne receiver-Scenario.....	11
Figure 2. 7 Ground vehicle based receiver-Scenario	11
Figure 2. 8 Stationary receiver-Scenario.....	12
Figure 2. 9 Using the process of correlation to compress the received chirp.....	14
Figure 3. 1 GNSS Satellites Frequency Bands.....	17
Figure 3. 2 Functional Elements of GPS.....	20
Figure 3. 3 Satellites signal Generation process	21
Figure 3. 4 Generation of L ₁ C/A Codes.....	22
Figure 3. 5 Generation of L ₅ C/A Codes.....	22
Figure 3. 6 Navigation Data Format.....	23
Figure 3. 7 Block Diagram describing L ₁ and L ₂ Signal Generation.....	24
Figure 3. 8 Block Diagram describing L ₅ Signal Generation.....	25
Figure 3. 9 (a) L ₁ Autocorrelation Function (b) L ₅ Autocorrelation Function.....	33
Figure 3. 10 The Autocorrelation of L ₁ signal.....	34
Figure 3. 11 The Autocorrelation of L ₅ signal.....	34
Figure 3. 12 SNR Vs Range plot without processing gain.....	36
Figure 3. 13 SNR Vs Range plot with processing gain.....	36
Figure 3. 14 Power spectral densities of L ₁ and L ₅	38
Figure 4. 1 Block diagram of the device	55
Figure 4. 2 SS-BSAR image obtained using real data	57

Figure 5. 1 Imaging Hardware Functional Block Diagram.....	59
Figure 5. 2 Simplified Antenna Diagram.....	63
Figure 5. 3 Gain plot for a single 8 turn element Helical Antenna	66
Figure 5. 4 Final Antenna Array	68
Figure 5. 5 VNA based antenna array plot (a) S_{11} (b) VSWR	68
Figure 5. 6 Proposed Imaging System	69
Figure 5. 7 Acquisition plot (a) Zenith antenna (b) Nadir antenna	70
Figure 5. 8 Correlation plot (a) Zenith antenna (b) Nadir antenna.....	71
Figure 5. 9 Front End Block Diagram.....	71
Figure 5. 10 Dual Front End SdrNav20 Data Acquisition Card	73
Figure 5. 11 Set up for detection of reflected GPS signals	74
Figure 5. 12 Comparison of acquisition plot (a) (acquisition time of 4 ms) for RHCP antenna (b) (acquisition time of 200 ms) for LHCP antenna	76
Figure 5. 13 Comparison of direct and reflected GPS signals for (a) 50 m (b) 4 m (round trip distances).....	77
Figure 5. 14 Comparison of acquisition plot for acquisition time of (a) 1000 and (b) 2000 ms.....	78
Figure 6. 1 Structure of Simulation.....	81
Figure 6. 2 Detailed flow chart of the Simulation.....	85
Figure 6. 3 Code offset.....	84
Figure 6. 4 Candidate position for the target.....	88
Figure 6. 5 Block diagram of the modified reconstruction engine.....	92
Figure 6. 6 Integration-Time 0.1 sec (without noise).....	94
Figure 6. 7 Integration-Time 0.1 sec (with 16 dB noise).....	94
Figure 6. 8 Integration-Time 0.2 sec (with 16 dB noise).....	95
Figure 6. 9 Comparison of diagrams for Integration-time 0.1 sec & Target speed (a) 10 m/s (b) 20 m/s (c) 100 m/s	96

Figure 6. 10 Comparison of results for receiver velocity of (a) 20 m/s (b) 5 m/s (c) 3 m/s and (d) 2 m/s	99
Figure 6. 11 Comparison of results for receiver position error of (a) 0.01 m (b) 0.05 m (c) 0.07 m (d) 0.1 m.....	100
Figure 6. 12 Simulation results for 7200 seconds (a) Original Image (b) Deconvolved image.....	103
Figure 6. 13 Simulation results for 7200 seconds (a) Original Image (b) PSF	103
Figure 6. 14 Comparison of results for T_s of (a) 2400 s (c) 1000 s (d) 300 s	104
Figure 6. 15 (a) Raw reconstructed image (b) Target area enlarged.....	106
Figure 6. 16 (a) Point spread function (PSF) (b) Image enlarged around centre	107
Figure 6. 17 The degradation process	108
Figure 6. 18 Comparison of results for T_s of (a) 4500 s (b) 2400 s	111
Figure 6. 19 (a) Reconstructed image (b) De-convolved Image	111
Figure 6. 20 PSO and SVD System Model Flowchart.....	113
Figure 6. 21 (a) De-convolved Image after PSO (b) Restored image after SVD.....	114
Figure 6. 22 Comparison of time and frequency domain plots (a) Actual GPS data (b) Simulated GPS data.....	116
Figure 6. 23 (a) Acquisition plot for PRN 31 for one ms (b) Correlation versus delay plot for PRN 31 (one ms of simulated GPS data).....	117
Figure 6. 24 Acquisition plots for PRN 2 with time (a) 2 ms (b) 20 ms	118
Figure 6. 25 Acquisition diagram for actual GPS data	119
Figure 6. 26 Satellite polar plot, showing the visible satellites.....	120
Figure 6. 27 Comparison of image obtained by reconstructing 2400 sec of (a) Actual signal (b) Simulated signal.....	121

LIST OF ABBREVIATIONS

ADC	Analogue to Digital Converter
BPSK	Binary Phase Shift Keying
BR	Bi-static Radar
BSAR	Bi-static Synthetic Aperture Radar
C/A	Clear / Acquisition
CDMA	Code Division Multiple Access
CPLD	Complex Programmable Logic Device
DFT	Discrete Fourier Transform
DLL	Delay Lock Loop
DPI	Direct Path Interference
DSSS	Direct Sequence Spread Spectrum
ECEF	Earth Centered Earth Fixed
FFT	Fast Fourier Transform
FM	Frequency Modulation
GA	Genetic Algorithm
GAF	Generalized Ambiguity Function
GNSS	Global Navigation Satellite Systems
GPS	Global Positioning System
GUI	Graphic User Interface
I	In Phase
ID	Identification
IF	Intermediate Frequency
IFFT	Inverse Fast Fourier Transform
LEO	Low Earth Orbit

LO	Local Oscillator
ms	Millisecond
NAV	Navigation
NCT	Non Cooperative Transmitter
OCS	Operational Control Segment
P Code	Precision Code
PCB	Printed Circuit Board
PLL	Phase Locked Loop
PRN	Pseudorandom Number
PSD	Power Spectral Density
PSO	Particle Swarm Optimization
Q	Quadrature
RCS	Radar Cross section
RF	Radio Frequency
RHCP	Right Hand Circularly Polarized
SAR	Synthetic Aperture Radar
SMOS	Soil moisture and ocean salinity
SMAP	Soil Moisture Active and Passive mission
SNR	Signal to Noise Ratio
SPS	Standard Positioning Services
SRAM	Static Random Access Memory
SS-BSAR	Space Surface Bi-static Synthetic Aperture Radar
SVD	Singular Value Decomposition
TCXO	Temperature Compensated Crystal Oscillator

TOW

Time of week

WGS - 84

World Geodetic System

Chapter 1

Introduction

1.1 Background

The GPS is United States (US) space based global navigation satellite system maintained by Defense department. GPS is mainly used for positioning and navigation purposes. A constellation of GPS satellites transmit signals which are received and processed by GPS receivers before displaying the position of the user. These satellites broadcast signals to the surface of earth which strike different objects and bounce back to receiver in multi-path fashion. GPS receivers positional capability is highly degraded by these reflected signals, hence termed as unwanted signals [1] . However, potential information's about the reflecting objects/surfaces are carried by these reflected signals [2]. This characteristic of the reflected signals makes it the best choice for remote sensing and imaging purpose [3], [4].

Due to potential military and civilian applications, analysis of GPS reflected signals has recently gained a lot of attention. Sea ice thickness, land soil moisture, wind speed and direction of sea surface, ocean significant wave height etc. are some of the parameters which can be measured with help of reflected signals [5]. In fact, based on Synthetic Aperture Radar principle in combination with digital signal processing of the direct and reflected GPS signals image of the target area can be processed with recognizable features resolution.

1.2 Objective and Research Contributions

This research endeavor focuses on SAR based imaging system with GPS as transmitter of opportunity. The main purpose of the dissertation is to investigate in detail manner the feasibility of the imaging system and verify its performance/ability to resolve a target in the area of interest. The ultimate aim is to develop suitable and efficient image reconstruction techniques, along with design and assembly of required data acquisition card (hardware).

Following is the summary of contributions made during the research phase.

1. Recently added new L5 GPS signal (by the US) has been proposed in order to confirm the remote sensing capability of the imaging system. After thorough performance evaluation during the simulation, it is concluded that L5 has superior detection characteristics i-e greater bandwidth, high correlation peaks, better SNR as compared to other GPS signals.
2. For acquisition of low power reflected GPS signals Left Hand Circularly polarized (LHCP) antenna was designed. For further better results and higher antenna gain LHCP helix antenna array has been proposed with compact design.
3. Finally, in the deconvolution phase of reconstruction of the target image we applied Wiener filter and Particle Swarm Optimization (PSO) heuristic technique by using our proposed fitness function. The effectiveness of the algorithm is checked by considering different imaging scenarios. Simulations show that the proposed method performs well when compared with existing techniques.

1.3 Thesis Organization

The dissertation report consists of seven chapters. Following few paragraphs gives glimpse of the contents covered in the chapters.

Chapter 2 highlights the basic concept of radar & synthetic aperture radar. It also presents in brief some important concepts like matched filters, ambiguity functions, FM chirp signals etc.

For understanding of GPS based SAR imaging it is imperative to have knowledge about GPS basics components: types of signals and its structure, auto and cross correlation, navigation message etc. All these concepts are covered in chapter 3.

Chapter 4 is reserved for: in order to broaden the academic perspective and obtain knowledge of the contemporary research activities in GNSS based remote sensing and imaging, some aspects that are pertinent to the research topic have been reviewed, discussed and analyzed.

Chapter 5 is dedicated for furnishing some details regarding the hardware, which has been assembled for the practical realization of the imaging system.

Chapter 6 presents the detailed simulation which was carried out for confirmation of the idea, presented in thesis i-e by utilizing SAR concept in combination with reflected & direct GPS signals correlation characteristic it is feasible to image target area. Next it presents the results obtained during the course of Matlab® simulations and experiments performed to acquire actual GPS data. The chapter ends with results comparison, findings discussion and highlighted shortcomings.

The final chapter 7 summarizes the conclusion, highlights further system improvement steps like system resolution, image quality, computational efficiency etc which can be taken in future research.

Chapter 2

Basic Theory of SAR (Synthetic Aperture Radar)

This chapter provides the technical basis for understanding the working principle of SAR operation. Brief historical look and evolution of SAR is presented at the beginning of the chapter. Next idea of aperture synthesis and working theory of SAR is discussed. At the end formation of SAR image, along with its basic properties are elaborated.

2.1 Brief History of SAR

Before investigation of SAR imaging reconstruction, it is imperative to have a look about SAR evolution. The origin of the SAR concept was introduced and demonstrated by Carl Wiley in 1951. Since then, SAR has undergone several significant technology phases to meet various industrial and military applications.

The use of the wavefront reconstruction theory in SAR imaging was recognized during the late 1950s and early 1960s, which is now known as Doppler Beam Sharpening (DBS) algorithm. However, due to the lack of advanced computing machines and digital signal processing techniques at that time, the reconstruction theory could not achieve its intended purpose.

In 1970s, the first digital processing method for SAR image formation was developed which significantly improved the image resolution. The first SAR satellite SEASAT, which was introduced by NASA started its transmission in 1978. SEASAT began the development of space based SAR. Different countries like Russia, Canada and Japan etc. have launched their SAR satellites in space which still continues to this day. By utilizing the various collection modes characteristic of SAR, in future SAR systems will provide enhanced capabilities [6].

2.2 Concept of SAR

Synthetic aperture radar works on the concept of generating an effective long antenna by signal processing means rather than by the actual use of a long physical antenna. Only a single element of the antenna is utilized along with platform motion (Aircraft/Satellite) to move that element through successive element position. At each position signal is broadcast, which travel to target area where the antenna beam illuminates targets and bounced back signals (echoes) are placed in storage after collection through the same antenna. This process is suggested in Figure 2.1. The SAR system preserves both the amplitude and phase history of echoes at each place. It then constructs an image through signal processing by adding responses of all the reflected signals from targets.

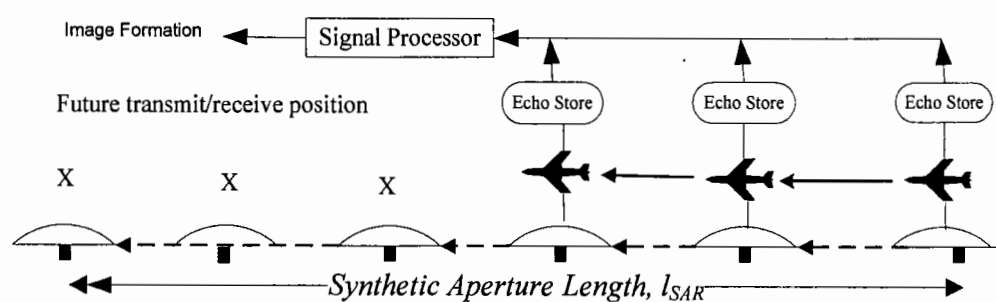


Figure 2. 1The concept of synthetic aperture operation

2.3 Types of SAR

The SAR system components (transmitter and receiver) can be placed in different ways. This topological configuration is defined by the manner in which the transmitter and receiver of the system reacts as shown in Figures 2.2-2.4.

2.3.1 Mono-static SAR

In this configuration the transmitter (T_x) and receiver (R_x) are arranged in same location, so that the same antenna can be used for transmission as well as reception of the signal, as depicted in Figure 2.2.

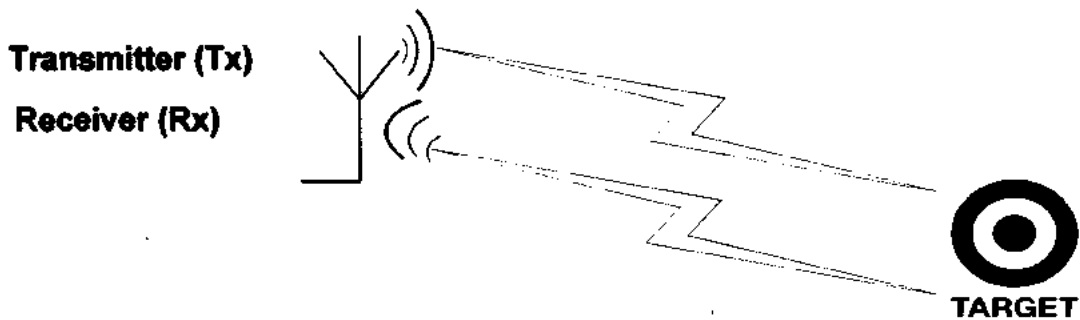


Figure 2. 2 Mono-static SAR Configuration

2.3.2 Bistatic SAR (B-SAR)

In this kind of SAR configuration, the transmitter and receiver are placed at different location separated by some distance, as shown in Figure 2.3. Any of the three components i-e (transmitter, receiver and target) may be moving or static and placed in space, on the earth surface or kept airborne. This leads to different imaging scenarios which are elaborated in detail in section (2.4.1).

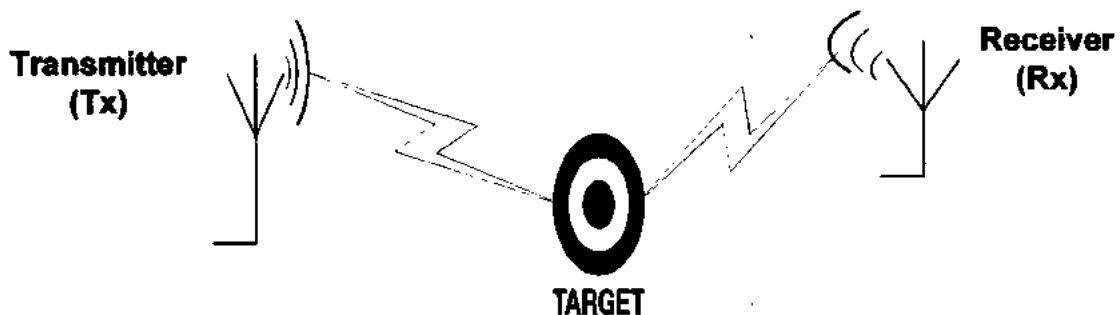


Figure 2. 3 Bistatic SAR configuration

2.3.3 Multistatic SAR

The multistatic radar depicted in Figure. 2.4 normally have multiple cooperative elements at the receiver end and a single transmitter. Multi-static radars in some cases uses more than one transmitter.

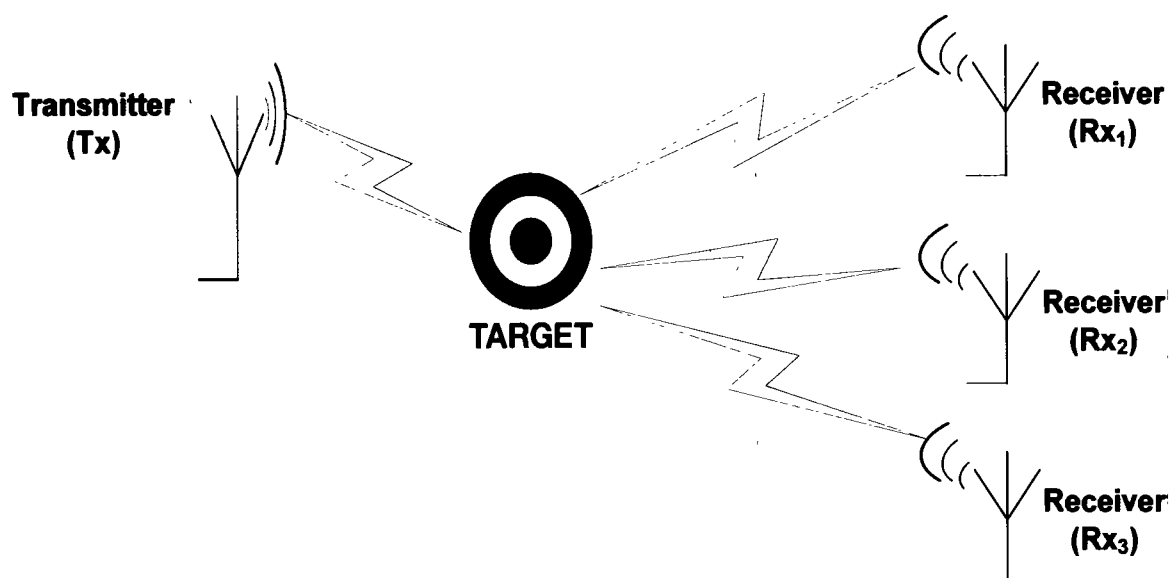


Figure 2. 4 Multistatic SAR configuration

2.4 SAR Imaging and allied concepts

A SAR system normally produces two dimensional images of target area. The image must provide adequate information so that the underlying targets which are being imaged by the system may be resolved in the area of interest. Measuring distance (line of sight) between target and transmitter is termed as range (cross-track) dimension. Perpendicular to the range, dimension of the SAR image is known as azimuth (along-track) depicted in Figure 2.5. In radar literature the ability of the radar to detect and distinguish closely situated targets is called its resolution. Range or cross track resolution of typical radar can be mathematically expressed as [7]:

$$\text{Range Resolution } (R_r) = \frac{c\tau}{2} \quad (2.1)$$

Here τ represents width of the employed pulse and c is light speed. Sufficient range-resolution for radar is relatively easy to achieve by using pulse frequency modulated (FM) chirp signal discussed in section 2.4.2. It is worth mentioning that both SAR and common radar achieve their range resolution as given by equation (2.1). Now we move to check how radar achieves the azimuth resolution. Figure 2.5 illustrates the cross-range (azimuth) resolution for real-beam radar. The antenna of the transmitter scans in azimuth angle. It has an azimuth beam-width of θ_{az} radians; thus at a range R_o , the azimuth resolution can be approximated by following equation:

$$\text{Azimuth Resolution } (R_{az}) = R_o\theta_{az} \quad (2.2)$$

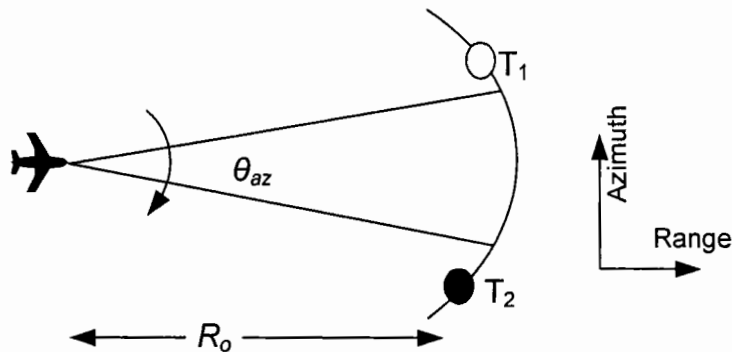


Figure 2. 5 Resolution of target

From antenna theory, the beamwidth of a conventional antenna is given by:

$$\theta_{az} = \frac{\lambda}{l_{az}} \quad (2.3)$$

where l_{az} = antenna width in azimuth direction. Combining equations 2.2 and 2.3 gives general radar azimuth resolution as:

$$R_{az} = \frac{R_o \lambda}{l_{az}} \quad (2.4)$$

Equation (2.4) suggests that in order to get better azimuth (R_{az}) resolution value of the following three options can be opted:

- Using higher frequency signals or short wavelength pulse (λ)
- Increasing length of the antenna in azimuth direction (l_{az})
- Decreasing the target range (R_o)

But none of these options are very effective and seem impractical in case of space or airborne system. So the resolution indicated by equation (2.4) is not acceptable for imaging purposes.

Hence, to achieve reasonable azimuth resolution relatively efficient alternate method is required. The adopted technique/solution is based on SAR concept, which is explained previously in section 2.1 of this chapter. The maximum possible along-track (azimuth) resolution which can be obtained by utilizing SAR principle is given by the following expression [7]:

$$R_{SAR} = \frac{l_{SAR}}{2} \quad (2.5)$$

Where l_{SAR} = synthetic aperture length, produced as result of translating the single antenna element along the flight path as can be seen from Figure. 2.1. Equation (2.5) gives remarkable results and show that R_{SAR} (azimuth resolution) is not effected by: platform altitude, operating wavelength and range (R_o) as compared to R_{az} of equation (2.4). Consequently, this makes SAR a best choice for imaging and remote sensing operations. The relationship between azimuth and range resolution is shown in Table 2.1.

Table 2. 1 Resolution Functional Relationships

Platform	Range Parameter	Azimuth Parameter
SAR	$\left(\frac{c}{2\beta}\right)$	$\frac{\text{Along Track Antenna Length}}{2}$
Radar	$\left(\frac{c}{2\beta}\right)$	$\frac{\text{Along Track Antenna Length}}{\lambda * R_0}$

2.4.1 BSAR Imaging Scenarios

By changing the topological arrangement of the employed receiver, the BSAR configuration leads to three different imaging scenarios.

Case I. Spaceborne transmitter and airborne receiver

This kind of geometry can be understood with help of Figure. 2.6. Where the imaging receiver is mounted on aerial platform. This option is best suited in case of remote sensing of forest change detection, presence of ships etc. Shading, synchronization and Doppler effect due to fast change in geometry and associated possible restriction in airspace are some of the problems of this configuration.

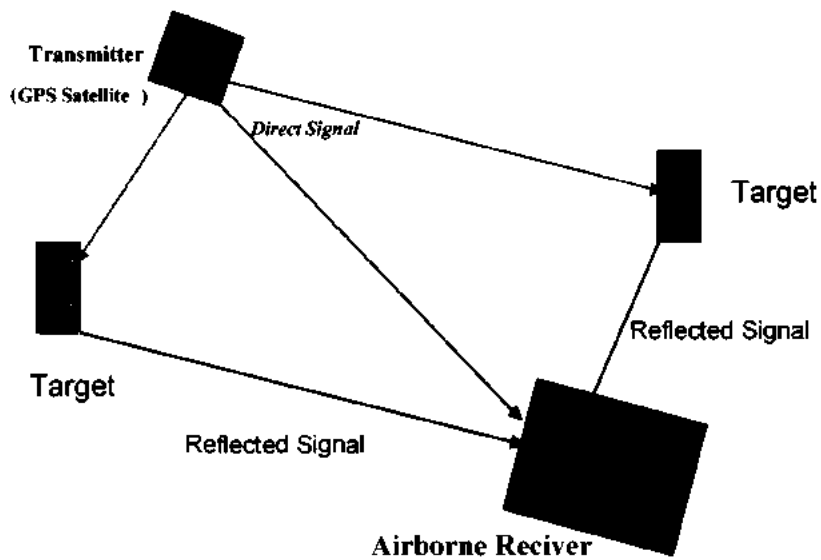


Figure 2. 6 Airborne receiver-Scenario

Case II. Spaceborne transmitter and low speed ground vehicle receiver

In order to eliminate the requirement of airborne receiver and simplify the geometry further, the imaging system can be mounted on a ground vehicle moving with slow speed near to the target. The arrangement is depicted in Figure 2.7.

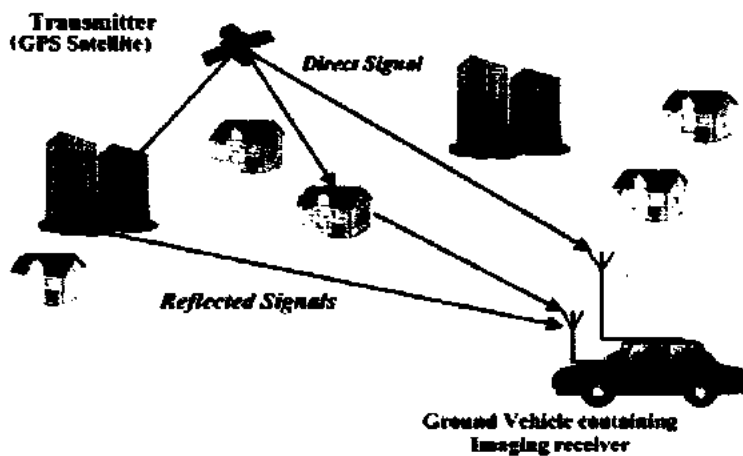


Figure 2. 7 Ground vehicle based receiver-Scenario

However due to the associated logistics issues related to the arrangement of an aerial or terrestrial platform makes these two options unattractive or even unpractical.

Case III. Spaceborne transmitter and Stationery receiver

In this configuration, the receiver works in static mode, on or near the surface of earth. By increasing the integration time for data collection, it is possible to generate an image of the target area using stationery receiver at least theoretically, simplifying more the experimental set up. The synthetic aperture synthesis is provided by the motion of satellite, as shown in Figure. 2.8. This option is best suited for wind speed, sea surface height, landslides and other similar applications.

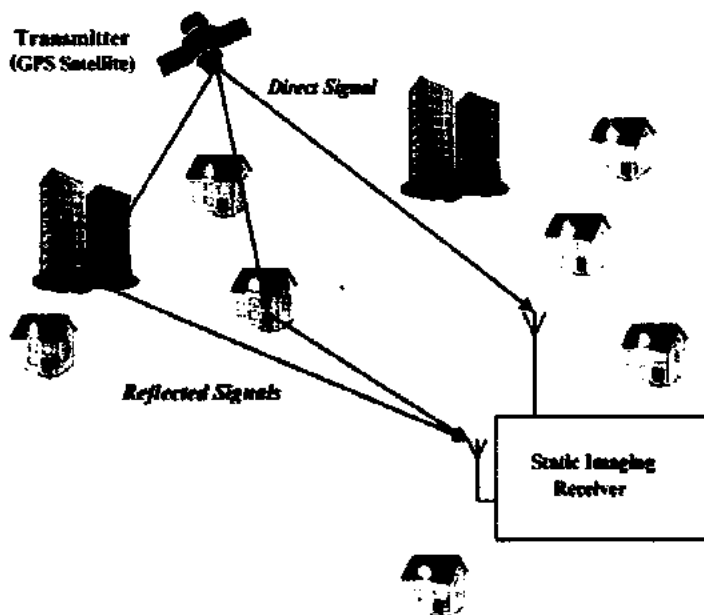


Figure 2. 8 Stationery receiver-Scenario

During the course of current research effort all these different configurations and imaging scenarios have been analyzed and simulated, in a detailed manner with GPS as transmitter of opportunity. After thorough deliberation, based on simulation results and practical constraints, it

was finally decided to perform the experiment for data acquisition with the hardware positioned at a fixed geographical location.

2.4.2 FM Chirp Signal

As mentioned earlier in section (2.4) that sufficient range resolution for radar is relatively easy to achieve by using pulse with short duration. A waveform having effective small duration (greater bandwidth) can be designed using frequency modulation (FM) in combination with matched filtering technique discussed in section (2.4.3), this signal processing technique is called pulse compression. Frequency of the pulse is changed linearly with time. This frequency modulated pulse is known as chirp signal, which can be expressed mathematically as [8]: -

$$s(t) = A \text{rect}\left(\frac{t}{T}\right) \cos\left[\omega_0 t + \frac{\Delta\omega t^2}{2T} + \phi_0\right] \quad (2.6)$$

Here A , ω_0 , T are positive constants, $\Delta\omega$ represents frequency sweep and ϕ_0 is an arbitrary phase angle.

Using the operation of correlation when the chirp signal is received, it is compared with its locally generated replica which results in compressed waveform. The clear centre location in time can be viewed as shown in Figure (2.9), which is unique beneficial property of chirp signals.

2.4.3 Matched Filter

The matched filter derives its name from the fact that its transfer function represented by Equation. (2.8) is proportional to the transmitted signal's spectrum (conjugated). The filter must adjust itself accordingly, if the signal being used/received changes.

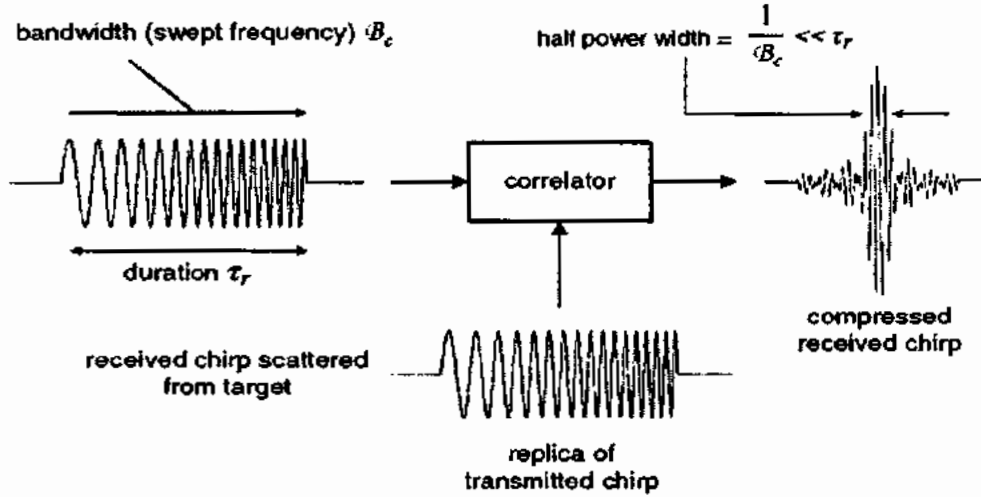


Figure 2. 9 Received chirp signal compression.

Let signal $s(t)$ is transmitted signal then the received pulse $s_r(t)$ can be represented as:

$$s_r(t) = \alpha s(t - \tau_R) \leftrightarrow S_r(\omega) = \alpha S(\omega) e^{-j\omega\tau_R} \quad (2.7)$$

The matched filter output can be computed with following impulse response as:

$$h_{opt}(t) = \frac{2C\alpha}{N_o} s(t_o - \tau_R - t) \leftrightarrow H_{opt}(\omega) = \frac{2C\alpha}{N_o} S^*(\omega) e^{-j\omega(t_o - \tau_R)} \quad (2.8)$$

For a transmitted signal matched filter should be designed in such way so that at its output maximum signal to noise ratio (SNR) can be achieved [9].

2.4.4 Doppler Frequency

The Doppler effect is central to synthetic aperture radar, in which relative motion of the transmitter (GPS satellite in our case) and receiver of the signal has profound affect on transmitted signal frequency. It means the frequency of received signal is different from transmitted signal. This change of frequency is noted as Doppler offset/shift [1]. The values of Doppler shift increases as the transmitter come closer to the receiver and start to decrease as

transmitter goes far away. Generally the Doppler frequency shift can be mathematically expressed as [7]:

$$\omega_d = \frac{d\phi(t)}{dt} \quad (2.9)$$

$$\phi(t) = \frac{2\pi x(t)}{\lambda} \quad (2.10)$$

Putting Equation (2.10) in Equation (2.9) we shall get final formula for Doppler shift as:

$$\omega_d = \frac{2\pi}{\lambda} \frac{dx(t)}{dt} \quad (2.11)$$

Where $x(t)$ is the distance b/w transmitter and receiver at time t .

Both the C/A code and carrier frequency of GPS signal are affected by Doppler frequency shift. However, it is observed that update rate of the tracking program for the satellites motion is much more frequent as compared to the low rate of change of the Doppler frequency introduced by GPS satellite motion. So the Doppler shift can be compensated to greater extent [10].

As indicted by equation 2.5 and the relationship given in Table 2.1 the cross range (azimuth) resolution of SAR depends upon the aperture produced by the translating antenna element. As in our case the aperture is created by the movement of GPS satellite which also causes Doppler frequency shift. So these frequency shifts have considerable effect on the azimuth resolution of SAR image.

Chapter 3

GPS Signals for SAR Application

The GNSS (Global Navigation Satellite System) is a unique, interesting and revolutionary development of current times and novel applications for it are constantly being discovered. This chapter starts with some insight about GNSS. Next, with SAR application perspective GPS signals are analyzed along with its constituent elements. Concepts like power spectrum, reception and generation of GPS signal are elaborated in detail. In order to understand the simulation and generation of images and support the developed algorithms during the current research study it is imperative to investigate the important correlation property of GPS signals. This critical investigation is given at end of this chapter.

3.1 GNSS Signal Frequency Bands

Frequency bands for three major GNSS systems (GPS, Galileo and GLONASS) are highlighted in Figure 3.1. Both GNSS signals which will be available in future and being used currently are shown. It can be observed from the depicted diagram that spectrum of adjacent signals may overlap because each satellite system have numerous signals due to which bands are occupied or highly crowded. Although the positioning and navigation services of GNSS is not much affected by the signal overlap problem, due to the employed modulation scheme. However, in case of radar applications the system SNR and in-band interference will be affected to greater extent.

It is evident from Figure 3.1, the highest code rate of 10.23 MHz (in all GNSS signals) is being used by only three navigation signals namely: Galileo E5a/b, GPS L5 (recently introduced), both

L1 and L2 (P-code only). Due to the maturity of GPS system and easily available receiver components for SAR application, the option of GPS is opted in this research study.

GPS signals carrying P code are encrypted and reserved only for military purposes. Therefore, focus will be on newly introduced L5 signal along with L1. The recently introduced L5 GPS signal have some characteristics which makes it best choice for SAR applications. These characteristics include improved signal structure for better performance with parameters like: longer spreading codes, wider bandwidth (24 MHz), data-free code and high power (-154.9 dBW). All these parameters are discussed in detail in Section 3.7.

Currently GPS broadcast its signals on three carrier frequencies namely: L₁ (1575.42 MHz), L₂ (1227.60 MHz) and L₅ (1176.45 MHz) as shown in the Figure. 3.1 by the red lines. L₁ and L₂ uses UHF (Ultra High Frequency) band while L₅ works in the Aviation band.

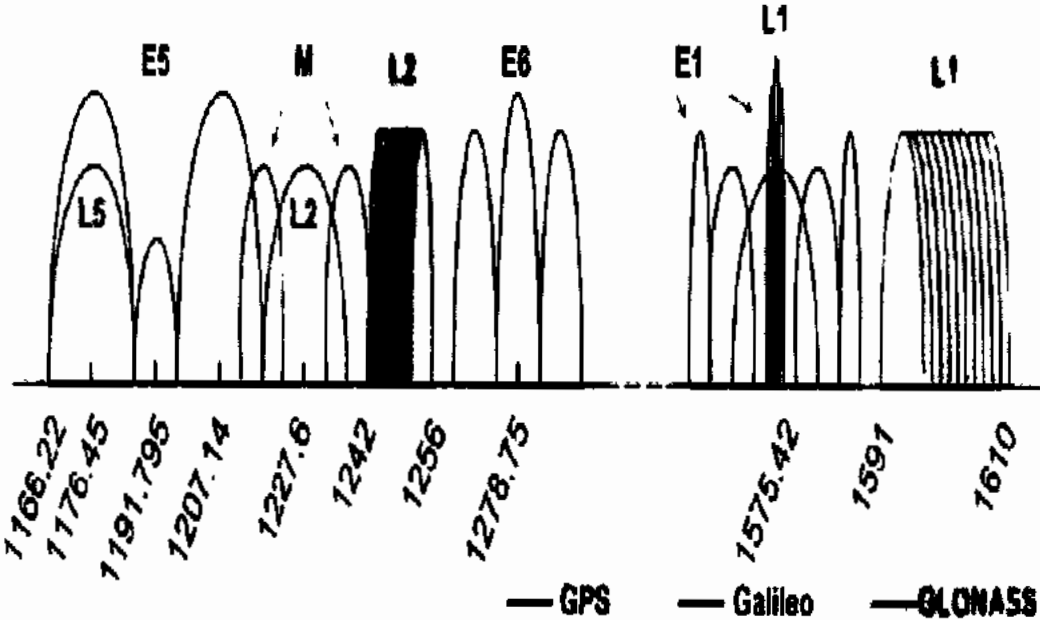


Figure 3. 1 GNSS Satellites Frequency Bands

3.2 General Description of GPS

The GPS is United States (US) space based global navigation satellite system maintained by Defense Department. Its older name is NAVSTAR. The program was initially conceived and researched in the 1960. In the start of 1978, the first satellite was placed in orbit. The full operational capability (with constellation of 24 satellites) of GPS was completed at the end of 1993.

The initial objective of GPS development was to assist the U.S. military in their missions. However, later on it was opened for public use. This technology is now a dual use system, that is, it can be utilized both by civilians and military. The civilian use of GPS is not limited to navigation and position calculation but, it can be used for remote sensing. It is not an exaggeration to claim that the GPS has revolutionized the field of navigation & positioning since last tow decades with its inception in 1995 [1] .

3.3 Elements of GPS

The three basic structural elements of GPS are: Space, Control and User segment which are outlined below.

3.3.1 Space Segment

This structural part contains a constellation of 32 satellites. Out of this total constellation 24 satellites are currently operational. The rest of 8 satellites are being placed spare for emergency use. In case, any of the satellite becomes non-functional it is replaced by one of the spare satellites. These satellites have been arranged in six nearly circular orbits (55° inclination angle). In order to ensure non stop world wide coverage service, the separation angle of 60° is

maintained among orbits to cover the complete 360° . The GPS satellites work at a height of 20,000 kilometers, with an orbital period of about 12 hours. With a clear view of the sky, one can be locked to a minimum of five satellites.

3.3.2 Control Segment

For regular maintenance purposes of the space segment, a Master Control Station (MCS) is situated in the USA (Colorado Springs). Besides this, eleven more monitoring stations are situated at different sites around the world (Ascension Islands, Kwajalein, Hawaii, Diego Garcia etc.). Some of the primary functions of these monitoring stations include: monitoring of satellite clocks, almanac data and overall system integrity. The correction made by the MCS is applied to the satellite constellation through the S-band link, as depicted in Figure 3.1.

3.3.3 User Segment

In the chain of GPS system components, the ultimate part is the User Segment. Basically, it consists of a GPS receiver having a front-end antenna for acquisition of signals, tracking circuitry, a microprocessor, and a user interface. Any one having a GPS receiver can use its services without any subscription. Satellites transmit data to the GPS user using L-band frequency. A detailed discussion about the GPS receiver is given in Chapter 5.

All the three segments are shown in Figure 3.2.

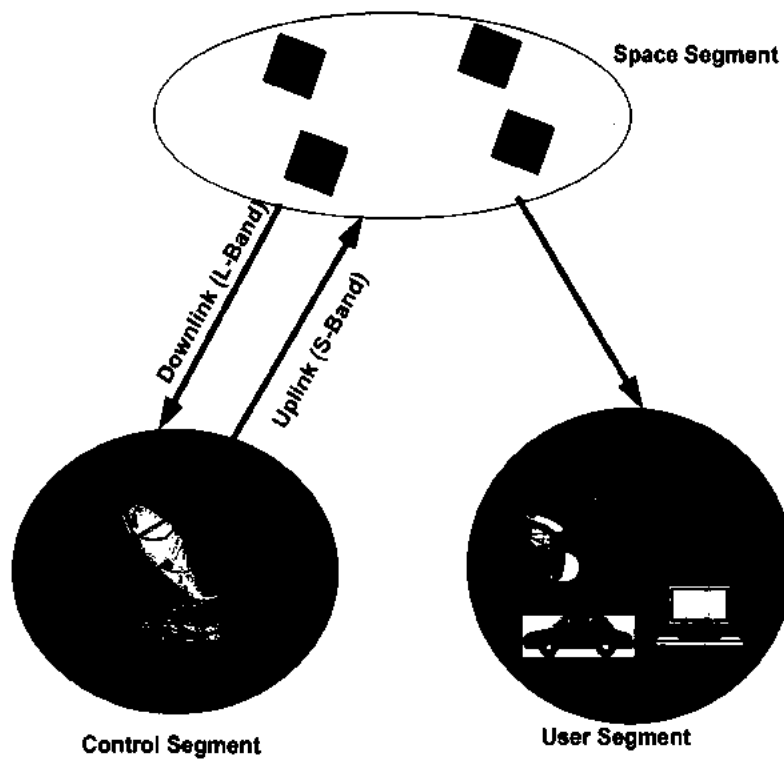


Figure 3. 2 Functional Elements of GPS

3.4 Structure of GPS Signals

The signals transmitted by GPS satellites have the three structural components: Carrier, spreading sequences and navigation data as shown in Figure. 3.3.

3.4.1 Carrier

For carrying information from GPS satellite to user mainly three carrier wave with frequencies f_{L1} , f_{L2} and f_{L5} are used.

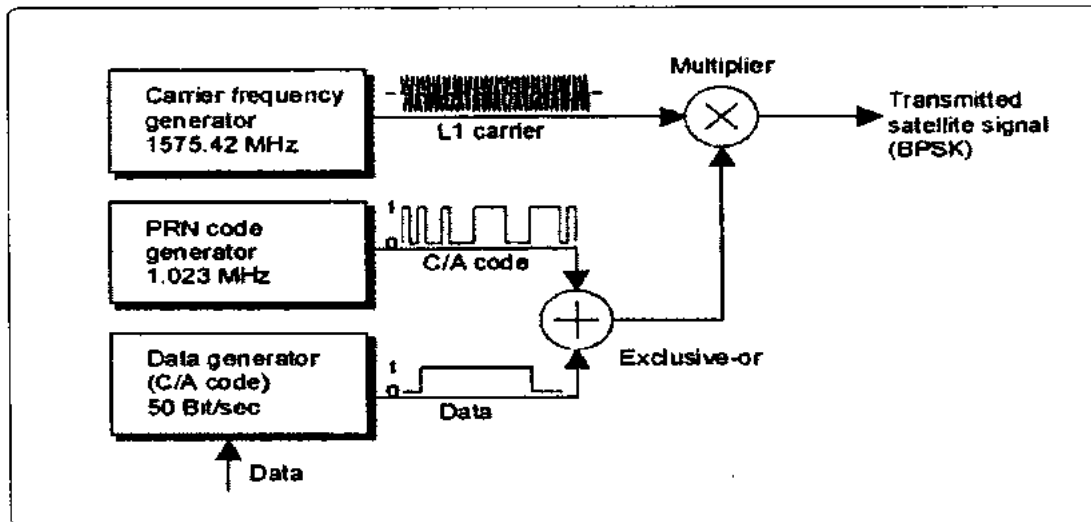


Figure 3. 3 Satellites signal Generation process

3.4.2 Spreading codes

Normally two unique spreading sequences/codes are generated for each GPS satellite. That is coarse acquisition (C/A) code and precision code (P/Y). The C/A code sometimes called PRN (Pseudo Random Noise) sequence with a bit length of 1023 chips. (One chip is equal to a bit. These chips do not hold any information's.) The PRN sequence is repeated every millisecond, that is, chipping rate of 1.023 MHz. On other hand with chipping rate of 10.23 MHz and code length of 267, the P(Y) code, which is repeated at midnight of every Saturday/Sunday of GPS week is used for security purposes and only authorized user can access it. Therefore it will not be discussed further. Only the L1 carrier is used for the modulation of C/A code while both carriers (L₁ and L₂) modulate the P(Y) code. L₁ uses two shift register namely: $G_2(1 + X^2 + X^3 + X^6 + X^8 + X^9 + X^{10})$ and $G_1(1 + X^3 + X^{10})$ and. Figure 3.4 represents the generation of C/A code for L₁ while Figure. 3.5 depict procedure for generation of L₅ signal PRN code respectively.

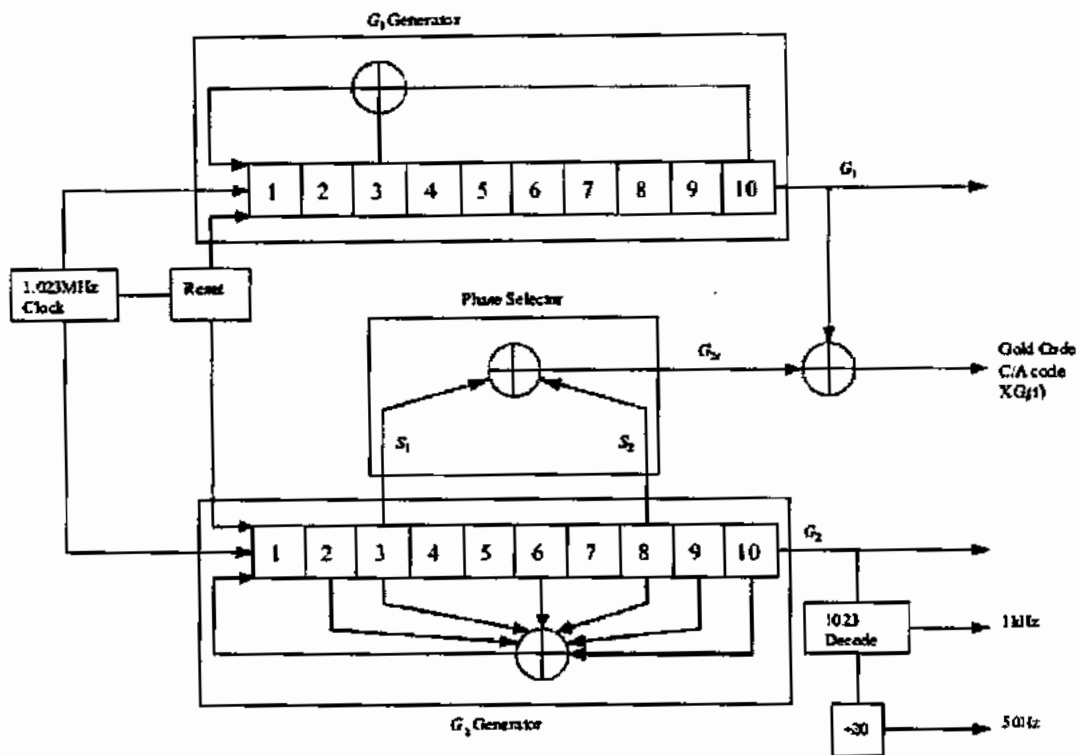


Figure 3. 4 Generation of L_1 C/A Codes

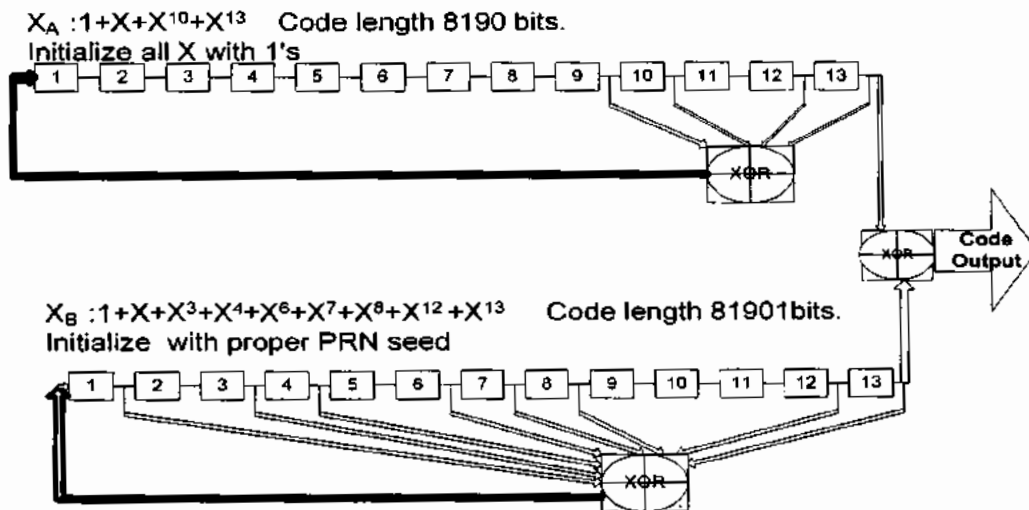


Figure 3. 5 Generation of L_5 C/A Codes

3.4.3 Navigation data

The control information's about satellite orbits are placed in navigation data, which is being uploaded with 50 bits per second (bps) by the monitoring stations of GPS. For optimization of satellite signals acquisition and accurate user's position calculation, the GPS receivers utilized the vast amount of information contained in the navigation-message [11].

Each navigation message consists of five sub-frames with individual length of 300 bits and total length of 1500 bits. Single sub-frame is made up of 10 words with 30 bits length. First three (1, 2, and 3) sub-frames are included in every frame. The remaining two sub-frames (4, 5), contains different data with the same structure which give rise to 25 versions marked as page 1 to 25.

Figure 3.6 shows the pattern of the navigation message highlighting the frames and sub-frames.

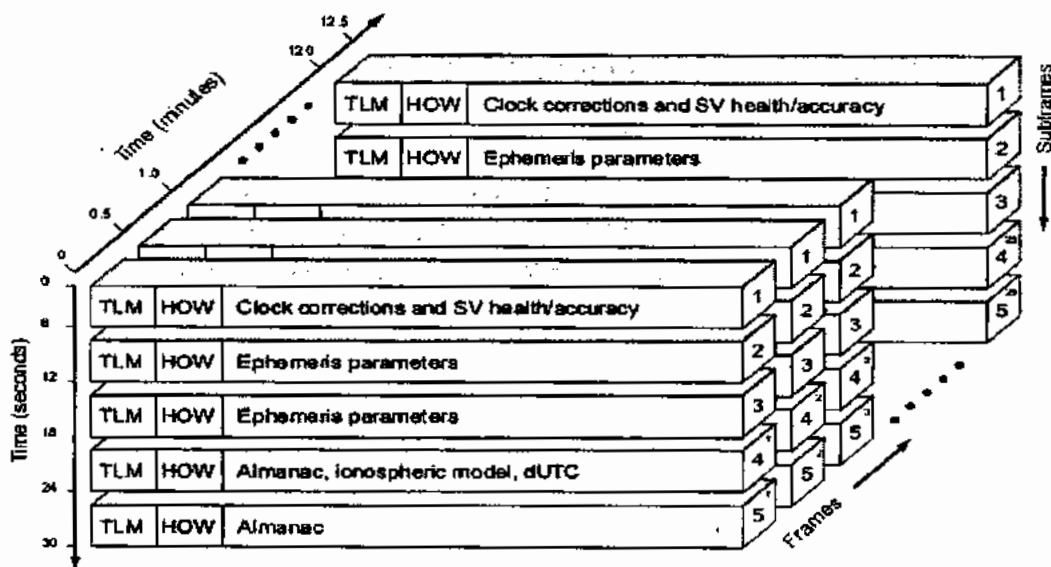


Figure 3. 6 Navigation Data Format

3.5 GPS Signals Modulation

The block diagram of Figure 3.7 explains GPS signal modulation structure [1]. The L1 carrier frequency is generated by multiplying base/nominal reference frequency ($f_0 = 10.23$ Mhz) with 154, followed by modulation with navigation data along with P(Y) and C/A codes in order to obtain the L1 signal. On contrary the L2 frequency ($120 \times f_0$) is generated by multiplying base/nominal reference frequency ($f_0 = 10.23$ Mhz) with 120 and then navigation data along with only P(Y) code takes part in the modulation as result L2 signal is generated.

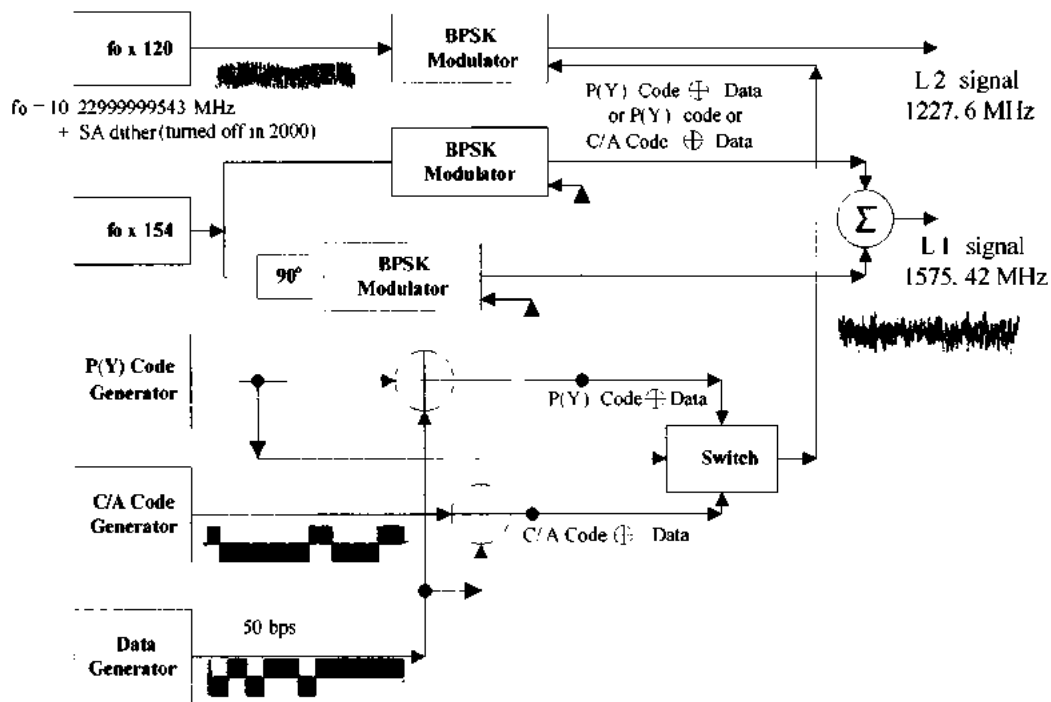


Figure 3. 7 Block Diagram describing L₁ and L₂ Signal Generation

Similarly the block diagram of Figure 3.8 represents the signal generation process of newly introduced L₅ signal. It is designed to overcome deficiencies experienced by L₁ signal. The L₅ signal consist of two channels: I₅ also termed is in phase data channel for carrying navigation

data, while Q_5 or pilot channel is responsible for enhancement of tracking function and does not carry navigation data.

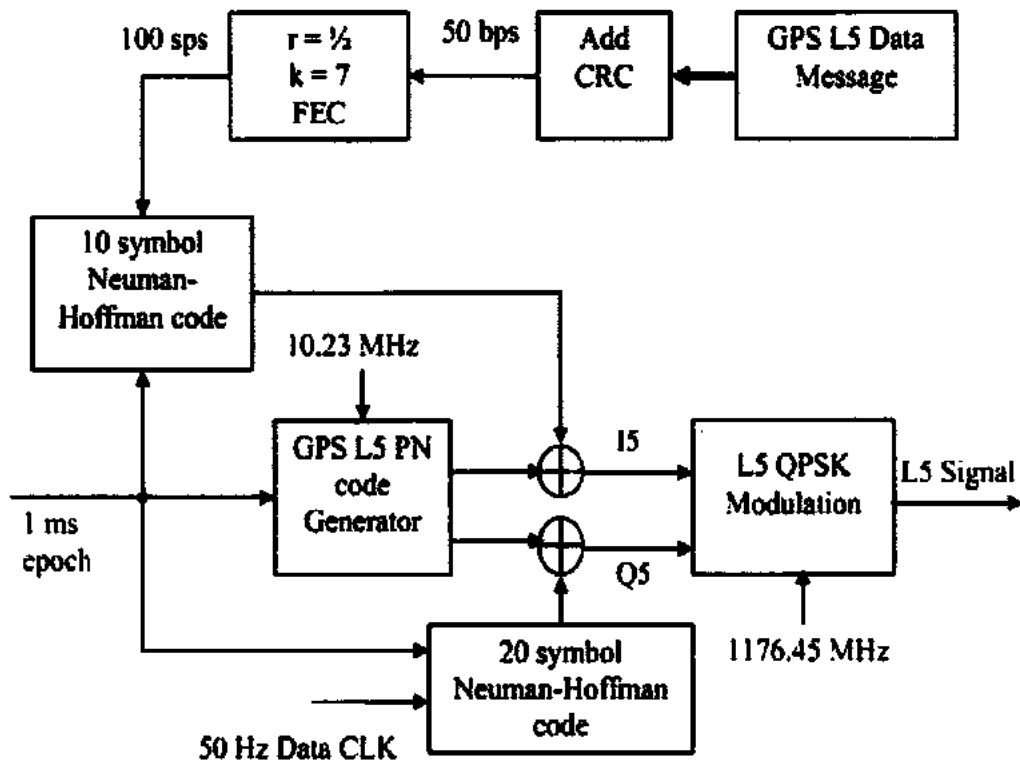


Figure 3. 8 L_5 Signal Generation

Block diagram of Figure 3.8 should be read from right to left. At the right top side, the main data with speed of 50 bps is supplied to the remaining blocks of signal generation. In next step CRC (cyclic redundancy check) bits are introduced for enhancing the error detection capabilities. This is followed by FEC (forward error correction convolution) code with a rate of $1/2$. The obtained code at hand is passed to Neuman-Hoffman (NH) modulation block with data rate of 100 sps (symbols per second). The output is forwarded to next stage modulation with pseudo noise (PN) sequence. Consequently I_5 part of the L_5 signal is generated.

Similarly, for generation of the pilot channel (Q part) containing only tracking data, in first step it is directly passed through NH code with 20 bits length. After mixing with PN code for bi phase modulation, the ultimate result in form of Q_5 channel is obtained. In final step both I_5 and Q_5 are combined for modulation using L_5 carrier frequency with QPSK (Quadrature Phase Shift Keying) technique to get the final L_5 signal.

Finally, after going through modulation process the L_1 signal carrying C/A and P(Y) codes transmitted from i^{th} satellite can be represented mathematically as:

$$S^i(t) = \sqrt{2A_{CA}}(C^i(t) \oplus D^i(t))\cos(2\pi f_{L1}t) + \sqrt{2A_{PY}}(P^i(t) \oplus D^i(t))\sin(2\pi f_{L1}t) \quad (3.1)$$

Where A_{CA} and A_{PY} represent power of the L_1 , C^i shows i^{th} satellite C/A code, P^i refers to i^{th} satellite P(Y) code, while D^i contains navigation message.

Equation (3.1) can be easily modified for L_5 signal as follows:

$$S^i(t) = \sqrt{2A_{CA}}(C^i(t) \oplus D^i(t))NH_{10} \cos(2\pi f_{L5}t + \partial_{L5}) + \sqrt{2A_{PY}}(P^i(t) \oplus D^i(t))NH_{20} \sin(2\pi f_{L5}t + \partial_{L5}) \quad (3.2)$$

Here NH_{10} and NH_{20} represent Neuman-Hoffman bits, ∂_{L5} is carrier phase of L_5 signal.

3.6 GPS Error sources

Due to the tremendous accuracy potential of this system, and the latest improvements in receiver technology, the GPS has revolutionized navigation and position location for more than a decade. However GPS signal suffers from inherent imprecision due to a variety of error sources. The combined effects of these errors during signal propagation result in the degradation of positioning accuracy as calculated by the GPS receiver. The commonly held belief is that GPS is

accurate to $\pm X$ meters, where X is often viewed as acceptable for the purpose of the system under consideration [12].

For estimating user position coordinates a term, called pseudorange is frequently used. It is basically the distance measurement between satellite and receiver, including combined effect of all error sources [13]. By measuring the time of arrival (TOA) of the signal, the user's distance (range) from each of the satellite is calculated. By combining the range from a minimum of three satellites, the user position can be calculated in three dimensions. The basic pseudorange measurement equation can be given as [14]:

$$p = r + r_d + c(d_{\Delta t} - d_{\Delta T}) + ion_d + trop_d + p_\epsilon \quad (3.3)$$

Here in Equation (3.3), p represents pseudo range expressed in meters, r refers to geometric_range, r_d an orbital_error, c shows speed_of_light, $d_{\Delta t}$ and $d_{\Delta T}$ represent clock_error of satellite and receiver respectively, ion_d ionospheric_error, $trop_d$ tropospheric_error, and p_ϵ multipath_error.

As shown in Equation (3.3), there are a number of possible sources of errors which can degrade the accuracy of position computed and hence adversely affect the performance of a GPS receiver. These error sources are discussed below one by one.

3.6.1 Orbital error

When the position of satellite as reported by the ephemeris data, mismatch with the actual position of that satellite the resultant error is known as orbital or ephemeris error. The main causes of the inaccuracies in the satellites position are gravitational forces and solar winds. This induces drift in the planned trajectories of GPS satellites. Without correction of this error, it will

ultimately leads to wrong positioning calculation of satellite as well as inaccurate user location. The ephemeris data is utilized to calculate satellite positions during image reconstruction. These errors may have some effect on location of the target, which needs to be investigated, possibly during later research efforts.

3.6.2 Satellite clock error

Although GPS satellites are equipped with high accurate and stable clocks (rubidium or cesium), but still, there is chance of errors. The behavior of satellite clocks are constantly monitored by the GPS ground control stations and correction for this kind of error is being uploaded from time to time. This helps the user receivers to remove/compensate for satellite clock error [15].

For finding satellite clock error using ephemeris data the following mathematical expression can be used:

$$E_S = af_2(t - t_e) + af_1(t - t_e) + af_0 + d_{rel} - t_{gd} \quad (3.4)$$

Where E_s is satellite clock error, af_2 , af_1 , af_0 are second, first and zero order coefficient (s) respectively. t_{gd} shows group delay, d_{rel} is used for relativity correction.

3.6.3 Ionospheric errors

The upper part of atmosphere which ranges from 50 to 1500 km is called ionosphere. It is full of both positive particles and negatively charged electron [16]. The GPS signals transmission is retarded up to 300 ns (the worst case) by these layers of free electrons, which results in 100 meters range errors [17].

Both carrier and code phase calculations are adversely affected by the ionospheric error, which sometime leads to lose the locked satellite. The normal range of this error is 5-30 meters. The

receiver geographic location, solar cycle, Earth's magnetic field, local time of the day and season are some of the contributing factors which can increase this error.

The ionospheric error is dispersive in nature, meaning that the delay is dependent upon the frequency of the signal. In order to provide the ionospheric error free result dual frequency GPS receivers employ correction to such effect [18].

3.6.4 Troposphere error

Troposphere is the initial part of atmosphere and ranges up to 16 km in altitude from the surface of the earth, although the neutral atmosphere extends up to 60 km [19]. The Troposphere affects the GPS signals which are in fact electromagnetic waves, to a significant level. As a result the GPS signals are both delayed and refracted. The main factors which cause troposphere delay include temperature, pressure and humidity. The delay also varies with the height of the user position as the type of terrain below the signal path can affect the delay. According to Hopfield [20], there are two components of troposphere delay, namely wet delay and dry delay. The dry component which comprises of about 80 to 90% of the total delay is easier to determine as compared to the wet component. Table 3.1 depicts the average numerical values of both components of the troposphere delay related to different elevation angles.

7/1/2015

Table 3. 1 Tropospheric Delay on Measured Range

S.No	Elevation angle (in degree)	Dry component (in meters)	Wet Component (in meters)	Total Delay (in meters)
1.	90 ⁰	2.3	0.2	2.5
2.	20 ⁰	6.7	0.6	7.3
3.	15 ⁰	8.8	0.8	9.6
4.	10 ⁰	12.9	1.1	14.0
5.	5 ⁰	23.6	2.2	25.8

The dry delay is mainly caused by the O₂ and N₂ gases present in the atmosphere and it can be modeled only up to 1% or better. On the other hand the wet delay which causes up to 10-20% of the total delay is difficult to model. The wet delay is due to the presence of water vapors in the atmosphere. Mathematically the tropospheric delay T can be represented as

$$T = \int_{path} (n-1)ds + \Delta_g \quad (3.5)$$

Where n is the refractive index of the atmospheric gases and g is the difference between the curved and free-space paths.

During the last several decades, number of models (Hopfield model, Saastamoinen model, etc) have been developed and reported in scientific literature by researchers for estimation and correction of the delay induced by the troposphere in the GPS signal. However, much research has gone into the creation and testing of tropospheric refraction models to compute the refractivity N along the path of signal travel. Among these models the Hopfield model is most commonly used.

3.6.5 Receiver clock error

Receiver clock error occurs when there is time mismatch b/w GPS system and receiver clock. This kind of error mainly depends upon type of oscillator used in the receiver. Carrier phase and pseudorange calculation are normally affected by the drift in receiver clock. The receiver clock error can be compensated to greater extent by employing differential GPS principals.

3.6.6 Multipath error

Entrance of different versions of the same signal at the front end of the receiver, is the basic reason behind the multipath error. This affects mask correlation peak of the original signal. It

will not be discussed in detail as we are exploiting this property of the GPS signals to locate the target in the region of interest.

Besides these major error sources, receiver noise, calculation and rounding off error and relativistic effect are also the contributing factors (error up to 1-2 m) which degrade receiver accuracy. Table 3.2 gives summary of the GPS error sources discussed along with approximate values.

Table 3. 2 Summary of GPS errors

Type of error	Description	Approximate Error value in meter
Ephemeris_Error	Biasness in satellite location	± 2.5 m
Satellite/Receiver clock_Error	Time difference b/w the satellite/ receiver clocks	± 1.5 m
Ionosphere_Error	Error in the pseudo-range induced by ionosphere effect	± 25 m
Troposphere_Error	Error in the pseudo-range induced by Troposphere effect	± 25 meters
Multipath_Error	Error due to the multiple copies of the same signal	± 1 m
Receiver_Error	Biasness in measurement of range due to interchannel and inaccuracy of softwares at receiver end	± 10 m

3.7 Analysis of GPS Signals

In order to analyze the suitability of L1 and L5 signal for BSAR application the performance evaluation parameters considered during the research study by the thesis author are: autocorrelation, power budget analysis, and power Level. Detail analysis is documented in [21].

3.7.1 Autocorrelation

In satellite navigation applications, autocorrelation function has great importance. It basically refers to the integration & multiplication of a signal with its delayed copy. The general formula for the auto correlation function as given in [9] can be written as: -

$$R(\tau) = \lim_{T \rightarrow \infty} \frac{1}{2T} \int_{-T}^T f_i(t) f_i(t - \tau) dt \quad (3.6)$$

Where $f_i(t)$ represents signal with time t for i^{th} satellite, T is time period and τ is delay in time.

The autocorrelation properties are utilized to detect a GPS signal in a noisy environment. The C/A codes of GPS signals exhibit greater auto correlation peak and low cross correlation [22]– [24]. For better detection of a weak signal, it is necessary that auto- correlation peak of the weak signal should be greater as compared to cross-correlation peak of the strong signal. As C/A codes are near to orthogonal therefore cross-correlation value will approach to a smaller value. The auto-correlation function of a maximum length C/A code consists of an infinite sequence of triangular function, as shown in Figure. 3.9 (a,b) for both L1 and L5 respectively [25]. The peaks in the figures, shows high correlation value, which can be defined mathematically for L1 and L5 as follow: -

$$R_1(\tau) = \frac{1}{1023T_{CA}} \int_{t=0}^{t=1023} f_z(t) f_z(t - \tau) dt \quad (3.7)$$

$$R_5(\tau) = \frac{1}{10230T_{CA}} \int_{t=0}^{t=10230} f_z(t) f_z(t - \tau) dt \quad (3.8)$$

Where $f_z(t)$ is C/A code with time t for z^{th} satellite, T_{CA} is single C/A chipping period ($L1=977.5 \text{ nSec}$ and $L5=97.75 \text{ nSec}$) and τ is delay in time.

Simulation is carried out in Matlab environment, for the autocorrelation of one set of C/A code for a satellite broadcasting L1 signal and the result is plotted in Figure. 3.10. The amplitude peak value around 1500 in the diagram represents autocorrelation of C/A code. Similarly Figure. 3.11 depict the autocorrelation of the simulated L5 signal with autocorrelation value more than 4000. It is evident from the diagram that L5 autocorrelation value is greater than L1. Hence L5 provides better detection capability as compared to L1 signal. The secondary peaks in Figure. 3.10 of the auto correlation are significantly less than higher peak. Both Figure 3.10 and Figure 3.11 clearly show that the cross correlation values are low; which enables the satellites to transmit signals simultaneously with same frequency using different C/A codes. From both figures it is evident that the secondary peaks in the auto-correlation diagrams are significantly lower than the higher peak. This higher peak value helps the receiver in acquisition/tracking of GPS signal.

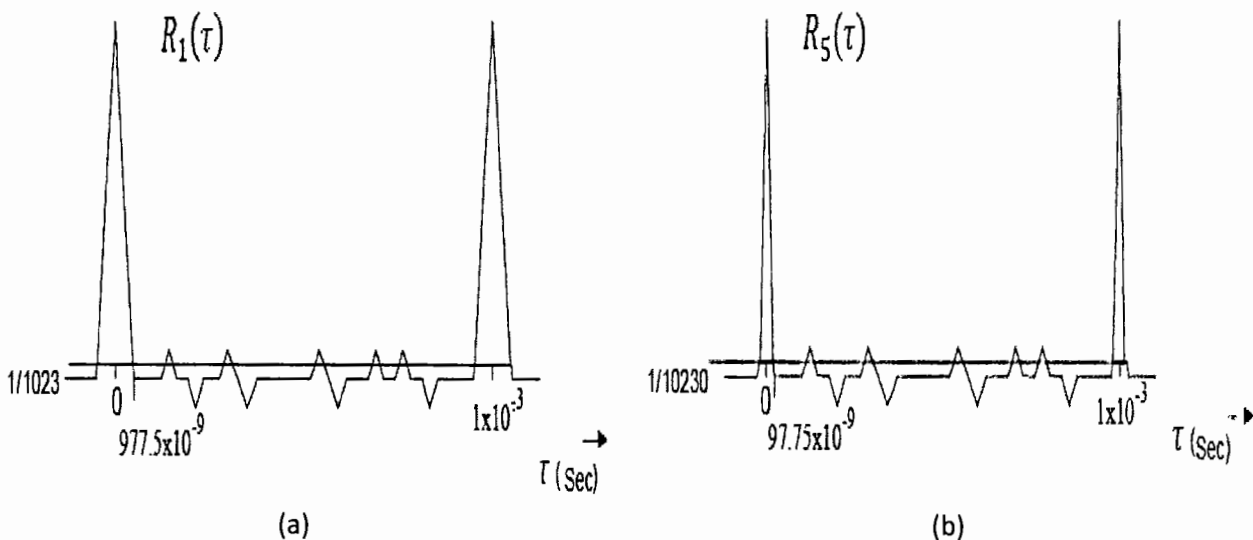


Figure 3. 9 (a) L1 Autocorrelation Function (b) L5 Autocorrelation Function

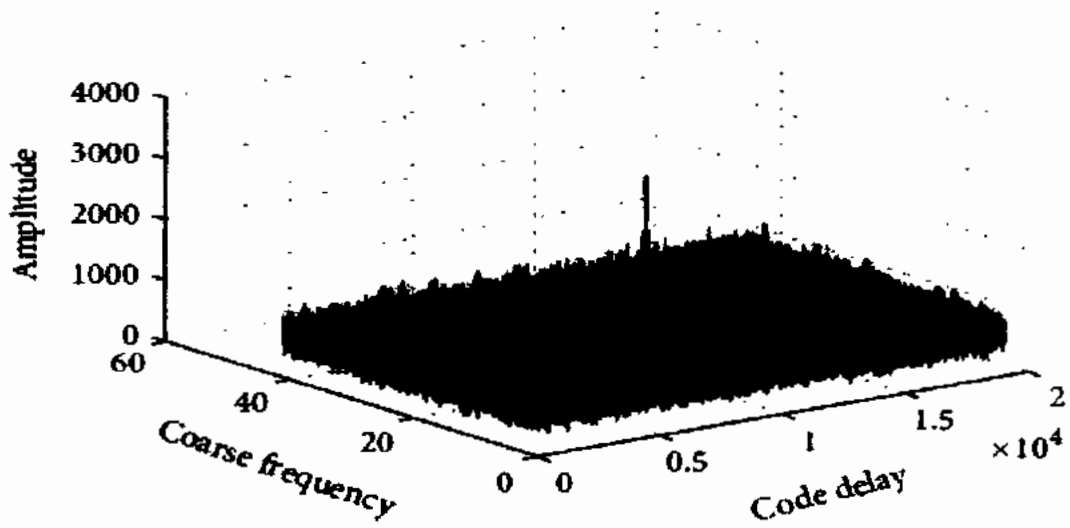


Figure 3. 10 The Autocorrelation of L1 signal

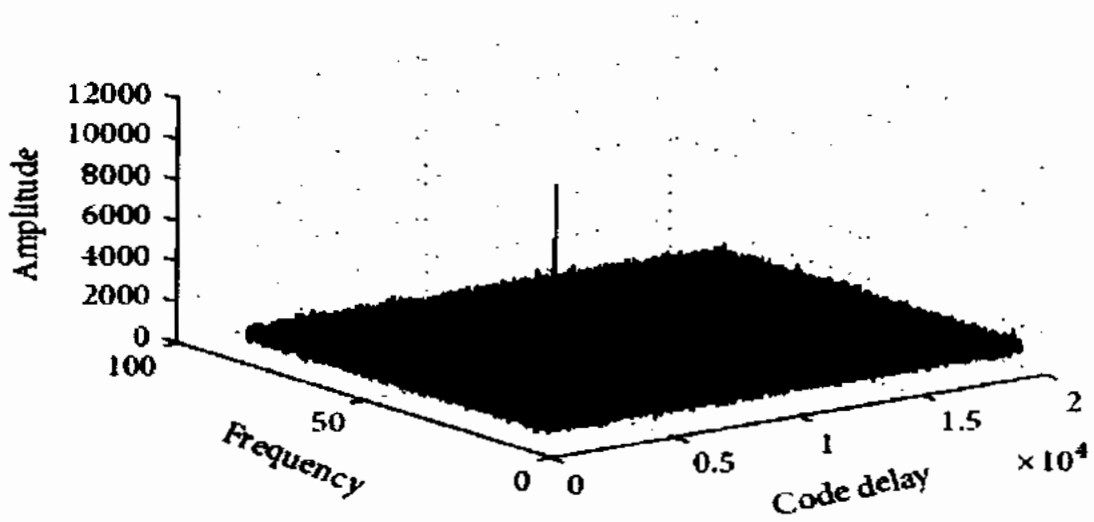


Figure 3. 11 The Autocorrelation of L5 signal

3.7.2 Power Budget Analysis

To check suitability of reflected L1 & L5 GPS signal with the aim of its utilization in remote sensing, power budget analysis is needed. Power budget analysis of reflected GPS signals has been elaborated in [25]–[27] where the reflected signals are used for passive imaging and target detection. The analysis is first accomplished for L1 and then for L5 signal.

Let P_t represents the power of transmitter (GPS satellite), G_t gain of transmitter, σ cross-section of target, R_1 shows distance (range) from satellites to target, R_2 is distance from receiver to target, then the received power can be calculated as [8]:

$$P_r = \frac{P_t G_t}{4\pi R_1^2 4\pi R_2^2} * \sigma A_{ef} \quad (3.9)$$

Where A_{ef} represents receiving antenna effective area calculated by following mathematical formula when GPS signal wavelength and receiver gain is known:

$$A_{ef} = \frac{\lambda^2 * G_r}{4\pi} \quad (3.10)$$

The receiver antenna SNR (Signal to Noise ratio) can be computed as:

$$SNR = \frac{P_t G_t G_r \lambda^2 \sigma}{(4\pi)^3 R_1^2 R_2^2 KTB_n} \quad (3.11)$$

Where KTB_n represent noise of receiver while λ is wavelength of GPS signal.

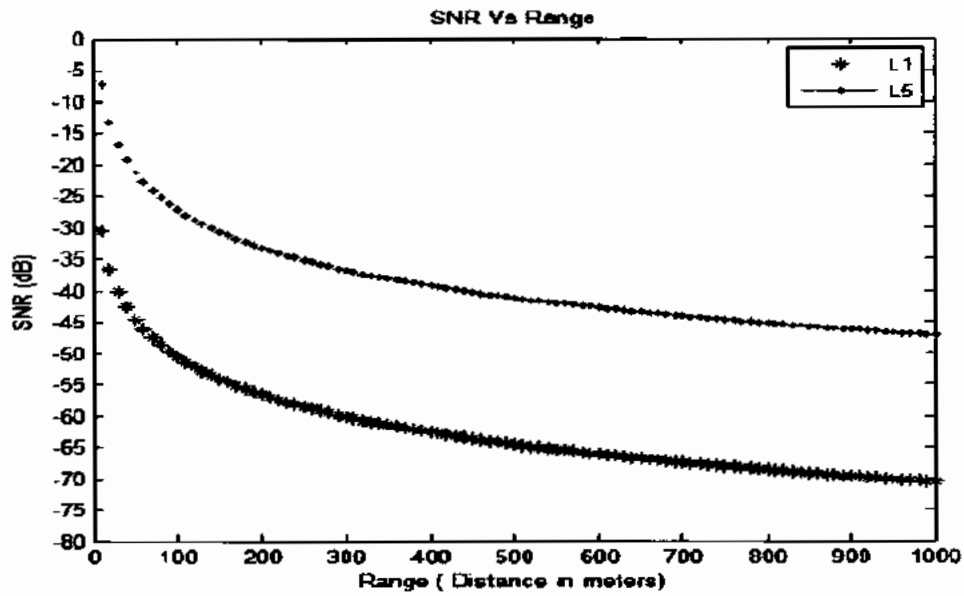


Figure 3.12 Range versus SNR without processing-gain

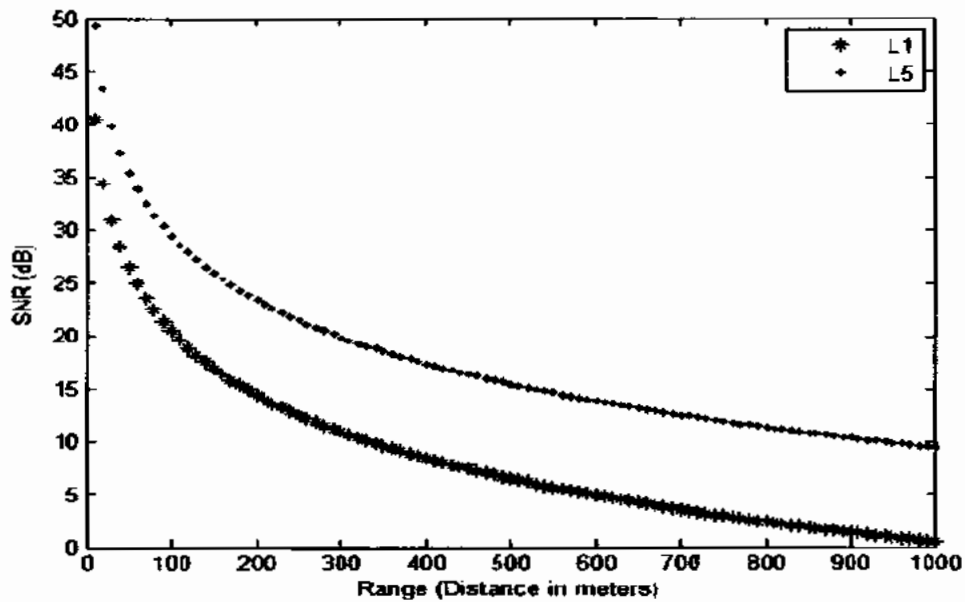


Figure 3.13 Range versus SNR using processing-gain

Due to wide bandwidth, addition of Neuman-Hoffman codes in modulation and comparatively longer spreading codes, the L5 signal as expected, given a high processing gain which is evident from Figure. 3.13. SNR comparison plots for L1 and L5 are shown in Figure 3.12 & Figure 3.13.

Simulation result of Range (0 to 1000 m) versus SNR, without using processing gain and target cross section of 10 m^2 was recorded for both L1 & L5 reflected GPS signals and plotted in Figure 3.12. SNR is calculated for different values of the range. At a range of 100 m SNR values of L1 and L5 signals are respectively -50 dB and -30 dB, which are very low and detection of target is almost impossible in both cases. It is evident from Figure 3.12 that the SNR is very poor even at short distances; hence tracking of the GPS signals is almost impossible.

For further SNR improvement the GPS signals were correlated for a longer period of time consequently better processing gain was achieved. The simulation results of SNR with processing gain of 43dB for GPS L1 and around 50 dB for L5 are shown in Figure. 3.13. It is worth mentioning that the L5 reflected GPS has 7 dB more processing gain when compared with L1 signal.

On the basis of higher correlation levels depicted in Figures 3.10 & 3.11 it can infer that L5 signal as compared to L1 is more reliable and presents greater resistance to wrong acquisition problem. Moreover from the results it can be observed that, for same acquisition time noise floor of L5 signal is lower than L1 and therefore acquisition peaks are more prominent. This low noise floor of L5 signal has advantages of: better accuracy, low distortion and high processing gain.

3.7.3 Power Level

The L1 signal has minimum signal strength of -158.5 dBW while L5 has -154.9 dBW [1]. It means that L5 is 3.6 dB better level as compared to L1. Beside this, bandwidth of L5 signal is 10 times larger than L1. This increase in bandwidth ensures accuracy in noisy and multipath environment. Figure 3.5 shows the power spectral densities of L1 and L5 signals.

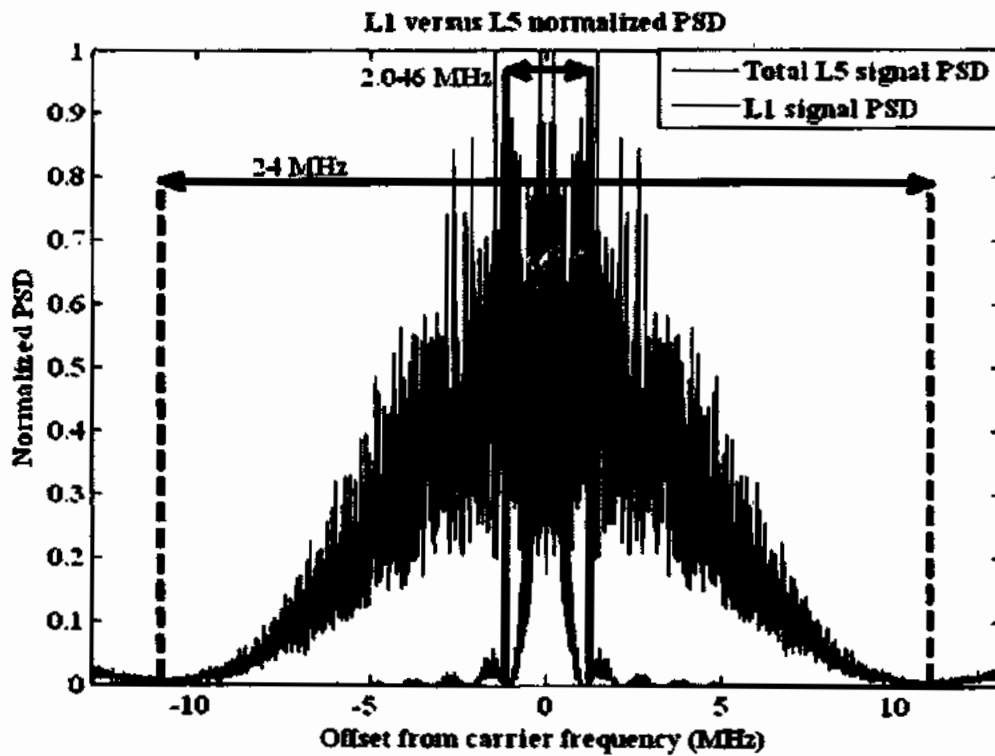


Figure 3. 14 Power spectral densities of L1 and L5

Some other important difference parameters between L1 and L5 are summarized in Table 3.2.

Table 3.3 L1 and L5 Comparison Parameters

Parameter	L1	L5	Remarks
Bandwidth	2 MHz	24 MHz	The higher bandwidth of L5 can provides better accuracy in noisy environment
Center Frequency	1575.42 MHz	1176.45 MHz	
Secondary Codes	N/A	Neuman-Hoffman (NH) codes	The addition of NH codes in L5 signal 1. Improved spectral line component spacing 2. Reduced affect of narrow band interference 3. Result in Low cross correlation 4. Provides better synchronization at bit level
Chip Rate	1.023 MHz	10.23 MHz	Increases chipping rate of L5 1. Provides greater bandwidth performance 2. Low signal distortion 3. Provides greater accuracy
Data Encoding	No	Improved data encoding with Parity & Cyclic Redundancy Check	Greater signal and data integrity can be achieved with advanced methods of encoding

Chapter 4

Literature Review

It is always prudent to keep abreast with the recent developments in relevant research area. In order to broaden the academic perspective and obtain knowledge of the contemporary research activities in GNSS based remote sensing and imaging, some aspects that are pertinent to the research topic have been reviewed, discussed and analyzed in this chapter.

4.1 Different types of GNSS Remote Sensing

Although GNSS reflected signals have numerous remote sensing capabilities, but still expert of the GNSS community consider them as a nuisance factor. The credit goes to the European Space Agency who envisaged the idea in 1993 for the first time that reflected GPS signals have remote-sensing capabilities [28]. Subsequently, the idea has been further elaborated in different scientific documents by numerous researchers. The most relevant research has been carefully selected and reviewed.

4.1.1 Ocean Remote Sensing

Ocean remote sensing based on GNSS reflected signals includes: measurement of ocean surface roughness and height, direction/ speed of sea wind, target detection near sea surface etc. For the mentioned applications minimum one example has been discussed in following paragraphs.

A research performed by C. Zuffada et al. studied remote sensing of sea surface wind and topography based on reflected GPS signal. They investigated the change in signal statistical

characteristics along with coherence time [29]. The authors state that after striking off the sea surface the GPS signal spreads in omni-direction and carries maximum power in the forward scatter direction. They also highlighted that by observing at given instant of time, the combine effect of the reflected signals on the power at receiver input depends on the geometry, system parameters and current state of sea surface. The researcher concluded that from the analyzed waveform, parameters of the ocean like wind speed/direction and surface height can be deduced by utilizing the waveform upper and lower edge respectively [29].

The research initiated by S. Katzberg and his other fellows in 1996 at NASA research centre regarding the use of reflected GPS signals for remote sensing applications result in a series of publications. Using the concept of forward scattered GPS signals they successfully measured sea wind speed [30].

In similar research a specialized receiver with two antennas one in zenith direction for direct signal tracking and another nadir-oriented antenna for reflected signal was utilized by J. L. Garrison. For estimation of wind speed using correlation values, the author employed inversion of bistatic scattering models technique. During this research analytical models were utilized to compare the shape of signal power distribution. Basically two methods were selected for the purpose of matching the power distribution patterns. The first highlighted that the leading edge of GPS reflected signal carries important information's. Nonlinear least squares estimates were obtained in the second approach for matching the complete shape of the signal [31].

Based on reflected GNSS signals Wang Xin et al. studied the sea wave height, speed and direction by performing an experiment in the coastal area of southeast China [32], [33]. In their research experiment they used modified Soulat method and derived adaptive semi empirical

expression in order to study the sea wave height in near and far field of the static sea. The research findings were then compared with off the shelf ultrasonic gauge device for accuracy purpose. The authors concluded that the sea wave height and coherence time depends upon on the topographic conditions of the area being investigated. For wave speed and direction a method is also presented which is based on reflected GPS data and three observational sites.

Sarab Tay et al. proposed the idea based on Extended Kalman filtering for near ocean surface target tracking [34]. In order to detect and track the mobile target lying near sea surface, the researchers used coastal receiver along with reflected GPS signals. The problem of receiving weak reflected signals in non-stationary medium has been tackled through matched filtering.

Apart from positioning the data collection device on light aircrafts, some experiments have been performed in which such hardware was installed on low earth observing satellites termed as LEO.

In October 2003, United Kingdom (UK) launched a satellite as part of Disaster Monitoring Constellation (DMC) mission, which made it easy to monitor the reflected GNSS signals from LEO. The basic aim of this low cost satellite was global disaster monitoring along with providing daily images to be used in numerous applications. Quite promising results regarding remote sensing of the sea surface roughness, land and ice detection have been achieved through this satellite [35].

A similar effort made by university students as a scientific mission named, SuRGE (Student Reflected GPS Experiment), was carried out to measure reflected GPS signals [36]. It was explored during the experiment that ocean surface height can be measured through computation of signal delay. Similarly it was argued by the researchers of the mission that signal power

distribution provides information about the sea roughness, resulting basically from wind driven waveforms. The experiment also highlighted that reflected GPS signals from earth surface have the potential to be used for measurement of soil moisture. The instrumentation used to capture both direct and reflected GPS signal i-e for data recording purpose at selected ground stations consisted of GPS receiver with signal translator (S-Band). The GPS reflection data was down-converted and re-broadcasted for post-processing and retrieval of earth and sea surface characteristics.

After the success of (SuRGE) it was proposed to carry out practical experiment based on bistatically scattered GPS signals received in the LEO satellite orbit to demonstrate the collection of altimetry data including sea surface wind speed, direction etc. The SuRGE mission provided a new avenue in remote sensing research based on GPS reflected signals and opened attractive ways for collaboration among aerospace industries, universities and NASA centres.

4.1.2 Hydrology and Vegetation Remote Sensing

GNSS based reflectometry is one of the emerging and promising tool for measuring hydrology. One of the key land parameter in hydrology is soil moisture content. ESA and NASA are launching missions for retrieval of global soil moisture measurement. So far they have launched two successful missions namely: SMAP (Soil Moisture Active and Passive mission) and SMOS (Soil moisture and ocean salinity) [37], [38].

Y. Jia et al. investigated soil moisture remote sensing based on GNSS reflectometry concept [39]. In their study the researchers performed an experiment for soil moisture data collection. A small UAV based GNSS receiver was utilized during the several flights for capturing both direct and reflected signals. Open loop approach was selected by the researchers for post processing of

the collected signals. The authors claimed that without taking into account surface roughness and incoherent component the soil moisture content can be retrieved from the power ratio of RHCP direct SNR over LHCP reflected SNR. For the estimation accuracy improvement an over water calibration method is suggested.

Another similar study was conducted by Y. Jia and Patrizia Savi by applying polarimetric GNSS-R technique. This time along with soil moisture content research findings for vegetation biomass were also analyzed and documented [40]. For investigation of the soil moisture and vegetation fluctuation three polarimetric observables were considered. The authors conclude that reflectivity value for the grass and forest was higher as compared to lakes.

R. Alvarez et al. practically demonstrated vegetation remote sensing through field experiments [41], [42]. In their research experiments they have utilized Interference Pattern Technique (IPT) for the measurement of vegetation height and other land geophysical parameters. According to the authors of the paper the vegetation biomass height retrieval results were quite promising.

For monitoring of forest biomass based on reflected GNSS signal P. Ferrazzoli et al. performed useful simulation based study. The already developed electromagnetic model by the same author was used and different vegetation land sites were tested accordingly. It was pointed out that the magnitude of reflected signal power decreases as the biomass increases. However the simulated results supported the idea of GNSS-R for biomass monitoring. It is concluded that reflected signals with low observation angles carry reasonable SNR, hence are best suited for forest biomass application [43].

4.1.3 Cryospheric Remote Sensing

Investigation of polar sea ice states based on surface reflected GPS signals analysis is another interesting direction of remote sensing [23]. Due to the harsh environmental conditions of these areas the application is more attractive and useful. Appalling visibility due to persistent cloudy weather and hostile environment are some of the factors, which posed unique difficulties for conventional instrumentation in aerial or situ mapping of polar ice states. On the contrary GNSS signals can be accessed and recorded any where in all weather conditions for the purpose of off-line signal processing. Hardware setup utilized by the researchers included a dual channels modified GPS receiver, two compact antennas, relevant cables and data storage device. The modified GPS receiver measured correlation power at offset values of Doppler and delay with a LHCP antenna in nadir-direction. The basic computation was the power received from a reflected signal for different Doppler and delays values.

In December 2009 at Dome Concordia, Antarctica, a GNSS-R based experiment for snow monitoring was conducted. Continuous data was collected for 12 days by employing two antennas: RHCP and dual polarized (LHCP+RHCP). These antennas were then joined to a special purpose GNSS-R receiver, which was mounted on tower having height around 45 meters. The research findings of the experiment states that GNSS signals (L band), when bounce back from snow surface have long coherence time. It is also point out that these reflected signals can determine ice layer upto 200-300 meters in depth. Detail of the experimental set up is documented in [44]–[46].

4.1.4 Atmospheric Remote Sensing

As mentioned in section (3.6.3) of the thesis that the major part of atmosphere is made of ionosphere and troposphere. Both have a significant effect on the propagation of GPS signals. For remote sensing of different atmosphere parameters which includes: ionosphere electron density, humidity, pressure, temperature etc both space borne and ground based GNSS-R monitoring is commonly practiced. Promising results have been achieved through this approach in the field of: weather forecasting, space weather and atmospheric science, climatology and numerical weather model [47]–[49].

For investigating atmospheric conditions another emerging and interesting technique of Radio Occultation (RO) can be utilized in GNSS-R. This technique is more successful so far and achieved remarkable results in terms of vertical resolution and atmospheric measurements globally [50]. Several special purpose satellite constellations working on RO principle have been launched including the recently added US and Taiwan combined FORMOSAT-7/COSMIC-II mission. This observing system have the capability of investigating more than 8000 radio occultation profiles everyday. Using the nine years GPS based radio occultation data from (2001-2009) Schmidt and his fellow researcher point out for the first time, that initial part of troposphere has low temperature as compared to the warm upper part [49].

In the last few years although, satisfactory progress is made in terms of sensing atmosphere, based on GPS radio occultation principle. However there is still need of making ground based GNSS observations which can provide high temporal spatial resolution in short period of time [51]–[53]. For example, due to the unavailability of GPS satellites, for line of sight observation for longer period of time, it is difficult to measure ionosphere and troposphere profile

information directly from GPS tomographic data. The dream of improved and high temporal spatial resolution, with more detail profile contents of the atmosphere will soon change into reality as sophisticated GNSS radio occultation missions and more GNSS satellites are getting ready for launch in near future [54].

4.2 Initial Research regarding GPS Imaging

Y. Li and Co-authors performed foundation research study and envisaged the idea of GPS imaging based on reflected signals [55]. For movement detection of the imaged object the researcher conceived the technique of Bi-static radar. In order to improve spatial resolution of detection the idea of matched filter was utilized. Keeping in view the visible satellite, receiver and the imaged target, several scenarios were considered and simulated.

Generalizing the concept of bi-static radar, the authors in [55] presented a multi static SAR system. The constituent elements of the system included: GPS satellite transmitter's constellation, multiple frequency GPS receiver and several targets/objects in the area of interest. A 3D multi-static SAR system for terrain imaging purpose was arranged by placing the transmitter and receiver at different locations and moved by varying speed.

According to the authors observation the received reflected signal $S_{Rij}(t)$ exhibits characteristics like linear FM signal. For obtaining reasonable resolution, $S_{Rij}(t)$ should be compressed. Using the auto correlation function narrow pulse property of the linearly frequency modulated signal; the researcher argued that after passing through a matched filter, the final signal output will becomes more narrow. For improvement of the system resolution match filtering method was employed in the signal processing at the receiver end.

From the simulation results and observations presented in [55] it can be concluded that receiver and target velocities have profound effect on the system resolution. This has been proved during simulations performed by the thesis author, in search of optimum geometry for the imaging system and will be further explained in the coming chapters. Increased speed results in more change in geometry, thus improved resolution. It was further proved that spatial resolution also depends on the position of transmitter with respect to receiver and object. However, it seems that the researchers have not carried out or documented further work in order to validate the simulations with the construction of imaging hardware or improved reconstruction algorithms.

The secondary application of GPS signals has been further documented by Bijan Mojarrabi et al. In this research communication, power budget analysis of reflected GPS signals is elaborated for the purpose of passive target detection and imaging. They studied different configurations of the receiver, in stationary format, moving on the ground or space borne. Their research focused on the GPS signal low power levels, which normally comes out around -160 dBW, when the signal strike off at the Earth's surface. They indicated that some power will be absorbed, due to the surface nature of the target or reflector; resulting in a further reduction of signal strength. An interesting account in the research was related to the maximum detection range. However, the range and other calculations given the paper were theoretical results and need to analyze carefully prior to any inference regarding practical aspects. Again, no follow up research activity in this area by same authors is available [26].

E.P.Glennon et al. examined the air target detection capability of GPS as bi-static radar [56]. The research work was initiated with power budget analysis for single satellite, later on extended with multiple satellites. Greater clutter power, low SNR of the reflected GPS signal and near-far constraint were the main problems of the system highlighted by the authors. In order to

overcome the difficulties, a few suggestions were proposed for real time deployment of GPS based bi-static radar. The outlined suggestion includes: multipath mitigation techniques for near-far problem, high gain antenna, non coherence integration for longer period of time and clear visibility of the locked satellites. The researcher concluded that such workable system can be developed by utilizing new GNSS signals along with the proposed suggestions.

The concept of air target detection was further extended by V. Behar and C. Kabakchiev by utilizing GPS L5 signal. The principal of FSR (Forward Scattering Radar) was incorporated while giving numerical and theoretical estimation for the air target detection using navigation receiver based on L5 signal. In another paper by the same authors after performing power budget analysis for the same setup, it is claimed on the basis of obtained results that FSR configuration along with reflected L5 GPS signal is suitable for slowly moving air targets [25], [57].

It would be an injustice not to mention the work performed by Microwave Integrated Systems Laboratory (MISL) research group at the University of Birmingham and especially Dr M Cherniakov. The group has registered some impressive research regarding GNSS signals as transmitters of opportunity and general bi-static radars (BR). Initially using the idea of BR the researchers [27] checked the feasibility of air target detection and specified the relevant encountered hurdles. Iridium LEO satellite signals were utilized by the researcher for air targets detection and highlighted issues like direct satellite signal interference, background noise and clutter. The authors presented equations for the power density of reflected signals, total power at the receiving antenna and maximum detected range. A calculated example specifies that maximum possible range is 30 km which is unfeasible practically. In their experimental set-up two types of antennas were used and a helicopter was used as the target. Interestingly, the authors concluded that the alarming issue/problem for the proposed system design is the

interference from direct signal. They mention numerous methods, for example, space and frequency adaptive filtering, polarization and wave separation for mitigation of interference.

In order to detect reflected signal in the presence of direct signal background the thesis author relied on the opposite polarization of direct and reflected GPS antennas and the main lobe of the LHCP antenna was positioned away from the reference GPS satellite. A cone shaped base plate has been used in the LHCP antenna that suppresses the side lobes, thus further preventing the reception of direct signal that may cause undue interference during signal detection and later image formation.

In the last part of chapter 3 of this thesis a power budget analysis of reflected GPS signals was summarized. Power budget analysis for GNSS signals in SAR context has been performed in a separate research by the same research group at MISL [58]. The scenario similar to the one as depicted in chapter two of this thesis is termed as SS-BSAR (Space Surface Bi-static Synthetic Aperture Radar). According to the researchers the most important factor is the reduction of noise rather than interference in the power budget of SS-BSAR. Finally, several methods are suggested for the improvement of Signal to Interference Ratio (SIR). In essence, this research confirms and reiterates the same problems and points of concerns that have been mentioned in the results and analysis chapter of this thesis.

Two configurations suitable for practical applications have been proposed in [59]. For the airborne receiver configuration the low power budget specifies SS-BSAR application for short and medium range radar placed on autonomous small aircrafts. This kind of application is recommended for the purpose of disaster management, rescue and search operation. Due to the longer integration time in case of stationary receiver, more favorable power budget is obtained.

Which makes it best choice to be utilized particularly in change detection and interferometric observations [59]. During current research efforts the thesis author has utilized a stationary receiver to collect GPS data, the orbiting satellites provided the requisite change in geometry, hence the system can be used for above-mentioned applications.

Documenting further research [60], M Cherniakov and co-authors presented an experimental configuration for the study of SS-BSAR with GNSS as Non-Cooperative Transmitters (NCT). The set up comprised of three channels radar receiver, namely, navigation, radar and heterodyne channel. Radar antennas and a custom-made track carriage system functioning as flight imitator were also part of the arrangement. The area used for the experiment was part of land surrounded by trees and two corner reflectors with different radar cross-sections used as targets. A signal acquisition algorithm based on the GLONASS satellite C/A signal was developed to verify the functionality of developed hardware. The authors were pleased to confirm that the results verified the proper functioning of the hardware and readiness of the set-up for further experimentation.

In [61] the authors further elaborated the set up. However, the main emphasis was the signal processing algorithms. The received signal is modeled as a function of two variables. One variable is the fast time t , which describes the ranging waveform and its propagation. The second variable u is the slow time, which specifies the position of the receiver and transmitter. The term “slow time” comes from the fact that the movement of the transmitter and receiver are much slower than the speed of the electromagnetic wave propagation. The specified algorithm is extended version of RMA (Range Migration Algorithm). The authors concluded that in future, effort will be made to collect more data practically and devised efficient signal processing algorithms.

The change in geometry for the image formation algorithm in [61] is provided by a track carriage flight imitator system along with receiving antenna which is placed on the rail to slide. It is suspected that this huge investment in the infrastructure is based on the requirement that for moving receiver the position and velocity of moving GPS receiver or antenna are required to be known very accurately. Simulations have shown that even 0.07 m of receiver position error can have an adverse effect on the results. The results of such simulations have been recorded in chapter 6 of this thesis. Due to these limitations it has been decided to perform experiments using static GPS receiver where the orbiting satellites will provide the requisite change in geometry.

4.3 A Review of Relevant Hardware

The incorporated hardware for GPS remote sensing purpose by different research groups and organizations along with contemporary software receiver data acquisition techniques are analyzed.

Hardware platform presented in [62] is one of the early development with remote sensing and altimetry applications. Basically the hardware was three channels GPS receiver, prepared and tested near Zeeland Bridge (Netherlands). The data acquisition card received direct and reflected GPS L1 signal using 20.46 MHz sampling frequency. The obtained results were encouraging and proposed future work included hardware upgrades to capture real time signal and advanced signal processing techniques for better results. The paper discussed and contained information regarding the hardware; however its subsequent utilization in the remote sensing domain was not adequately mentioned.

As stated earlier, J. Garrison was one of the pioneers who utilized GPS reflected signals for different applications. Primarily his research focused on highlighting contemporary uses of GPS

based remote sensing. During his tenure at NASA Langley Research Centre he experimentally proved that GPS signal reflected off sea surface contains valuable informations about the surface. In 1997, he employed a GPS receiver with delay mapped remote sensing for scatterometry observations. The receiver measured power of the reflected waveform at different time instants. Finally, for each channel power measurements were summed incoherently by the receiver [63].

Further improvements led to the development of a hardware setup which was basically different in design as compared to the above-mentioned receiver. This time using open loop data mechanism reflected GPS signals were acquired by the modified receiver, later on processed with software routines. The receiver possessed was computationally inefficient but was more capable and flexible [63].

Software GPS receivers have the advantage that up-gradation and modifications can be performed easily and thus are particularly suitable for analyzing signals received by LHCP antenna used in remote sensing environment. Software receivers can also be used in non-real-time applications, hence allowing them to apply sophisticated signal processing techniques.

The modified version of Mitel GP2021 receiver was presented by Sophia Y. Zheng [10]. The IF data of approximately 4.31 MHz was obtained through newly added front end and then passed to the ADC to perform sampling at 20 MHz. The acquisition and tracking of the digitized signal were performed through software algorithms in order to recover the navigation information.

L. Dong [64] elaborated how eighty seconds of low pass GPS signal was collected through GPS-Signal tap (name given to the device). For clear view of the satellites, the antenna was placed fixed on the top of a department room. A base band signal was obtained by sampling IF data of 15.42 MHz using sampling frequency of 4.75 MHz.

Both receivers mentioned above use software GPS receivers technique but differ in the choice of sampling frequency and IF, obviously due to different types of ICs of various competitors available for this purpose. A lot of progress has been reported lately in the performance and size of these semiconductor devices on account of their potential application in the mobile navigation market.

A team of scientists in the research centre at The University of Tokyo, Japan are convinced that GPS signals can be used for various applications other than positioning and navigation. According to them it has become possible due to development of software-based GPS receivers. The phase and amplitude of the LHCP reflected signal basically depends upon the type of reflecting material and angle of incidence. Therefore, the analysis of reflected signal provides information about the reflecting object and path delay [65]. The different applications proposed by the researchers were estimation of accurate antenna height, soil moisture and wind velocity over ocean. Block diagram of the device presented in [65] is depicted in figure 4.1.

As usual, the system developed for this purpose consisted of two antennas. One of them being RHCP (zenith oriented) to acquire direct signal and the other being LHCP (nadir oriented) to acquire the reflected signals. The signals were processed by using custom developed algorithms in Matlab®. For this purpose a prototype software receiver capable of processing reflected GPS signal was developed, which analyzed the signal in master-slave mode at user defined chip spacing and number of correlators. The approach was to observe and compare the two signals to obtain data regarding the reflecting surface. It was performed by computing chip delay or by computing difference in amplitude or Doppler difference [66].

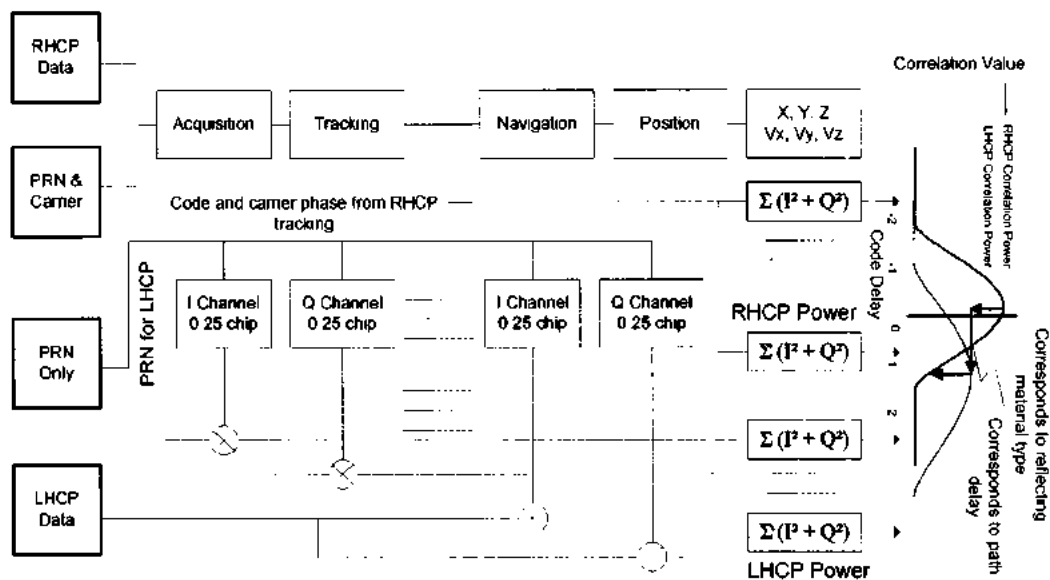


Figure 4. 1 Block diagram of the device

One of the applications was the determination of antenna height. GPS IF data was collected at BAO Tower in Colorado University using a pair of RHCP and LHCP antennas. The antennas were located on a 300m tall tower and moved from the bottom to the top of the tower while logging the data having different delay path lengths. Since the antenna travels along the tower from bottom to top the path delay increases, which was than observed. The developed algorithm computed the chip delay of LHCP signal with respect to RHCP signal in “Master-Slave” mode. Doppler frequency was however assumed to be the same for both signals. The height of the tower was successfully calculated by the analysis of reflected signal [66].

4.4 Experimental Results for Image Formation

The only relevant experimental results available have been presented by M. Antoniou et al. in [67]. The paper reports progress in the development of an image formation algorithm suitable for strip-map mode of SS-BSAR. The image has been reconstructed using real GLONASS satellites

signals through modified range Doppler algorithm (RDA). As mentioned earlier in section (4.3), during the experiments instead of using a real aircraft rail carriage flight imitator was utilized. Figure 4.2 depicts the reconstructed image of the investigated area [67]. It seems that the reconstructed image (small strip located in the middle of the picture) has been super-imposed with satellite photograph of the locality obtained from Google Earth®. According to author's statement the obtained image shows the change in magnitude of reflections/echoes from the target area through intensity variation (scale depicted in the legend located at top left).

However, an independent investigation of the result can reveal many short-comings and limitations of this technique. The resolution is not impressive and neither all features of the terrain shown in the satellite photograph of the locality are translated or exhibited, in the superimposed reconstructed image.

The GPS experimental data with the intention to generate an image was collected by the thesis author and subsequently investigated area image was formed that culminated in the successful identification of 0.5 m² spherical target. During the initial experiment the objective was to demonstrate the imaging principal rather than system capabilities. The experiment along-with the results will be explained in the fifth and sixth chapters. Moreover, the custom made LHCP antenna as compared to direct signal has opposite polarization and placed in different direction; cancel out the interference caused by direct signal. For extended ranges, the buried reflected waveform in direct signal cannot be detected, no matter how long we integrate it. Ultimately the targets in the image could not be resolved. In case of such scenario and for future undertakings, the techniques mentioned above need to be explored. The thesis author is pleased to say that, so far no research group or individual has presented or simulated an imaging system based on

reflected L5 GPS signal and generation of the synthetic aperture obtained through the movement of the orbiting GPS satellite.

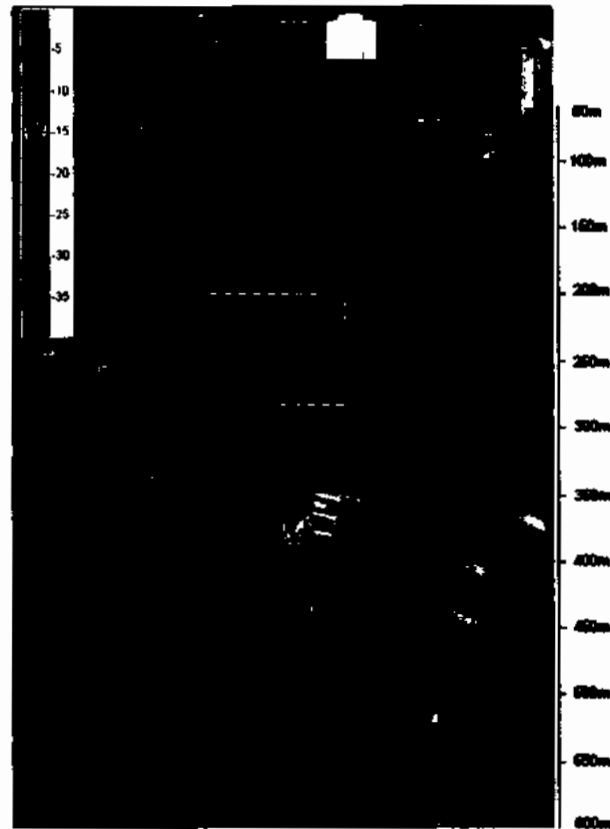


Figure 4. 2 SS-BSAR image obtained using real data

4.5 Alternate Source of Signals

Apart from GNSS, researchers have also tried alternate sources as ‘transmitters of opportunity’. In [68] a Digital Television - Terrestrial (DTV-T) signal is used for this purpose. According to the paper author’s statement, the target reflected signals were masked by the direct signals. The researchers based on dynamic compensation mechanism, proposed novel method for suppression of DPI effect caused by the direct signals. The results analysis for adaptive radar channel antenna shows, the chance of obtaining DPI cancellation upto 30 to 40 dB.. It was concluded that by

implementing the proposed techniques 30-50 dB DPI reductions is possible in addition to null steering adaptive antennas.

The research endeavor undertaken in [69] describes the feasibility study of low cost passive radar based on GSM signals. Detailed considerations regarding design of GSM waveforms, and its ultimate impact on radar system level parameter along with associated signal processing scheme were analyzed in detail manner. Further the researchers investigated extensively several ground moving targets and recorded the measurements accordingly. On the basis of obtained simulation results for numerous kind of ground moving targets the authors claimed a workable passive radar system.

Similar experimental study by P.E. Howland et al. utilizing FM radio transmitter signals is documented in [70]. It was claimed that targets far away more than 150 kilo meters from the vicinity of receiver (bistatic radar system) can be tracked. An adaptive filter algorithm was proposed for clutter reduction and mitigation of associated receiver channels interference. For the purpose of target detection along with false alarm rate, computationally efficient algorithm based on the principal of Doppler sensitive cross correlation was suggested. Performance limitations of the system are outlined in connection with real time air traffic control data.

Chapter 5

Experimental Imaging Hardware Setup

Appropriate imaging hardware platform has been designed and assembled for real GPS data acquisition and confirmation of the proposed imaging system performance. Several field experiments have been planned and performed with the imaging hardware for the system performance evaluation. The main experimental hardware consisted of: high gain antennas with attached front end and data acquisition card to capture IF data at appropriate sampling rate. This chapter will furnish some details regarding the hardware, which has been assembled to practically demonstrate the imaging system.

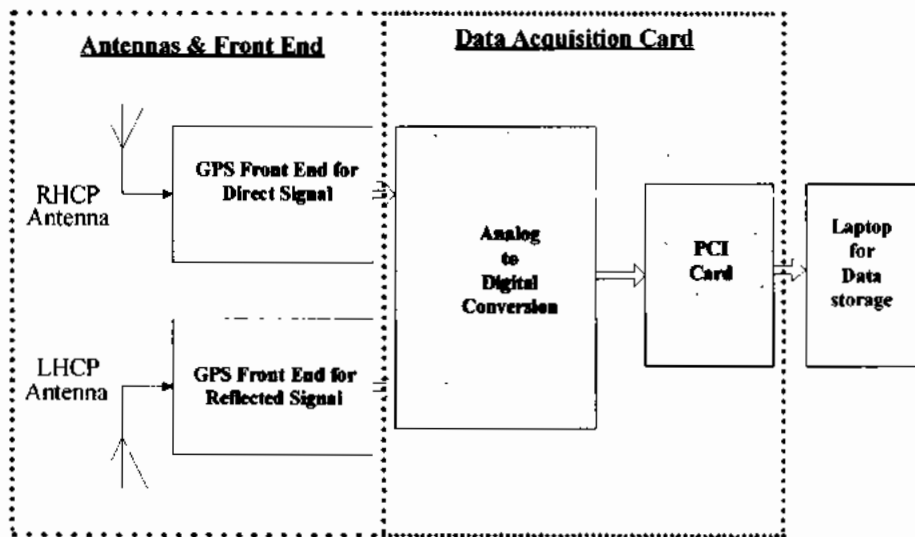


Figure 5. 1 Imaging Hardware Functional Block Diagram

5.1 Hardware Description

A high level functional block- diagram of the hardware is depicted in Figure 5.1. The three basic constituent's elements of the imaging system namely: antennas, front end and data acquisition card are elaborated in detail in following subsection.

5.1.1 Design and Development of Antennas

As evident from Figure 5.1, the employed antennas makes the initial component of the hardware setup which were designed particularly for the GPS environment. For direct GPS signals acquisition along with off the shelf patch antenna, a custom made antenna with right-hand circular polarization (RHCP) has been utilized. Similarly to receive the low power reflected signals, custom-made GPS antenna with high gain and Left-Hand Circular Polarization (LHCP) has been employed. Successful signal acquisition could not be realized due to low SNR and the weak nature of the reflected signal. The alternate option is to select and lock in a particular satellite in order to acquire the easily available direct signal using the RHCP antenna. This acquired signal will be utilized as a reference for the reflected signal. Upon successful locking-in both reflected and the direct signal shared single local oscillator.

At the time of transmission GPS signals are Right Hand Circular Polarized (RHCP). The signal become LHCP when strikes any surface [66]. Roughness of the reflecting surface, its dielectric characteristics and no. of times the signal is reflected by that surface are the contributing parameters on the basis of which the reflected GPS signal strength is measured. Attenuation rate (measured in dB) for a signal bounced back from conducting surface can be computed according to inverse square law as:

$$Attenuation_{dB} = 20 \log_{10} \left(\frac{R}{0.1} \right) \quad (5.1)$$

In the above equation the R refers to the distance between observation point and reflecting object. If R is 1km then attenuation value will be 80 dB [4]. This shows that if antenna gain is ignored then the strength of the reflected signal will be around 80 dB less as compared to direct received signal. With above value of R and receiver having 2 MHz bandwidth the value of SNR will approach around -96dB. Using antenna gain of 30 dB this value can be reduced to -66 dB. Similarly with 2 MS/s sampling rate and integration time of 100 seconds, 83 dB gain is possible with Peak Signal to Noise Ratio (PSNR) of 17 dB. Thus the antenna should have a gain in excess of 30dB. Successful effort has been made by thesis author to obtain about 15 dBi pure antenna gain and 20 dB with the help of GPS inline amplifier.

Some initial measurements with LHCP GPS antenna and limited design detail have been documented in [66]. In open literature research endeavors undertaken so far either used off-the-shelf LHCP antenna or described it only as functional block in their diagrams. A twenty one (21) turns LHCP helical antenna has been designed, assembled and tested in field experiments by the thesis author. The detail description is given in separate research paper [71]. However, the length of one meter and a sharp beam-width will render the antenna unsuitable for applications where space requirement is of paramount importance such as in an embedded or air borne environment e.g. in a UAV. Therefore, the alternate option of four element antenna array has been a better choice. Details about the antenna array specially the high gain and compact design characteristics, are elaborated in following section. Comparison of the three options considered during the design of the antenna is given in Table. 5.1.

Table 5. 1 Comparison of Different Antennas

Type of Antenna	Advantages	Disadvantages
Parabolic or Off set Dish Antenna	High Gain	The RHCP antenna at the feed point may receive direct signal and cause interference. Greater gains require larger diameters
High Gain LHCP Helical antenna	Medium Gain Excellent interference rejection between LHCP and RHCP signals	Length may be cumbersome Side lobes may increase
High Gain LHCP Helical antenna array	High Gain Compact Design	Mutual interference between elements

5.1.1.1 Basic Design Parameters

In 1947 Kraus introduced the idea of basic helical antenna. Its design parameters and detail geometric form are elaborated in [72], [73]. The geometrical parameters listed in Table. 5.2 will be used to describe the design of helix throughout this text. The desired antenna output can be achieved by changing the values of these parameters.

A number of the variables shown in Table. 5.2 will have a pronounced effect on the radiation pattern. For achieving Circular polarization value of the antenna circumference (CH/λ) should lie between 0.25 and 1.3. Similarly when $CH/\lambda = 1$ and $S = \lambda/4$ then optimum circular polarization will be achieved [73].

Table 5. 2 Design Parameters

Parameter	Description
D_H	Helix Diameter
C_H	Helix Circumference
S	Space b/w turns
A_p	Angle of the Pitch
λ_L	Wave-length
L_T	Single turn Length
N_T	No. of turns
A_L	Length of the antenna Axial
D_w	Helix wire Diameter

The simplified helical antenna diagram is shown in Figure 5.2.

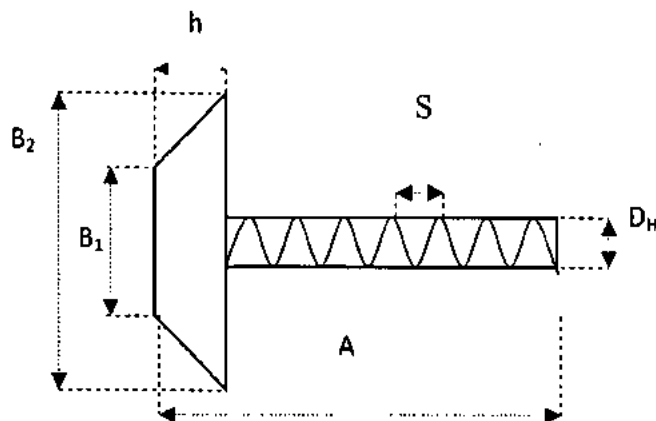


Figure 5. 2 Simplified Antenna Diagram

5.1.1.2 Input Impedance

Diameter of the wire, number of turns, pitch and radius of the helix, conductor shape and its frequency and mechanical support for the antenna are some of the contributing factors which can affect the antenna input impedance [74]. The final value of impedance for antenna working in axial mode computed by some earlier researchers is 140 Ω . But on the other hand research undertaken by Djordjevic in [74] claims that its value lies in range of 90 Ω to 270 Ω . Four such elements connected in parallel should furnish impedance in the range of a more encouraging value 22.4 Ω to 67.5 Ω . It has to be matched as closely as possible with the 50 Ω coaxial cable.

For input impedance computation normally vector network analyzer is utilized along with some other Scattering Parameters sometimes known as S-parameters. The power received at the antenna input feed point is generally represented by $|S_{11}|^2$ while S11 is used to denote input complex reflection coefficient.

Let Z_0 denote system impedance of the network analyzer then S_{11} can be calculated below:

$$s_{11} = 2 \left(\frac{z_{in}}{z_{in} + z_o} \right) - 1 = \frac{z_{in} - z_o}{z_{in} + z_o} \quad (5.2)$$

Ultimately after simplification of equation (5.2) and having value of Z_0 equal to 50 Ω , the input impedance is given by the formula:

$$Z_{in} = z_o \frac{1 - s_{11}}{1 + s_{11}} \quad (5.3)$$

5.1.1.3 Gain of the antenna

The desired output of the research effort undertaken for the design of the antenna was maximum possible antenna gain with circular polarization which is also indicated in Figure 5.3 graph. A single antenna element with 8-turns should provide around 13 dBi output gain (average of two values of Figure 5.3).

In open literature different mathematical methods are given for single helical antenna measurement of gain. The researcher has theoretically computed the gain listed in [73] using following formula:

$$G = 15NS\pi^2 \frac{D^3}{\lambda^3} \quad (5.4)$$

Using UHF frequency band the research endeavor undertaken by H. King and J. Wong listed in [75] has elaborated in detail the gain and pattern properties of 1 to 8 wavelength long helical antenna. For the terminal gain of cup shaped ground plane antenna the researcher used the following empirical relation:

$$G_p = 8.3 \left(\pi \frac{D}{\lambda} \right)^{\sqrt{N+2}-1} \left(N \frac{S}{\lambda} \right)^{0.8} \left[\frac{\tan\left(12.5 \frac{\pi}{180}\right)}{\tan\left(\alpha \frac{\pi}{180}\right)} \right]^{\frac{\sqrt{N}}{2}} \quad (5.5)$$

For expressing the Gain in dBi they applied $10\log_{10}$ to equation (5.5). The same parameters as shown in Table.5.2 have been used in equation (5.4) & (5.5).

Martin-Neira in [28] consulted the following empirical relation in order to calculate the antenna gain in dBi:

$$Gain = 11.8 + 10 \log_{10} (C_{\lambda}^2 N S_{\lambda}) \quad (5.6)$$

where C_{λ} denotes circumference and S_{λ} represents turns spacing. Gain plot for equation (5.6) is represented by circle (-o-) in Figure.5.3.

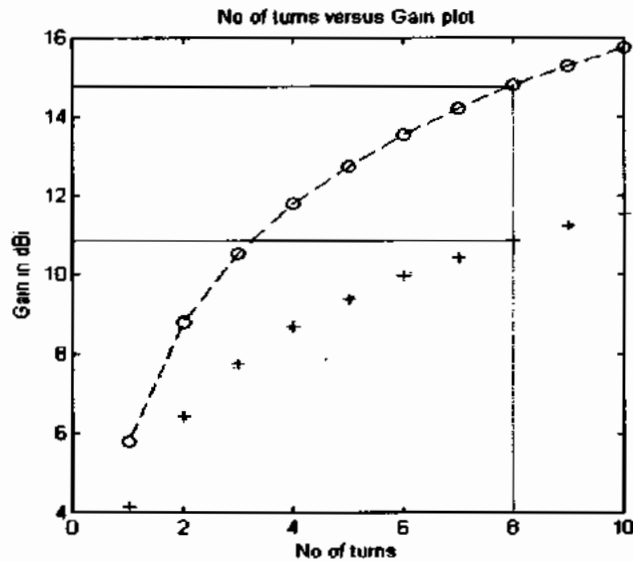


Figure 5. 3 Gain plot for a single 8 turn element Helical Antenna

However, D.T. Emerson [76] after comprehensive numerical study has pointed out and prepared a summary of different conflicting helical antenna gain claimed by researchers. On the basis of his research conclusion he has argued that actual gain value is 4 to 5 dB less than Kraus formula based result. The researcher has also revealed that increase in gain with length of antenna is not more encouraging as predicted by Kraus relation. The following empirical relation has been used in the technical literature when maximum helical antenna gain is expressed in terms of its length L and wavelength:

$$Gain(dB) = 10.25 + 1.22L - 0.0726L^2 \quad (5.7)$$

Gain plot for equation (5.7) is expressed by plus (..+..) in Figure.5.3. The researcher in [73] used the given below quasi empirical expression for calculation of half power beam width in degrees:

$$HPBW = \frac{52}{\frac{C}{\lambda} \sqrt{N \frac{S}{\lambda}}} \quad (5.8)$$

5.1.1.4 Assembly of the Four Elements Antenna Array

The finished array product with four elements helical antennas is depicted in Figure. 5.4. Individual helical antenna element contains 8-turns with 14° pitch angle. A flat squared shape ground plane with 2.5x2.5 wavelength has been employed in order to mount the four element antennas. The four elements are fixed in symmetrical position with spacing remains 1.5 wavelengths b/w their centers. The overall antenna array orientation is kept LHCP with all four elements working in similar direction. All the antennas are linked together with the center of the ground plane through single transmission line. The central line which connected all the four elements of the array goes down on the back side while the four helices are placed on the front of the ground plane. Finally from the front side at center of the ground plane a wire from each antenna is linked with 50-Ω RG 58 coaxial cable. The other end of the coaxial cable is connected with data capturing device through SMA connector. The antenna array was practically demonstrated at 1.575 GHz center frequency with ground plane of 94x94 cm.

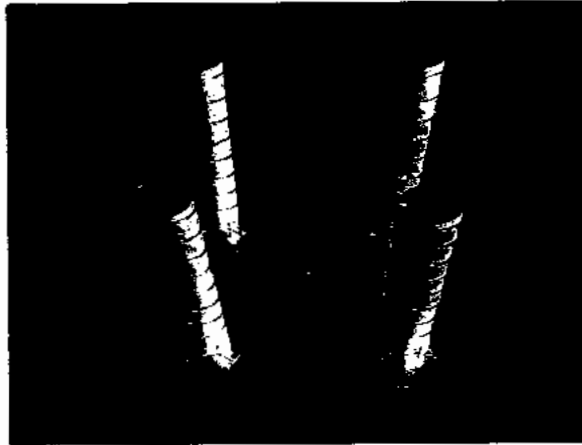


Figure 5. 4 Final Antenna Array

5.1.1.5 Testing and Gain Measurements

The antenna array has been tested through Vector Network Analyzer (VNA). The measurements for S_{11} , VSWR, return loss and input impedance comes out with value of -9.98 dB, 1:1.92, 0.20 dB, 60- Ω respectively. These results are recorded and depicted in Figure. 5.5. As highlighted by [73] the admissible value of VSWR is less than 2.

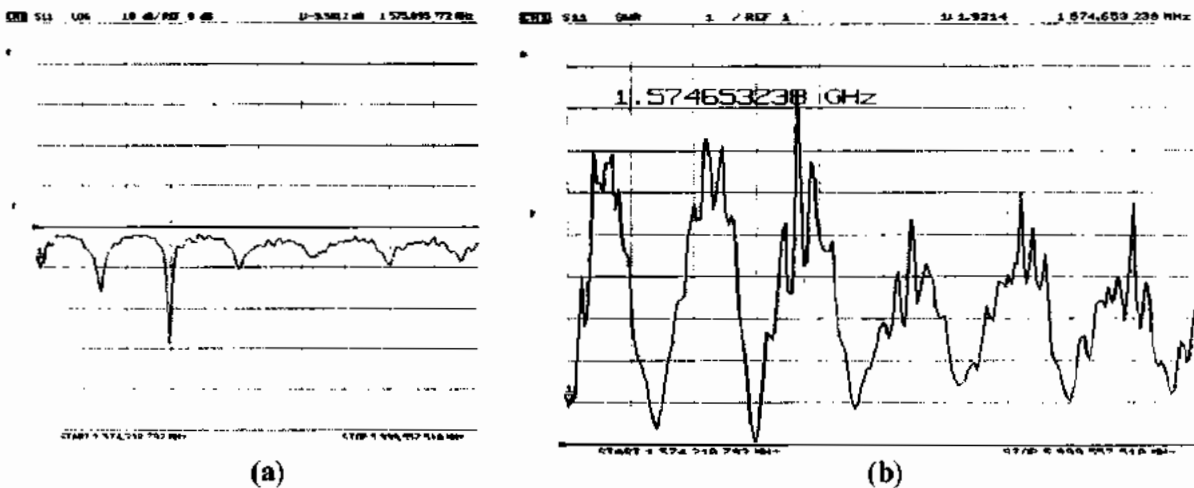


Figure 5. 5 VNA based antenna array plot (a) S_{11} (b) VSWR

Due to unavailability of adequate equipments (anechoic chamber etc.) at the time of testing, gain calculations have not been accomplished for the antenna array in a laboratory environment. However for measurement of gain and beamwidth a number of experiments has been initiated in open space.

5.1.1.6 Field Trials

The antenna array has been utilized in the imaging system, as shown in Figure. 5.6. For field experiments and analysis of the GPS signals custom made dual channel GPS Receiver, as shown in Figure 5.6, has been designed and prepared.

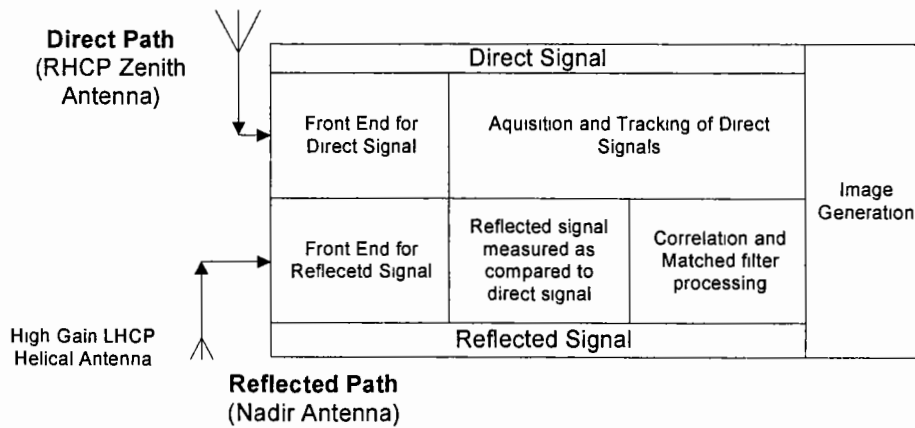


Figure 5. 6 Proposed Imaging System

The receiver zenith antenna channel received the direct GPS signal; while the second end with nadir looking LHCP antenna has been used for reflected GPS signals. For weak reflected GPS signal amplification, a 20 dB gain GPS inline amplifier was used.

As evident from Figure 5.7(a), with only one millisecond of integration time, direct signal was received having good acquisition value. Utilizing LHCP antenna to obtain similar SNR of the

direct signal, acquisition-time was rise to 200 milliseconds. Result for reflected signals is recorded in Figure 5.7 (b).

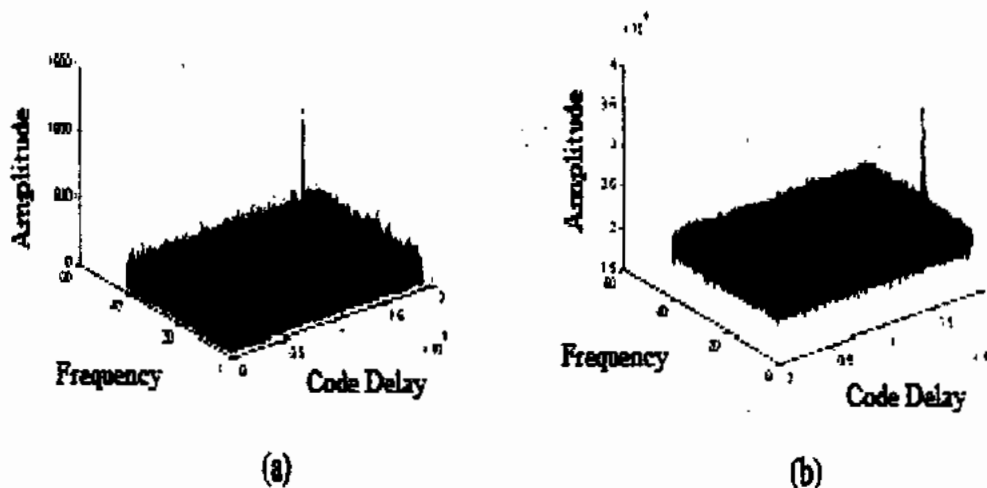
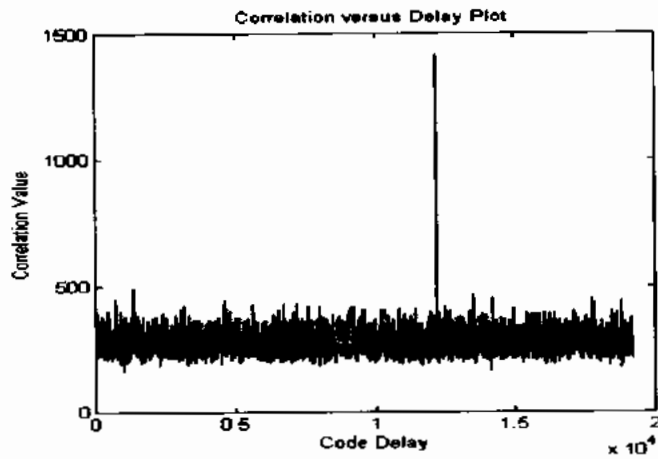


Figure 5. 7 Acquisition plot (a) Zenith antenna (b) Nadir antenna

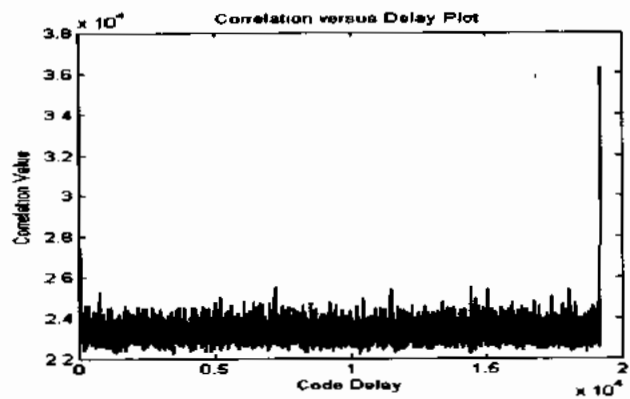
The plots in Figure 5.8 comparing the visually similar correlation value, depicted that for the 1msec case, the correlation value is 1425 and for 200msec it is 36000. Thus the reflected signal is 28dB below that of the direct signal.

5.1.2 Front End

At the heart of the imaging hardware is the GPS front end. As evident from Figure 5.1, the second part of the imaging hardware, which work in between the antenna and data acquisition card. Analogue-to-digital converter (ADC), local oscillator, mixers and amplifiers are the basic components of RF front end used in GPS receiver. The functional block- diagram of the front end is given in Figure 5.9. The front-end basically performs down conversion and signal conditioning functions.



(a)



(b)

Figure 5.8 Correlation plot (a) Zenith antenna (b) Nadir antenna

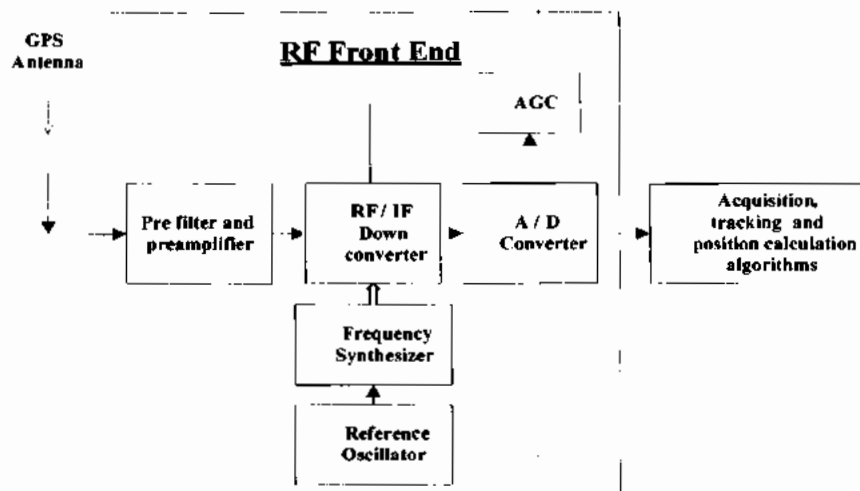


Figure 5.9 Front End Block Diagram

5.1.2.1 Signal Conditioning

The signal components which introduce interference in desired signal are removed during signal conditioning stage. This task is accomplished by Pre filter and preamplifier block of the front end. Bandpass filter is employed to remove such interfering signals, which suppress out-of-band interference. The second function is amplification of the low power received signal to achieve better results at the output of the receiver.

5.1.2.2 Down Conversion

Whereas, aim of down conversion block is to bring the high frequency (1575.42 MHz) received signal to more controllable IF signal having low frequency. By combining the input signal with a local oscillator (LO) signal, the mixer does the job of down-conversion. Well defined IF data depends upon stability and accuracy of the LO. Next the low frequency IF analog data is passed through the ADC converter to sample and change it to digital form, which is appropriate for signal processing. The no. of bits utilized for the digital representation of the signal in case of ordinary GPS receiver is usually set to 1 or 2 bits. The small number of bits simplifies the computations in the GPS receiver during later signal analysis.

5.1.3 Data Acquisition Card

The proposed imaging system in high-level block diagram format was shown in the figure 5.1. Efforts have been made to assemble a modified GPS receiver based on the concept presented and carry out testing in real time environment. Due to limited laboratory facility and unavailability of some circuit components in local market required for the data acquisition card, off-the-shelf SdrNav20 was procured from One-Talent- GNSS [77]. The Dual Front End SdrNav20 GPS data acquisition card was used to perform field trails and analyse real GPS signals is shown in figure

5.10, below. As evident one front end receives the direct signals from the satellites; the other receives the reflected signals.

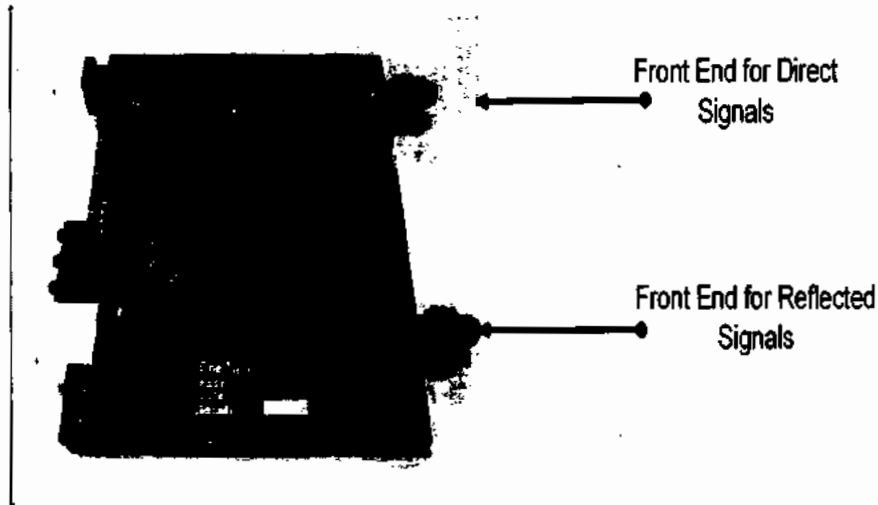


Figure 5. 10 Dual Front End SdrNav20 Data Acquisition Card

5.1.3.1 SdrNav20 Circuit Components

Main components of the data capturing device are given Table 5.3.

Table 5. 3 Main Components of SdrNav20

Component	Description
MAX21xx	The two Maxim/Dallas IC's is an L-band dual-conversion GPS receiver which down converts the RF GPS signal to a IF signal.
MAX195xx	These two IC's are employed as 8 bit ADCs
Xilinx XC6SLX4-2TQG144C	This FPGA element acts as a signal switchyard for the entire design, permitting flexible interconnection of the various design elements.
Cypress CY7C68013	It provides the necessary hardware support for implementation of a USB 2.0 high speed interface.

5.2 Experiment for Data Acquisition

As compared to ordinary radar the incoming reflected GPS signals have very low power levels. As part of the research endeavor the aim was to overcome this core problem. This was achieved by careful antenna design, suitable electronic circuit and acquisition algorithms.

In order to acquire actual GPS data with the help of proposed and assembled data capturing device and to confirm that the signal received by the LHCP antenna is in fact the reflected signal, a set up similar to Figure 5.11 was arranged. The direct signal was acquired by the off-the-shelf RHCP GPS antenna. The experiment was performed in front of a large brick building. The RHCP antenna was directed towards the satellite, while the LHCP antenna was positioned so as to receive the signal bouncing off the building at a distance of about 25m.

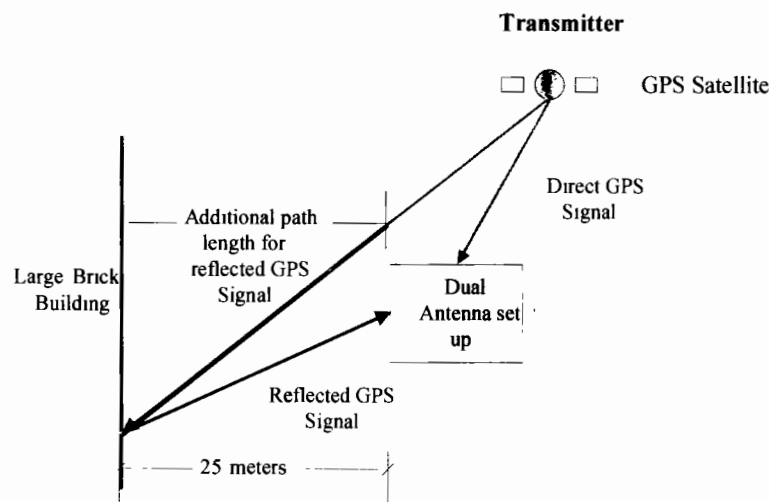


Figure 5. 11 Set up for detection of reflected GPS signals

The geometry of the LHCP antenna with reference to the visible GPS satellite played a vital part during signal reception. The most suitable satellite (in terms of signal strength and visibility) was GPS BIIRM-3 (PRN 12) and was therefore selected as the reference satellite. The satellite's elevation and azimuth angles were calculated with the help of a commercial GPS receiver. The

antenna was roughly positioned so as to receive the reflected signals of the reference satellite from the wall.

As expected a very strong signal was received with the RHCP GPS antenna, yielding good signal acquisition even for few ms of integration time as shown in Figure 5.12 (a). The comparatively weaker reflected signals acquired by the LHCP antenna required much longer integration times (200 ms) to achieve comparable SNR. The longer acquisition time resulted in the cancellation of uncorrelated noise, thus improving the SNR. As evident from Figure 5.12 the coarse frequency of both signals is the same but code offset is slightly different corresponding to the extra distance that the reflected signals have to travel and can be witnessed in Figure 5.13 in which the correlation peaks of both signals have been enlarged to facilitate analysis.

We know that in order to perform position calculations the direct signal is acquired in the GPS receiver by correlating the received code with a locally generated C/A code and varying delay and Doppler until the correlator output is maximized. The distance or range between GPS satellite and receiver is inferred from the time of occurrence of this peak value and later on position calculation are performed by suitable algorithms.

The length of one C/A code is 1023 code chips and is transmitted with a frequency of 1.023 MHz [1]. Taking into account the speed of light the length of one chip is 300 m. As mentioned earlier the signal is sampled at 19.2 MHz. Thus each code sample corresponds to about 15 meters ($3 \times 10^8 / 19.2 \times 10^6$). It is possible to distinguish between the direct and reflected signal if the difference is about 30m. During the experiment performed the difference in code samples of direct and reflected signal was 3 or 4 which came out to be about 45 to 60 meters and corresponds to the round trip distance between antenna and the large brick building or reflective

surface. Figure (5.13) compares the direct and reflected signal correlation peaks clearly depicting this path difference.

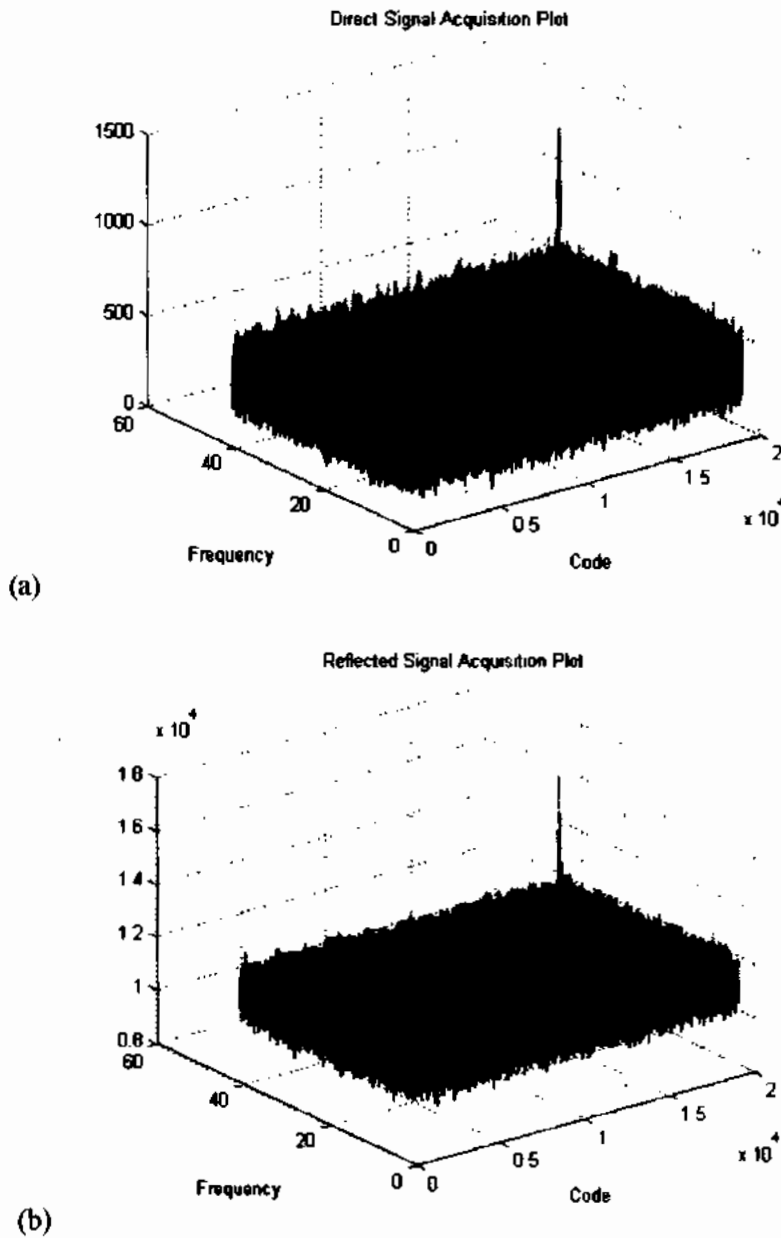


Figure 5. 12 Comparison of acquisition plot (a) (acquisition time of 4 ms) for RHCP antenna (b) (acquisition time of 200 ms) for LHCP antenna

The scale for the correlation value (y-axis) is different for both signals on account of the varying acquisition time.

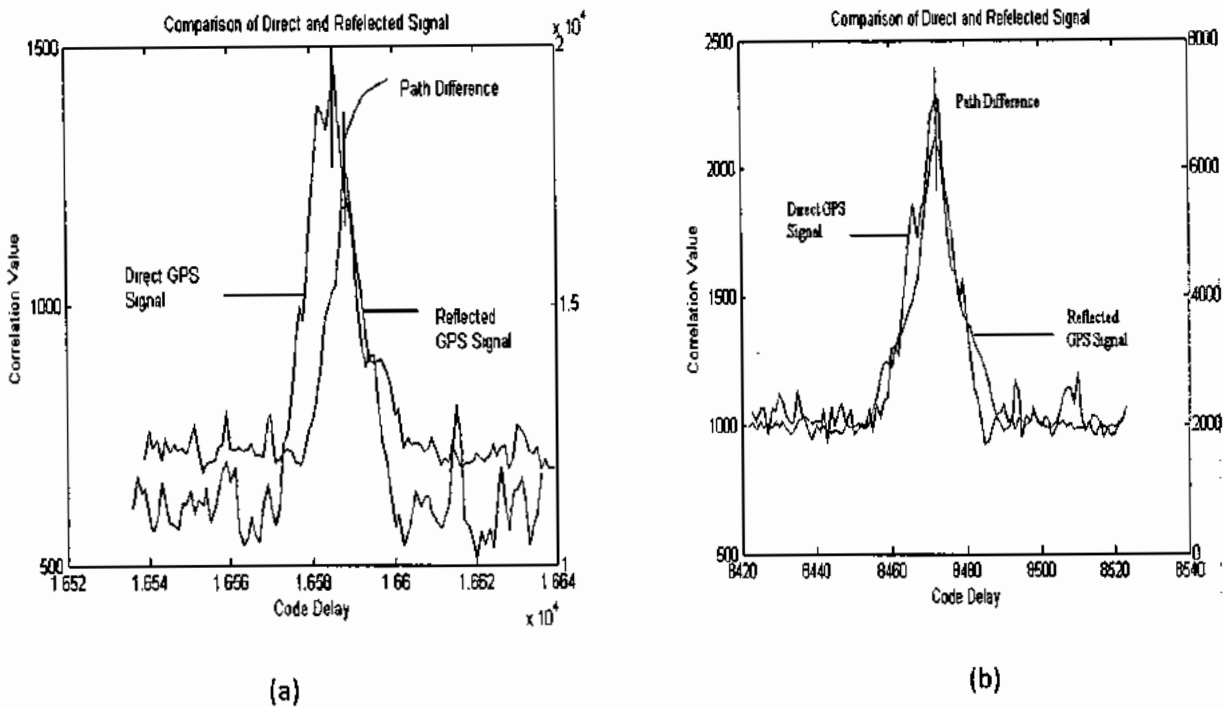


Figure 5.13 Comparison of direct and reflected GPS signals for (a) 50 m (b) 4 m (round trip distances)

In order to verify the results, GPS IF data was collected at a position of only two meters away from the building or reflecting surface. A path difference of only one code samples was observed among the direct and reflected signal as shown in figure 5.13 (b). A near specular GPS reflected signal was received suggesting an optimum geometry for reception of weak reflected signals. It is evident that by bringing the antenna set up closer to the brick wall the code sample difference between direct and reflected GPS signals is decreased.

Thus the experimental results substantiated that the signal present at the LHCP antenna is in fact the reflected signal and construction of the hardware has been successful and is ready for data acquisition for imaging purposes. It has been observed that this technique of verification of

reflected GPS signal by comparing the code sample difference is only possible if a relatively strong reflected signal is present and detected with 200 to 400 ms of acquisition time. Comparatively weak reflected signals have to be integrated for longer periods of time and unless some method of Doppler and/or phase compensation is not applied, the correlations peaks tend to enlarge and become relatively flat, possibly due to drift in phase and Doppler, and the delays cannot be measured accurately. This can be observed in Figure 5.14 in which a direct signal was integrated for one second (1000 ms) and later on for two seconds (2000 ms).

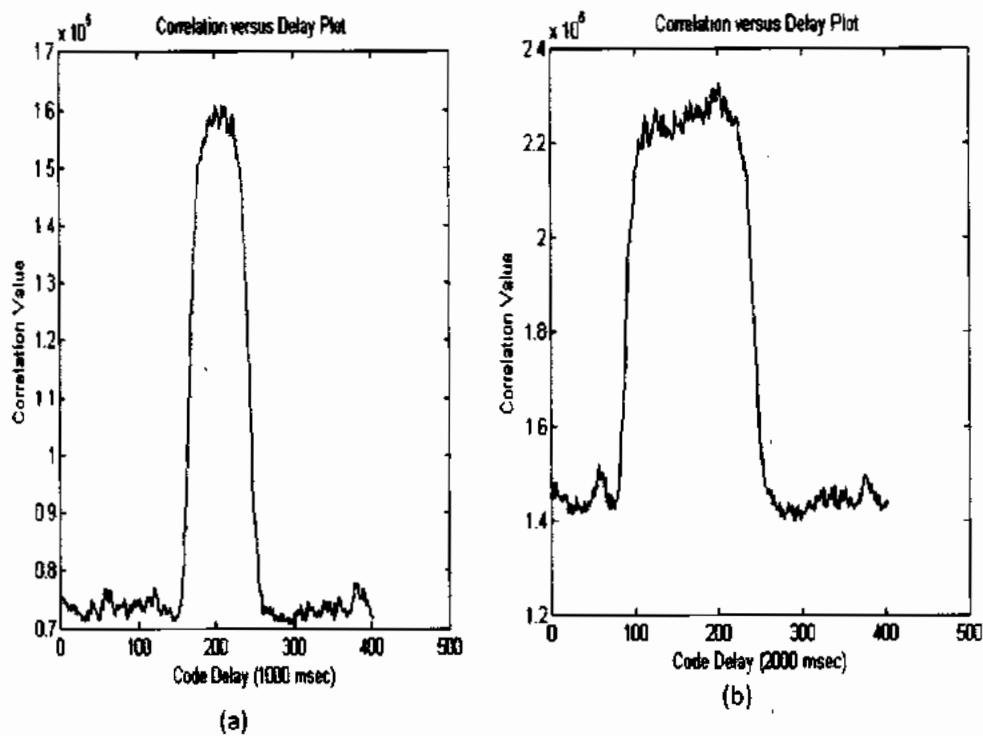


Figure 5. 14 Comparison of acquisition plot for acquisition time of (a) 1000 and (b) 2000 ms

A method for Doppler and/or phase compensation has not been applied in the acquisition algorithms. One motivation to incorporate a suitable technique might be the fact that this procedure can also be utilized as a Radar altimeter to measure height of an airborne platform or perform passive range calculations. If the sampling frequency is further increased even improved

measurement accuracy can be achieved. With minor improvements and efforts, the set up can be utilized as a basic, low cost and covert / passive (moving target indicator) MTI radar with the LHCP antenna aimed at a moving ground vehicle. However, the major objective has been is to image the area of interest, therefore this aspect or offshoot of the main research has not been explored any further.

Chapter 6

Simulations and Results

This chapter furnishes detailed simulations, carried out to confirm the idea that it is possible to image an area of interest by utilizing SAR concept and the correlation of direct and reflected GPS signals. Next it presents the results obtained during the course of Matlab® simulations and experiments performed to acquire actual GPS data. The results are compared, findings are discussed and any shortcomings are analyzed.

6.1 Initial Simulation

The simulation is initiated with development of a simple code using Matlab® 7.13 environment, for the verification of the imaging principle and concept. Later on, for improvement of the computational efficiency and to facilitate image generation under practical scenario, the code was further expanded and modified.

The simulation structure, depicted in Figure 6.1, begins with the generation and assignment of individual PRN sequence for each GPS satellite, calculation of the delay and offset introduced during transmission and finally reception by a dual front end GPS receiver. Using the matched filter concept it ends with construction of a gray scale image.

The simulation work can be mainly categorized in two stages. First stage simulation is related to the GPS space segment. This includes generation and initialization of ephemeris and PRN codes data. Computing attenuation and noise effect during the transmission of GPS signal while passing through the space is also part of the first phase simulation. While in the second part of

the simulation, the GPS receiver parameters like finding correlation, delay, match filtering and image reconstruction process are undertaken.

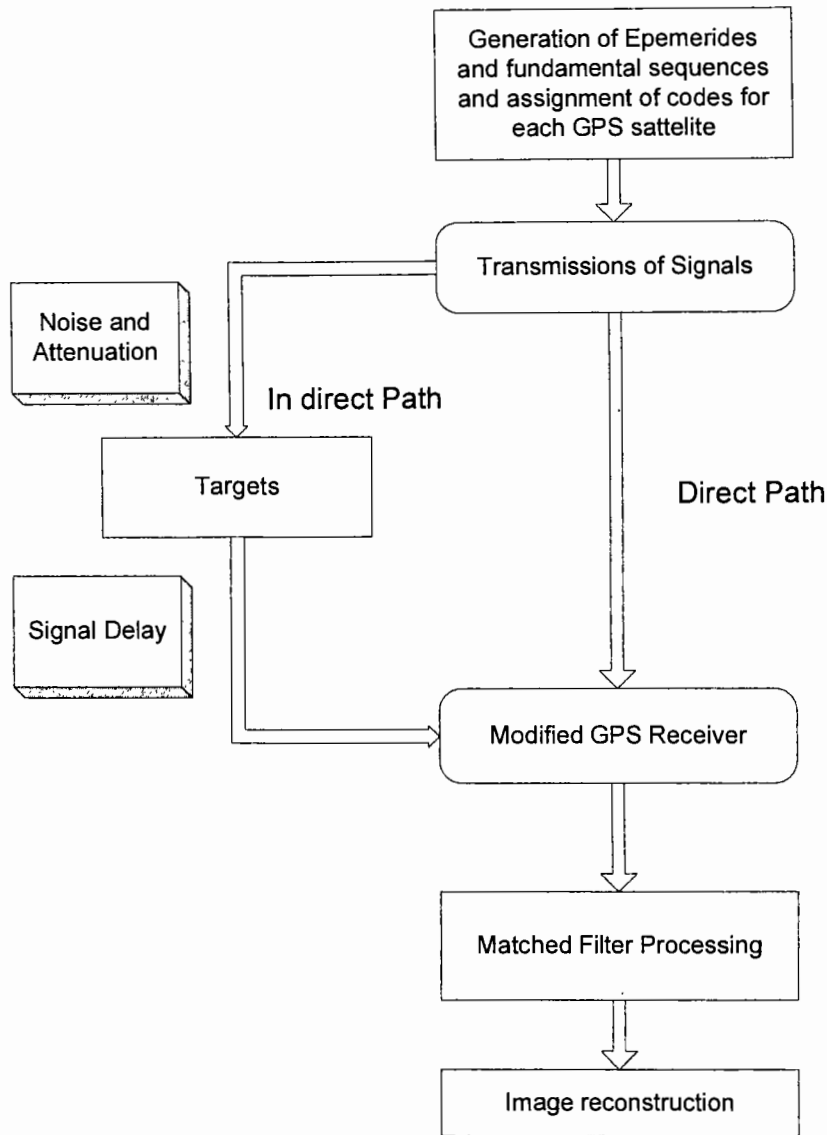


Figure 6. 1 Structure of Simulation

Later on, the code was modified in order to make it more realistic and adaptable for practical applications. Again the simulation was undertaken in two phases: the first phase was dedicated to produce digital signal utilizing the front end output of the receiver. While the ultimate image reconstruction was accomplished in the second phase of the simulation. This time more effort was made to make sure, the availability of digitized GPS signal with suitable parameters to the

reconstruction algorithms. Once the reconstruction algorithms were finalized and optimized, the simulated signal was replaced with actual GPS data.

6.2 Detailed Description of the Simulation

The code along with its constituent functions detail is given in diagram shown in Figure 6.3, with aim to gain better and quick view about the Matlab® simulation. At the beginning of the simulation the global variables, search area, sampling time, pixel size and noise are specified. Initially 2000 x 2000 meters search area containing the targets was selected. In centre of the observation area the position (0, 0, 6378000) is considered fixed to simplify coordinates transformation. These are actually the coordinates of North Pole. Three dimensional array; one each for the x, y and z coordinate is chosen for the candidate position. In the selected search area, initially two targets with positions in the ECEF coordinate system having coordinates values (200, 0, 6378000) and (-200, 0, 6378000) with 20 meters pixel size are specified. Later on the number of targets and the pixel size was modified.

6.2.1 Computation of satellite coordinates

For generation of position of satellites in ECEF (Earth-Centered and Earth-Fixed) coordinates and calculation of velocity of each GPS satellite, an array of actual satellite ephemeris data for the selected satellites was utilized. A short program was written that calculated satellites positions using parameters like transit time, ephemeris data and time of week. Normally 70 ms time is taken by the satellite signal to reach the earth. The function furnished a vector of size three containing the (xs, ys, zs) coordinates of each GPS satellite in ECEF coordinate system [78].

For description of GPS satellite or user location, the ECEF system uses three dimensional XYZ coordinates (in meters). The term "Earth- Centered" comes from the fact that the origin of the axis (0, 0, 0) is located at the mass centre of gravity. The term "Earth-Fixed" implies that the axes are fixed and rotate with respect to the earth. The Z-axis pierces the north pole, and the XY-axis defines the equatorial plane [79].

6.2.2 C/A Code Generation

For each satellite basic PRN sequences are created and assigned to every space vehicle with distinct codes. At the beginning GPS satellites undertakes code generation which is followed by the receiver upon the reception of the signal.

When the receiver performs the correlation process, it regenerates the codes locally. The fundamental characteristics of these codes have been elaborated in chapter 3 of the thesis in section (3.2.4). Through suitable Matlab® programming the individual C/A codes generation and allocation of the distinct sequence to each of the nine satellites has been done. These are biphasic codes with sequences of +1 and -1.

6.2.3 Calculation of signal delay

The signal delay is computed twice, initially for direct signal from satellite to the receiver, secondly for reflected signal from the target to the receiver. Using elementary trigonometry concept the distance between receiver and satellite represented by (D_{sr}) is computed through following simple formula.

$$D_{\text{direct}} = D_{sr} = \sqrt{(x_s - x_r)^2 + (y_s - y_r)^2 + (z_s - z_r)^2} \quad (6.1)$$

Where (x_s, y_s, z_s) and (x_r, y_r, z_r) represents visible GPS satellite and the receiver coordinates respectively. Initially the targets were positioned around 5 km distance from the receiver. The delay for the direct path expressed in seconds is computed with below given formula.

$$Delay_{direct} = \frac{D_{sr}}{c} \quad (6.2)$$

where c is the speed of light.

The combine distance from satellite to target and target to the receiver is calculated to find reflected path total distance: -

$$D_{reflected} = D_{st} + D_{tr} \quad (6.3)$$

By incorporating suitable Matlab® commands the delay is calculated for both targets: -

$$Delay_{reflected} = \frac{D_{st} + D_{tr}}{c} \quad (6.4)$$

6.2.4 Determination of code offset

Practically during transmission when GPS signal passes through the space it is delayed by number of factor before it is received by the receiver. A reference signal transmitted by specified satellite is used to simulate the delay by measuring only the difference with reference signal.

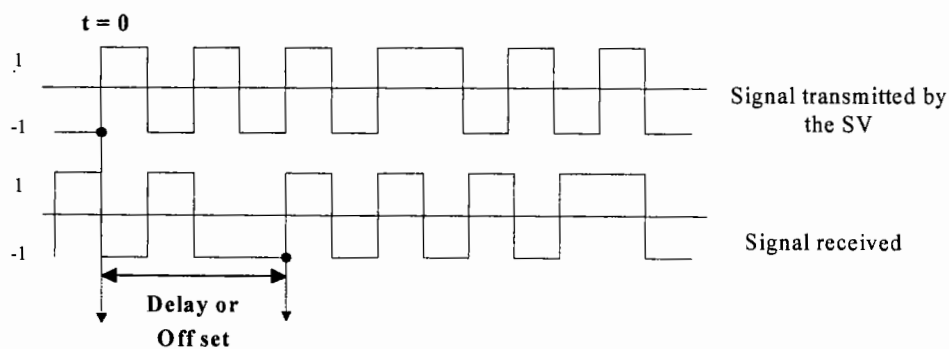


Figure 6. 2 Code offset

For finding the difference in delay a separate Matlab® function has been compiled, which furnishes the PRN delayed version. The PRN sequences along with chip rate of selected GPS satellites and time of week are used as input parameters for function. The computed difference in delay is termed as offset while the obtained PRN is known as offset PRN. The employed delay function is used to find offset for both reflected and the direct signal. Explained in the next section the offset is later on utilized to find the quadrature phase (Q) and baseband inphase (I) parts of the GPS signal.

6.2.5 Extraction of the baseband I and Q components

Using the IF signal both baseband I and Q components are extracted with help of already computed code offset. The sine and cosine of specified frequency and its subsequent multiplication with the IF signal results in I and Q components of the direct signal expressed below. Therefore: -

$$I_{direct} = d(t) * \sin \omega_0 t \quad (6.5)$$

$$Q_{direct} = d(t) * \cos \omega_0 t \quad (6.6)$$

Where $d(t)$ shows offset C/A sequence while ω_0 expressed in rad/sec represents frequency containing Doppler effect.

Before doing similar computations for the reflected signal, it is necessary to make sure that its phase is align to the direct signal. This difference between the direct and reflected signal is known as phase difference. This may occur due to the dissimilar path, where both signal have to covers unequal distance.

Using following equation the phase is calculated as: -

$$\Phi = \omega * \frac{\text{path difference}}{c} \quad (6.7)$$

Hence, the reflected signal I and Q parts are expressed by:

$$I_{\text{reflected}} = \alpha d(t) * \sin(\omega_0 t + \Phi) \quad (6.8)$$

$$Q_{\text{reflected}} = \alpha d(t) * \cos(\omega_0 t + \Phi) \quad (6.9)$$

Where α express attenuation factor discussed in section (6.2.6). For simplifying the simulation zero phase difference (Φ) is assumed.

However, in practical scenario the phase difference is required to be calculated, especially for extended ranges. This has not been implemented in the reconstruction algorithms as the initial image processing was performed at a very short range (10 meters) and the path difference in equation (6.7) was very insignificant. The measurement of Doppler frequency shift at each sample point (also called Doppler ambiguity) is also imperative. During the actual correlation campaign it was calculated during the tracking of direct signal and the Doppler ambiguity was successfully resolved.

6.2.6 Attenuation and noise

The GPS signal experiences attenuation, noise and path loss during transmission in the atmosphere similar to any other electromagnetic wave propagating through space. The indirect signal undergoes further attenuation, as part of the signal is absorbed upon striking different surfaces. At every reflection the amplitude level decreases, hence the magnitude of surface reflection coefficient is smaller than one. During the course of simulations, numerous values

were considered to observe the effect of noise and attenuation on the results of direct and reflected signals.

6.2.7 Display of image

The observation area containing targets is depicted in Figure (6.4). For simulation of the area under investigation, two arrays each having size 101 have been chosen with 20 m target pixel size. This results in an area around $20 \times 100 = 2000 \text{ m}^2$. The target size is sometimes called one pixel or square, element in the matrix. During these initial simulations the size of 20 m was an arbitrary value.

The size of the target array was modified during later parts of the simulation process in order to improve the image resolution. However, the size of target and the array can also be reduced to enhance computational efficiency. The candidate position of the target can be chosen anywhere in the matrix. The fixed position with coordinate's values $(0, 0, 6378000)$ lying in the centre of the observation area is employed to simplify coordinate transformation.

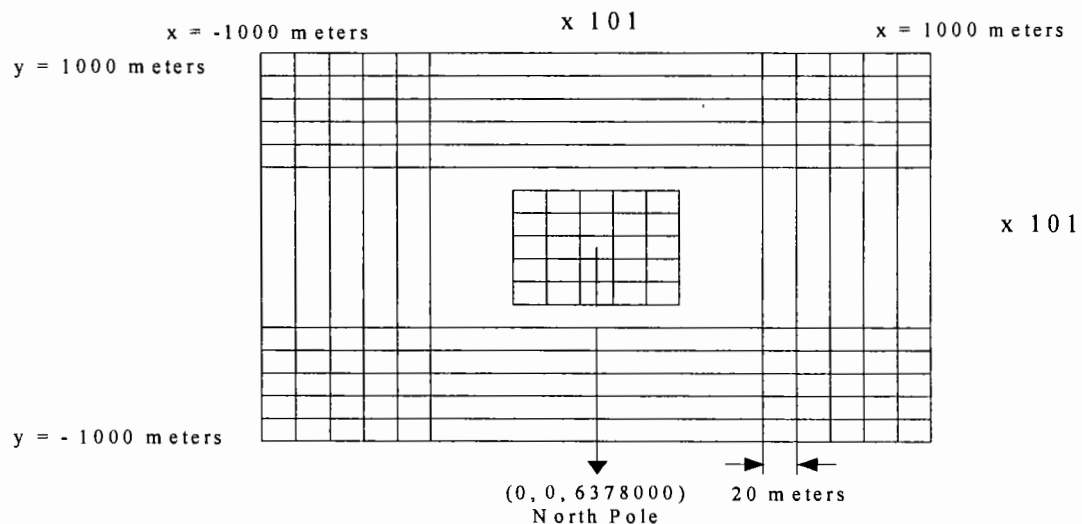


Figure 6. 4 Target Candidate position

6.2.8 Image reconstruction and matched filter processing

For better system resolution, in the signal processing a match filtering based technique is employed. This desired process is achieved in the Matlab® environment, after the multiplication of two codes bit by bit with resulting summation of all these values. This procedure is repeated and the relevant value is stored in the 101 x 101 matrix for every epoch or sample, as shown in Figure (6.4). The procedure resemble to a matched filter process, in which a given matrix is searched for every sample in time. In fact, delayed versions of the signal are multiplied with original signal and obtained value at each instant of time is added. This resembles with integrating over the sampling period. Greater or maximum correlation value will be achieved upon reaching the target location. It is apprized that the values for quadrature phase (Q) and the baseband inphase (I) components are changed to similar magnitude using below mentioned simple equation.

$$\text{Equivalent Magnitude} = \sqrt{I^2 + Q^2} \quad (6.10)$$

A grey-scale image is obtained utilizing above highlighted information's. Grey scale image is basically combination of white, black and grey shades of colours. The data is inverted and normalized by the Matlab® function during the above mentioned simulation. In case there is no target, the pixel or square of the matrix is displayed as white, otherwise is shown as black when there is maximum correlation. However, it can be vice versa as well. Hence the obtained image exactly pinpoints the target in the candidate position with required coordinates.

6.2.9 Simplifications and assumptions

Numerous assumptions and simplifications have been made with aim to make possible the simulations. The target is supposed as a fixed point scatter with the application of point target resolution theory. Furthermore, it is assumed that the target will reflect all the signals towards the receiver and the reflection coefficient is also assumed to be one. In order to simplify overall geometry and reduce coordinates transformation as well as spatial referencing errors, the location of targets are supposed to be located near the North Pole. It is further assumed based on the understanding that the signal strength will be improved during the correlation process, reasonable value of attenuation and zero phase difference.

6.3 Modifications and Improvements to the Code

In order to materialize the intentions of putting together a practical imaging system, it is imperative to work on real sampled data obtained from a GPS antenna through a RF front-end and an ADC converter. However, in the initial phase of developing the signal processing algorithms it is not optimal to use real sampled data, because it is not only impossible to control the received signals but also difficult to know all properties of the received signals. A Matlab® code was compiled that generated a signal similar to the GPS base band signal with selectable IF (few MHz) and other parameters like noise and attenuation. The signal can be uploaded in the simulation through routine Matlab® techniques in form of a file. The reconstruction engine was also modified and will be explained in a detailed manner.

For the enhancement of computational efficiency one of the reliable ways is to switch from interpretive Matlab to compiled code environment. In this regard modular approach has been

adapted to speedup the program execution. Utilizing the Borland C++ Builder, a GPS signal is separately generated with C++ code editor. The code signals generation phase is increased approximately 9 times better by employing the mentioned approach. The reconstruction function is still compiled in Matlab® and can be converted to C++ code as a future project.

In order to make the developed reconstruction code appropriate for use in practical scenario, modifications were made accordingly. For the computation, vectors/linear arrays instead of multi dimensions arrays were incorporated with the aim to enhance computational efficiency. The block diagram of the revised reconstruction algorithm is depicted in Figure 6.5. Only the difference, as compared to the initial code is elaborated as many functions and sub-routines are similar.

Signal segmentation is included among the options which could be opted for the improvement of computational efficiency. This approach was introduced while simulating stationary and low speed moving GPS receiver. Parameters like time of week, frequency and phase were updated accordingly with careful chosen data, while the rest of data was discarded. In fact only part of the received is used to reconstruct the image. Although, the method requires minimum computation time but image quality can degrade.

Under sampling or sub sampling is another simple and reliable method that can be used to enhance computational efficiency of the reconstruction code. To carried out sub sampling (up to level of 10), “resample” Matlab® routine was executed during the simulation, which reduced amount of process data. Without compromising image quality the adopted method increased computational efficiency to considerable extent.

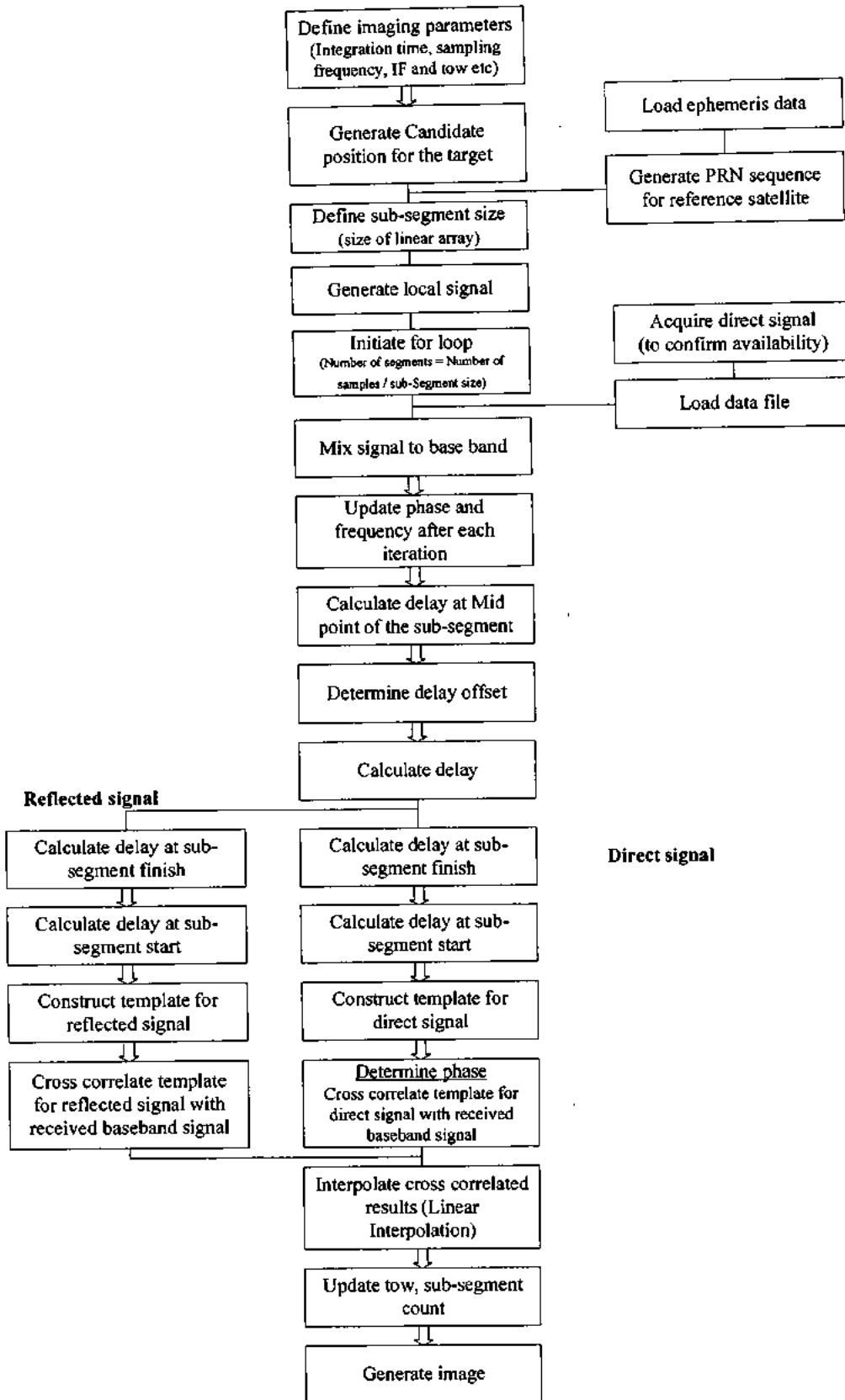


Figure 6. 5 Block diagram of the modified reconstruction engine

6.4 Preliminary Results

The parameters given in Table 6.1 were used during Matlab® simulations. For simulating various imaging scenarios under different condition some of the parameters were changed accordingly.

Table 6. 1 Simulation Parameters

Parameter	Value
Integration-Time	0.1 seconds
Attenuation-Factor	0.5
Noise	0
First Target-Coordinates	[200, 0, 6378000]
Second Target-Coordinates	[-200, 0, 6378000]
Receiver-Coordinates	[5000, -5000, 6378000]
Receiver-Velocity	[300, 0, 0]
Satellites-Tracked	1, 7, 9, 14, 16, 22, 25, 26, 27
Reference-Satellite	4

6.4.1 Case I

The values stipulated above in Table 6.1 were utilized while the first simulation was conducted.

In the resultant Figure 6.6 with reasonable spatial resolution the two targets are identified.

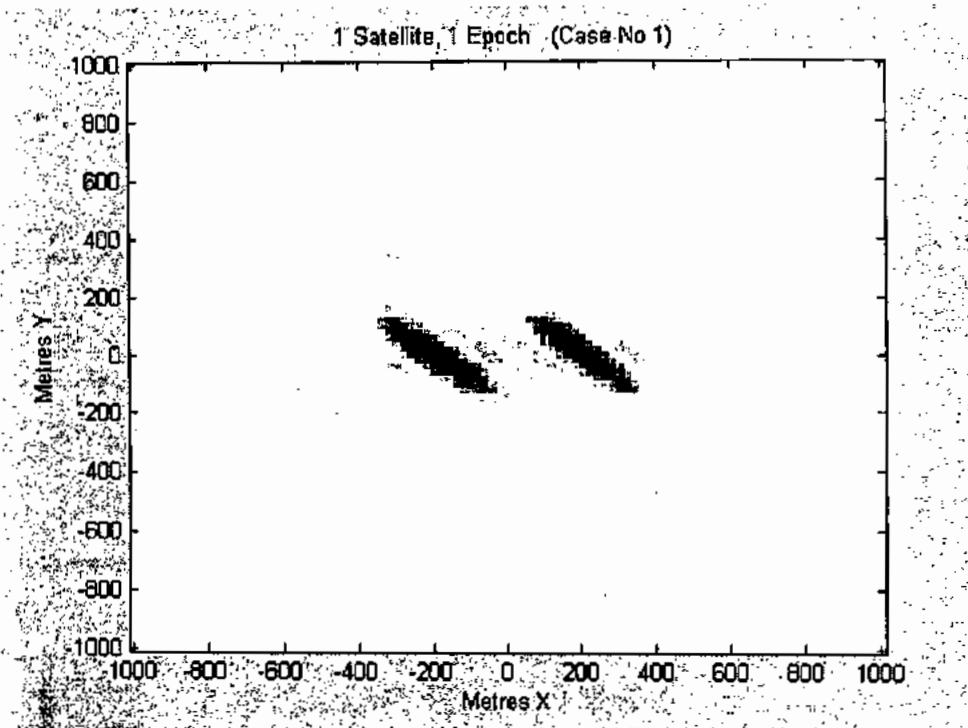


Figure 6. 6 Integration-Time 0.1 sec (without noise)

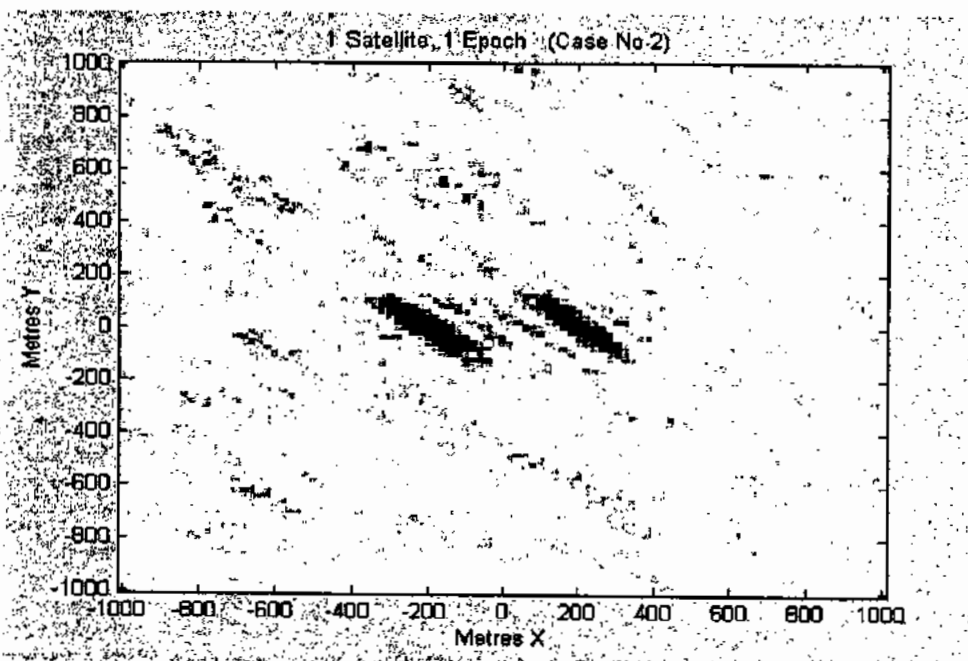


Figure 6. 7 Integration-Time 0.1 sec (with 16 dB noise)

6.4.2 Case II

This time noise of 16 dB was induced while all the others parameters were kept constant as per Table 6.1. Background noise can be seen in Figure 6.7, but the targets are still recognizable.

6.4.3 Case III

Simulation was executed with increase in integration time (0.2 sec) parameter only. As compared to previous simulation improved results and resolution was achieved but the execution time was longer, result shown in Figure 6.8. The increment in integration period made it possible to get large number of samples and cancel out the induced noise. Increasing the integration time also results in more synthetic aperture for the dynamic imaging device and better resolution.

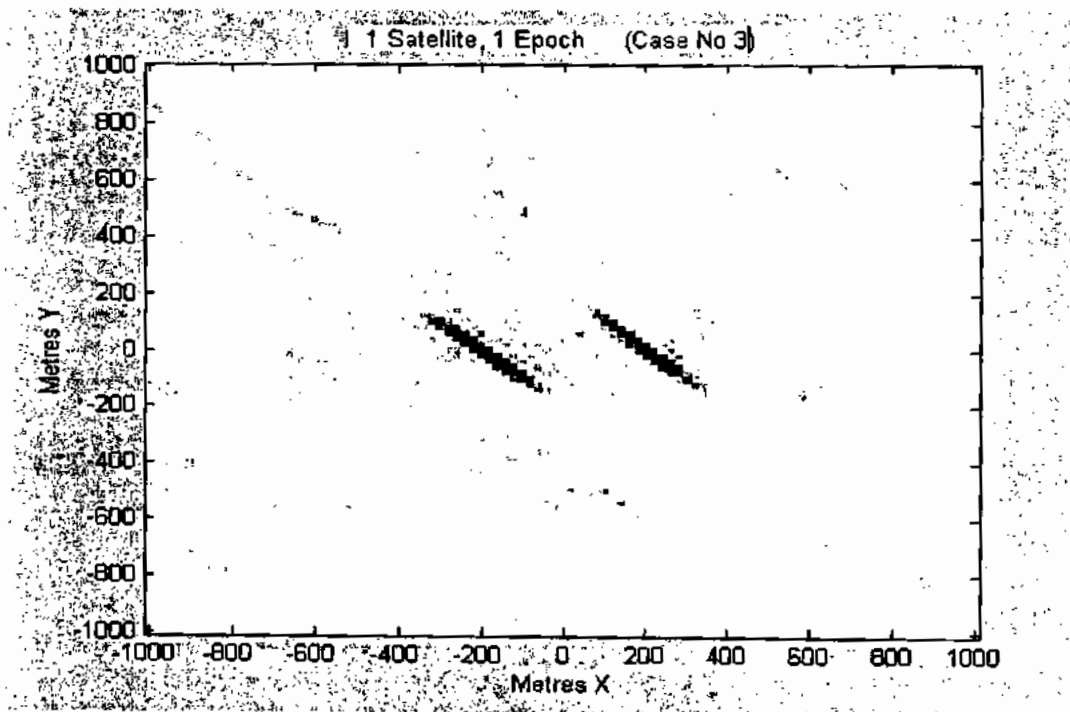


Figure 6. 8 Integration-Time 0.2 sec (with 16 dB noise)

6.4.4 Case IV

In the next course of simulation targets movement with different speed was considered, in order to verify what type of targets can be resolved with this technique and observe the effects of target dynamics. No noise was induced and integration period of 0.1 sec was utilized. The anticipated results are depicted in Figure 6.9.

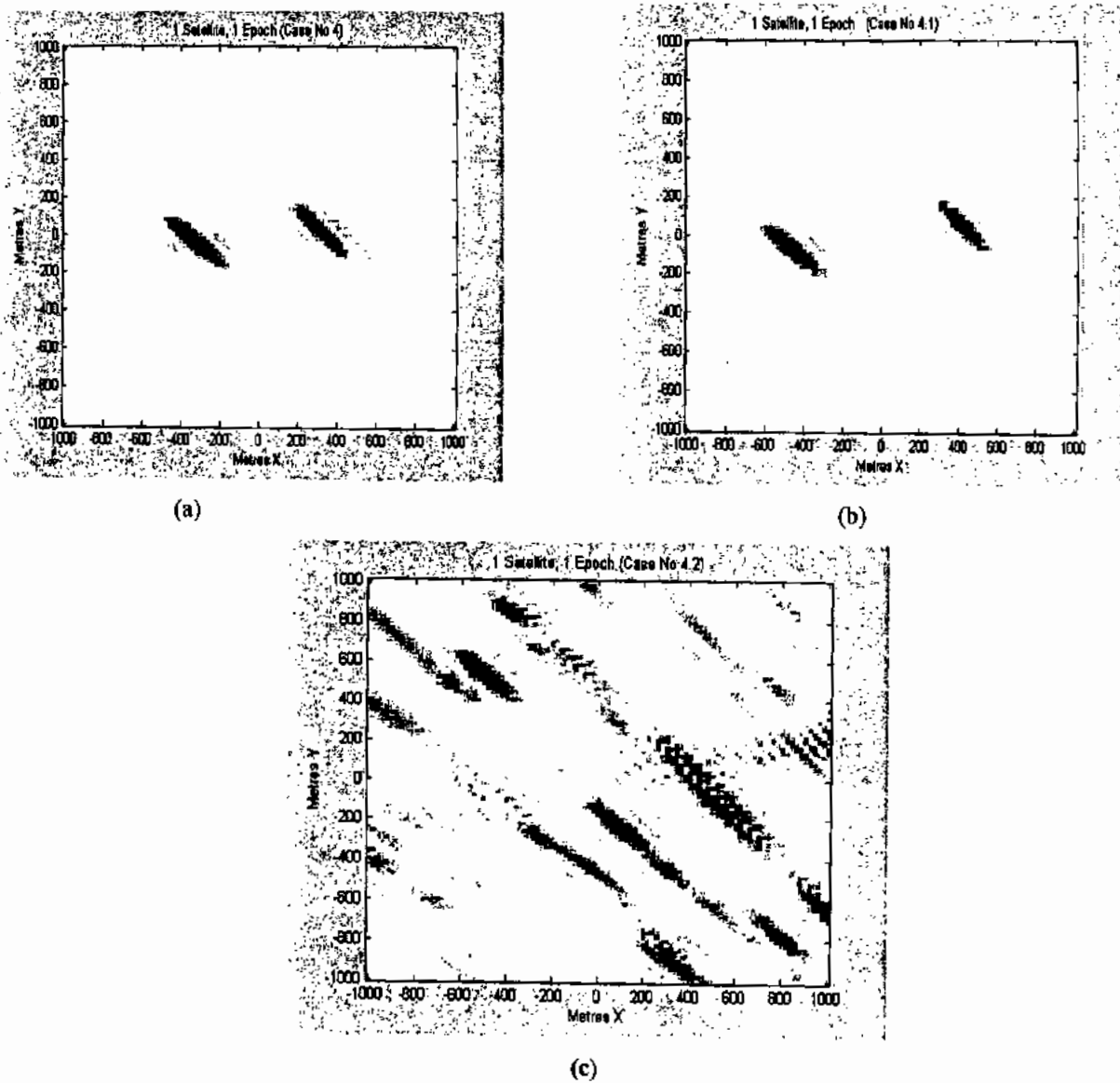


Figure 6. 9 Comparison of diagrams for Integration-time 0.1 sec & Target speed (a) 10 m/s (b) 20 m/s (c) 100 m/s

As can be observed from Figure 6.9 (c) the targets could no longer be visible when the speed was increased to 100 meters per second. Hence it can be deduced that this technique is best suited to effectively recognize static and slow moving targets i-e ships/ground vehicles.

Unexpectedly, when the integration time was increased in above case in the presence of noise, the targets could not be resolved. It has been stated in [80] that the power budget of SS-BSAR with GNSS NCT is noise rather than interference limited. Thus it is imperative to keep the noise as minimum as possible for satisfactory results. One of the methods is by employing high efficiency low noise amplifiers at the receivers input stages. Extraction of useful data from low power reflected signal in presence of noise remains the biggest challenge in the remote sensing environment.

Many interesting results were observed during the initial simulation process and are as follows: -

- 1) It is indeed possible to generate an image based on SAR concepts and utilizing matched filter techniques with the correlation of direct and reflected GPS signals.
- 2) An increase in the observation time translates into more number of samples, thus resulting in better simulation results and improved resolution by cancellation of uncorrelated noise.
- 3) While observing the effects of targets dynamics it was inferred this technique is best suited to effectively recognize static and slow moving targets i-e ships/ground vehicles, within the context of present computational resources.
- 4) During the simulation it was proved that an increase in receiver speed results in improved resolution. It is apprized that enhanced speed translates into an increase in synthetic aperture.

During execution of initial simulations it was concluded that the compiled Matlab® program and algorithms computational cost is high and also require large memory.

6.5 Simulation Results for Different Imaging Scenarios

6.5.1 Ground vehicle borne (low velocity) receiver

As mentioned in section (2.4.1) it is also possible to provide change in geometry with the receiver mounted on a moving terrestrial platform, for example, a ground vehicle or car. The total simulation time (T_s) for signal generation was selected as 100 seconds and net integration time (T_n) in the reconstruction algorithms was chosen as 10 seconds. This was made possible with the help of segmentation introduced in the code. Simulations were performed by varying the appropriate parameters and the results and conclusions have been recorded.

Simulations were performed for different receiver velocities; the velocity was decreased from 100, 20, 10, 5, 4, 3 to 2 m/s. The targets were resolved clearly for all receiver velocities except for 2 m/s. In next phase simulations were performed for a fixed receiver velocity (5 m/s), but a receiver position error of 0.01, 0.03, 0.05, 0.06, 0.07 and 0.1 meters was induced. Results are depicted in figure (6.11). It was evident from the results that noise started to appear in background when the receiver position error was 0.05 m, but the targets were still visible, however there was no target present when the receiver position noise was increased to 0.1 m.

Hence it is concluded that it is possible to generate an image with receiver velocities as low as 3 m/s (about 11 km/h), with a net integration time (T_n) of at least 10 seconds, but a receiver position error of only 0.07 meters renders the target undetectable.

Figure 6.10 compares the results for different receiver velocities with the integration time mentioned in the preceding paragraph. It is also possible to generate an image even with lower receiver velocities, but only at the cost of increased integration time and with the present

hardware configuration the data acquisition of more than 100 seconds is not possible. However, even these lower velocities have been simulated while finding the appropriate time for integration concerning a static GPS receiver.

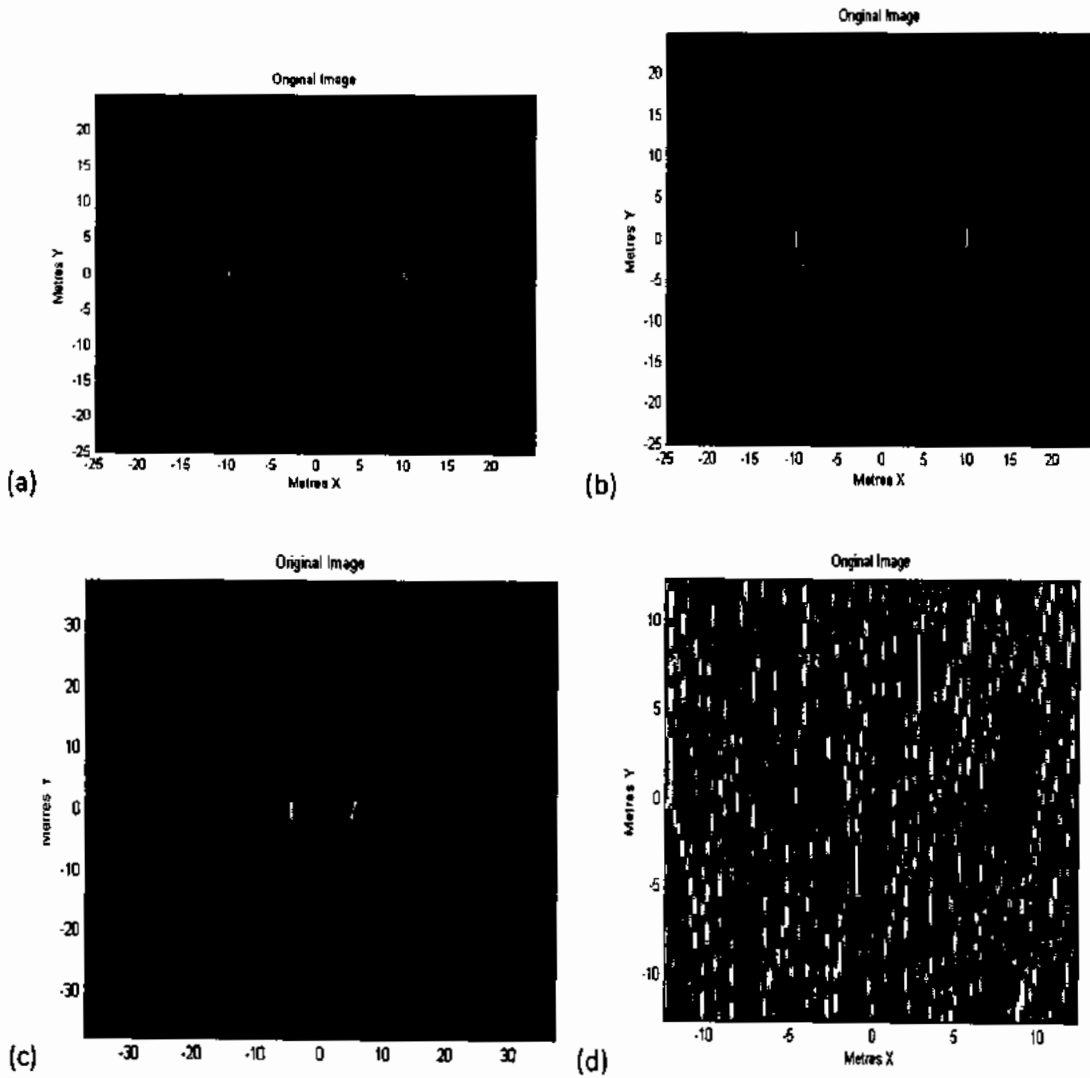


Figure 6. 10 Comparison of results for receiver velocity of (a) 20 m/s (b) 5 m/s (c) 3 m/s and (d) 2 m/s

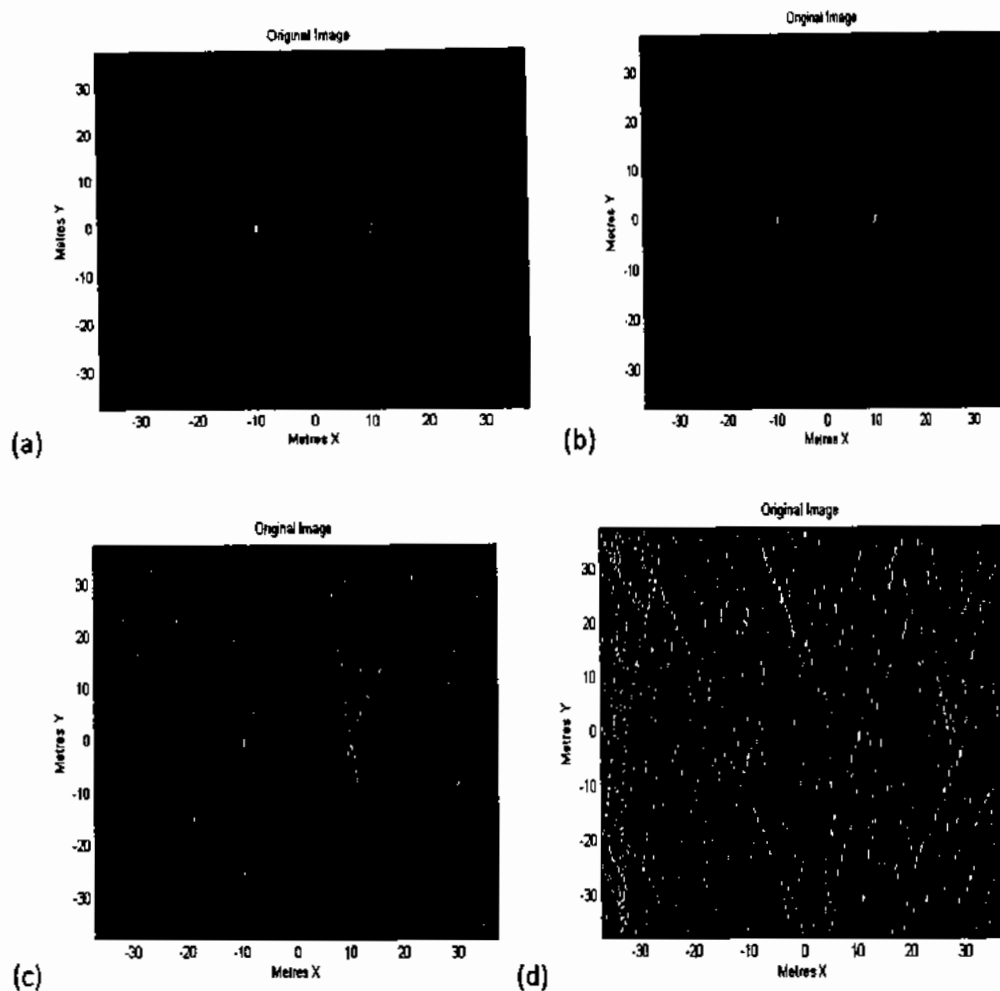


Figure 6. 11 Comparison of results for receiver position error of (a) 0.01 m (b) 0.05 m (c) 0.07 m (d) 0.1 m

Superficially, this type of scenario seems very attractive, because a simple platform such as a car can be used to provide change in geometry and the dual frequency GPS data acquisition device can be utilized despite the 100 seconds limit for data acquisition. However, the error induced due to uncertainty in receiver position renders this method unsuitable, at least for this research. It will be interesting to explore this method in future research undertakings, by correcting the receiver position and velocity errors using suitable methods.

6.5.2 Results for static receiver simulation

As mentioned in section (2.4.1) it is also possible to provide change in geometry by the orbiting GPS satellite in case the receiver is kept stationary. It was learned during the course of simulations that the optimum integration time is 10 seconds for a receiver velocity of 200 m/sec, a compromise between computational efficiency, resolution and size of collected data. The receiver covers a distance of 2km during this period and the image reconstruction only requires a few minutes for small target arrays. In order to find the optimum time required for image reconstruction in case of a static receiver, a different signal was generated with the help of GPS signal simulation code with a step by step decrease in the receiver velocity and increase in the integration time (T_s). In order to ensure that the targets are resolved, the net integration time (T_n) was kept at 10 seconds. This was made possible with the help of segmentation introduced in the reconstruction engine to deal with signals having longer duration. The other parameters were changed as shown in Table 6.2.

Table 6. 2 Optimum time for static receiver simulation

Total integration time (T_s, s)	Net integration time (T_n, s)	Receiver velocity (R_v, m/s)	Number of segments (SS)	Skip time (T_{sk}, s) (per segment)
10	10	(200, 0, 0)	1	0
100	10	(20, 0, 0)	10	9
200	10	(10, 0, 0)	20	9
400	10	(5, 0, 0)	40	9
800	10	(2, 0, 0)	80	9
1600	10	(1, 0, 0)	160	9
3200	10	(0, 0, 0)	320	9
3600	10	(0, 0, 0)	1000	3.59
7200	10	(0, 0, 0)	2000	3.5950

As observed from Table 6.3, with the integration time at 3200 seconds and number of segments equal to 320, the targets first appear to be resolved with a stationary receiver. An increase in the number of segments to 1000 revealed an improved image. It was noted that a further increase in the number of segments to 2000 and integration time (T_s) to 7200 resulted in enhanced image quality and resolution.

Thus, the simulations highlighted to obtain acceptable spatial resolution and recognized the targets; minimum integration time of 3600 seconds (one hour) is needed. However, for sub-meter level resolution, continuous two hours of data would be required. Another interesting finding was that the data should be divided into maximum possible number of segments. For example 2 hours (7200 seconds) of data was divided in 2000 segments with skip time (T_{sk}) equal to 3.5950 seconds and dwell time (T_{dw}) equal to 0.050 seconds (50 ms). With this arrangement the total data processed was only 10 seconds. However, during practical applications, where the reflected GPS signal is very weak, at least 100 ms of T_{dw} (dwell time) for shorter ranges and 400 ms for extended ranges is desirable. It is deemed necessary for the acquisition of weak reflected signal by correlation and thus cancels out uncorrelated noise. Care should be exercised in selecting the T_{dw} , as enhanced dwell time may compromise the computational efficiency and also result in ground clutter masking the targets. On the contrary, insufficient T_{dw} will not result in the acquisition of weak reflected GPS signal.

Figure 6.12 shows the results obtained by integrating over 7200 seconds with Figure 6.12 (b) depicting the deconvolved image. The two 10 cm targets appear to be resolved with sub meter range resolution. Figure 6.13 illustrates the same image in different shades of grey perspective along-with the PSF.

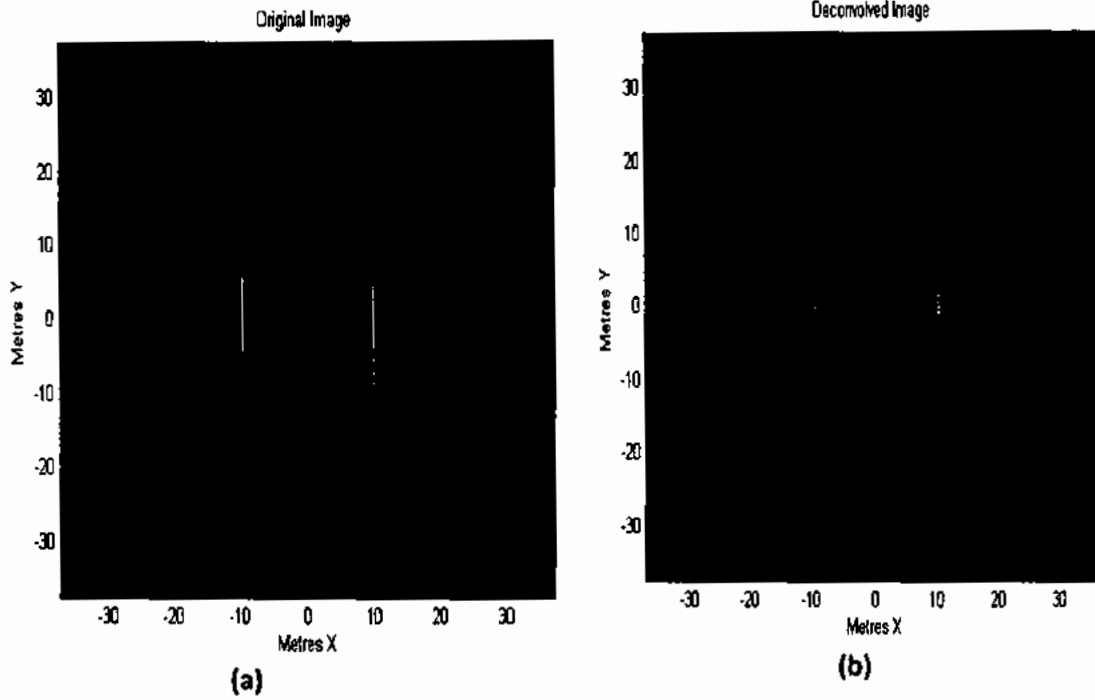


Figure 6. 12 Simulation results for 7200 seconds (a) Original Image (b) Deconvolved image

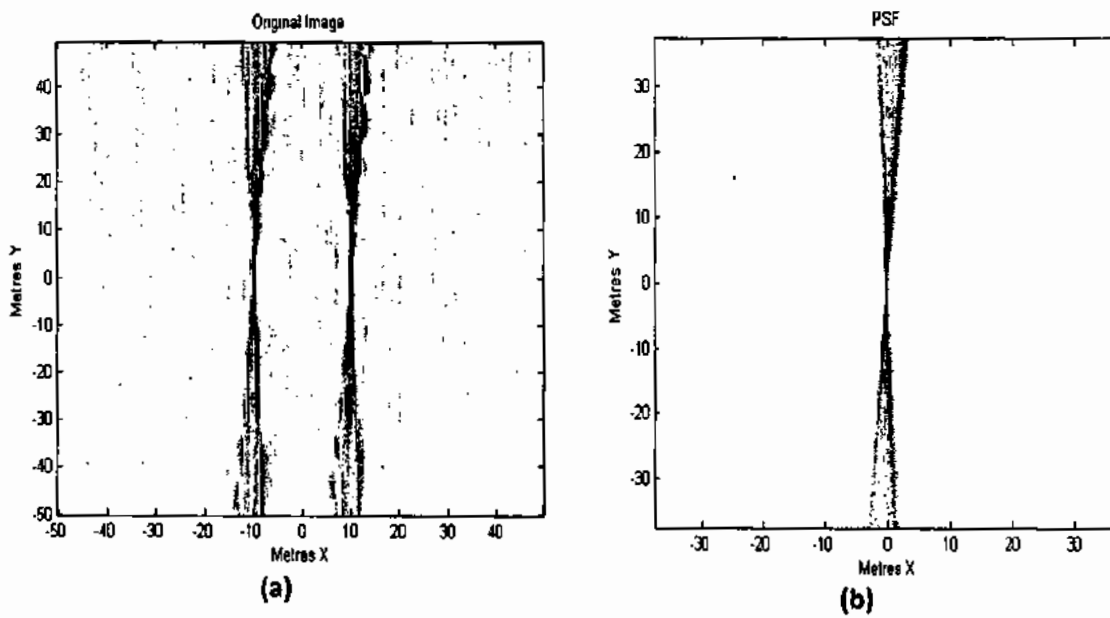


Figure 6. 13 Simulation results for 7200 seconds (a) Original Image (b) PSF

It has been mentioned earlier that the resolution has direct concern with variation in geometry of the orbiting satellites. It will be interesting to note the effect of total integration time on image quality and resolution. An increase in integration time translates into more synthetic aperture. The self explanatory Figure 6.14, depicts how the resolution deteriorates as we decrease the total integration time.

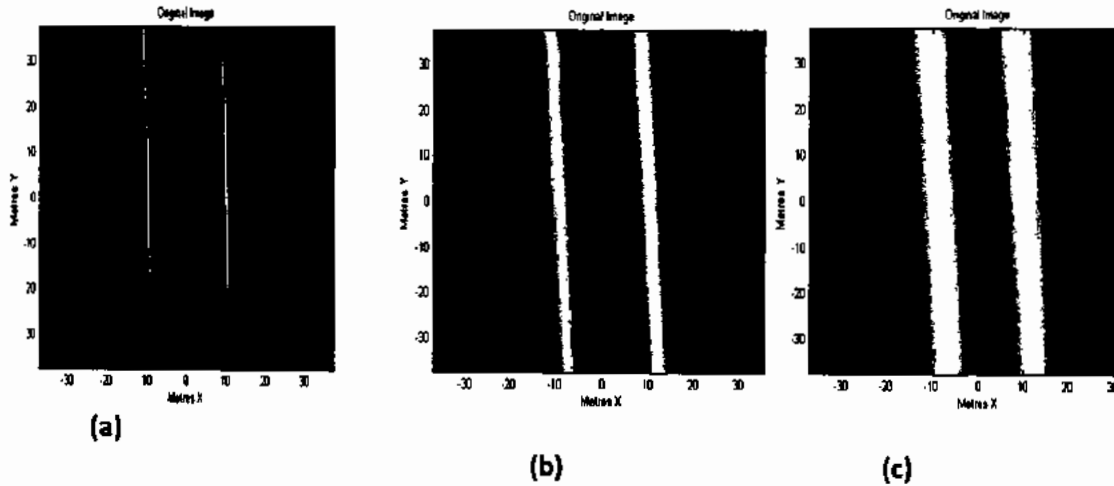


Figure 6. 14 Comparison of results for Ts of (a) 2400 s (b) 1000 s (c) 300 s

6.6 Further Simulation for enhancing Resolution

A matrix with size of 400 x 400 along with pixel dimension of 25 x 25 cm was chosen to check, best possible resolution which can be obtained during the simulation. A 20 m² observation area containing four point targets, with coordinates value of (10, -10, 6378000), (-10, 10, 6378000), (10, 10, 6378000) and (-10, -10, 6378000) are positioned at the corners in the area of interest. Each conducting point reflector was modelled as a sphere having reflection coefficient of one and 10 cm effective radius. This particular value for the radius was selected to demonstrate that it

is possible to detect a target comparable to the 20 cm wavelength of GPS L1 frequency. It was assumed that the antenna for reflected signals has a gain of 30 dB and that the direct signals can be suppressed by 70 dB. The coherent integration time was set to 100 seconds and later on the same results were obtained with 10 seconds of net integration time, but with help of code segmentation as explained earlier.

6.6.1 Image generation

It was mentioned earlier that the strength of the reflected signal depends upon the surface roughness and the dielectric properties of the reflecting object and the number of reflections. Following the inverse square law, the signal reflected from a conducting sphere with a radius of 10 cm would attenuate at a rate (expressed in dB) of approximately $20 \log_{10}(R/0.1)$, where R is the range from the 'point reflector' to the observation point. For example, at a range of 1000m the attenuation will be about 80dB below that of direct signals received by a RHCP antenna. For a receiver bandwidth of 2 MHz, the SNR would be about -96dB. This is improved to a figure of -66 dB due to the antenna gain (30dB). At a sampling rate of 2 MS/s we have 2×10^8 samples during the 100 seconds integration time, which should yield an improvement of 83 dB, giving an expected PSNR in the reconstructed image of 17 dB.

The generation of image with the modified reconstruction algorithms (receiver velocity of 200 m/s and sampling frequency of 2 MHz), as shown in Figure 6.15(a), revealed two conspicuous conclusions, firstly the targets appeared to have the potential of being resolved to the size of one bin, and secondly there was significant blurring. It was suspected that this phenomenon is a direct consequence of the geometry of the bistatic SAR system employed in the simulation, coupled with the efforts to improve resolution and thus warranted further theoretical assessment.

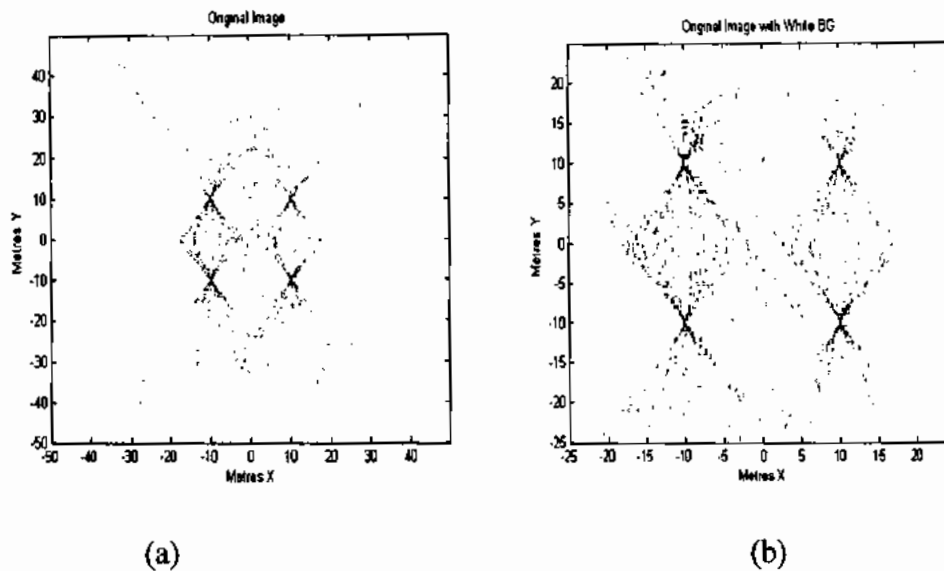


Figure 6.15 (a) Raw reconstructed image (b) Target area enlarged

It is pertinent to note that despite the targets exhibiting a star-like PSF, achieving a resolution comparable to the wavelength of GPS L1 frequency utilizing reflected GPS signals and without the help of a dedicated transmitter is a novel achievement. Resolution, among others, is an important factor while selecting a particular type of radar for different applications. Improved resolution will certainly pave the way for new and novel uses for this type of imaging. It is a very significant progress in the field of remote sensing utilizing transmitters of opportunity, especially the GPS.

6.6.2 Image restoration

The image-processing task at hand was to reconstruct the unfocused target signature into a focused image. Initially a technique of de-convolution of the signal with its PSF (point spread function) using Wiener filter and PSO (Particle swarm optimization) have been employed to

correct the blurred image obtained from four isolated point reflectors. Next for better image restoration results another hybrid technique based on the combination of PSO and SVD (Singular Value Decomposition) has been proposed.

The PSF is calculated during the course of simulation and used as the degradation function H . The deconvolution of a signal from another is performed by dividing the two signals in Fourier domain. The practical significance of deconvolution is that it can be used as an artificial or computational way to reverse the result of a convolution occurring in the physical domain, in pragmatic sense it is a process that removes the "blurring" obtained after convoluting data.

In order to perform deconvolution two images are required. Usually, one of the two images is a point spread function, or PSF, as shown in figure 6.16 (a), which represents the effect of distortion on a single point, the other image is the one from which this distortion is to be removed. The two images have to be of similar size and format to facilitate signal processing. If the point spread function is accurately known the deconvolution process will remove the blur or smear in the image.

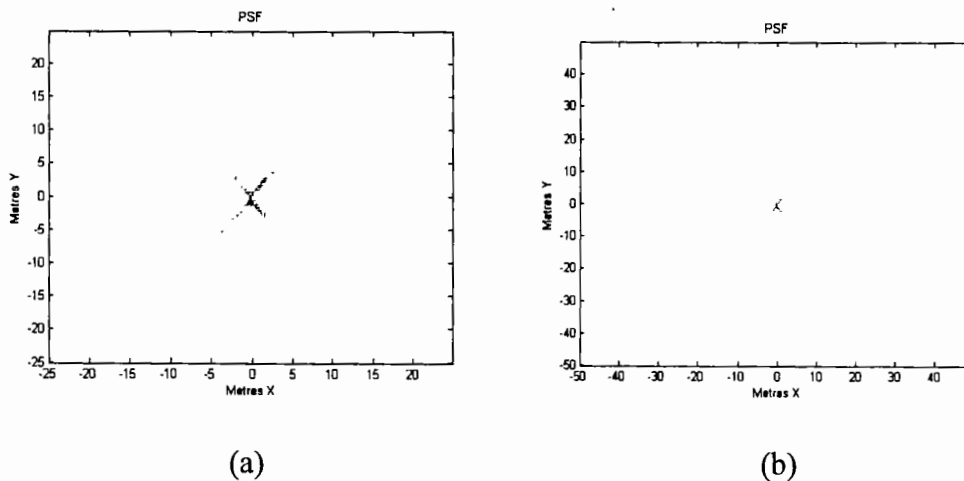


Figure 6.16 (a) Point spread function (PSF) (b) Image enlarged around centre

6.6.2.1 The Wiener filter

Because degradation is modeled as being the result of convolution, the restoration seeks to find filters that apply the process in reverse. Thus, the term image deconvolution is used frequently to signify linear image restoration and the filters are called deconvolution filters.

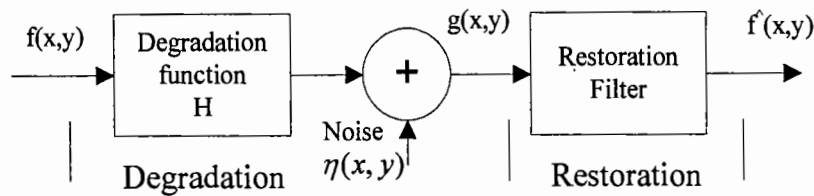


Figure 6. 17 The degradation process

The figure 6.17 depicts a basic degradation process, as evident the degradation function together with an additive noise term, operates on an input image, $f(x,y)$, to produce a degraded image $g(x,y)$.

Given $g(x,y)$, some knowledge about the degradation function H and some knowledge about the additive noise term $\eta(x,y)$, the objective of restoration is to obtain an estimate of the original image [81]. If H is a linear and position-invariant process, the degraded image in the spatial domain is given by: -

$$g(x, y) = h(x, y) * f(x, y) + \eta(x, y) \quad (6.11)$$

Where $h(x,y)$ is the spatial representation of the degradation function and symbol “*” indicates convolution, which in frequency domain is equivalent to multiplication, hence equation (6.11) in frequency domain representation can be written as:-

$$G(u, v) = H(u, v)F(u, v) + N(u, v) \quad (6.12)$$

The simplest approach to restoration is direct inverse filtering and is calculated as shown:-

$$\hat{F}(u, v) = \frac{G(u, v)}{H(u, v)} \quad (6.13)$$

Thus in elementary terms we divide the output with H, however, the situation is precarious as the output is now convolved and contains noise, blurring or both. Inverse filtering will result in the amplification of unwanted signals and suppression of required response.

Among the various methods available the Wiener filter is selected to remove the blurring of target on account of its unique characteristics. The Wiener filter is an adaptive filter. It tailors itself to be the best possible solution for a given dataset [82]. The Wiener Filtering executes an optimal trade-off between inverse filtering and noise smoothing. It removes the additive noise and inverts the blurring simultaneously. The method is founded on considering images and noise as random processes and the objective is to find an estimate \hat{f} of the uncorrupted image f such that the mean square error between them is minimized. This error measure is given by:

$$e^2 = E((f - \hat{f})^2) \quad (6.14)$$

Where $E(.)$ is the expected value of the argument. Assuming that noise and the image are uncorrelated, the minimum of error function in equation (6.11), after simplification, in frequency domain is given by: -

$$\hat{F}(u, v) = G(u, v) \left[\frac{H^*(u, v)}{|H(u, v)|^2 + \frac{S_\eta(u, v)}{S_f(u, v)}} \right] \quad (6.15)$$

This result is known as the Wiener filter, also termed as minimum mean square filter or least square filter. As evident from equation (6.15) the Wiener Filter does not have the same problem as the inverse filter with zeros in the degradation function [81].

Whereas, in equation (6.15), $H^*(u, v)$ is the complex conjugate of $H(u, v)$, $S_\eta(u, v)$ is the power spectrum of noise and $S_f(u, v)$ is the power spectrum of un-degraded image and the term $|H(u, v)|^2$ is equivalent to $H^*(u, v) H(u, v)$.

During the simulation white noise is assumed, whose power spectrum is constant, which simplifies things considerably. The Wiener filter in Matlab[®] is based on the following equation with value of K selected as 10^{16} .

$$\hat{F}(u, v) = G(u, v) \left[\frac{H^*(u, v)}{|H(u, v)|^2 + K} \right] \quad (6.16)$$

The restored image in the spatial domain is given by the inverse Fourier transform of the frequency domain estimate. The reconstructed and deconvolved images are shown in figure 6.19 (a) and (b), respectively.

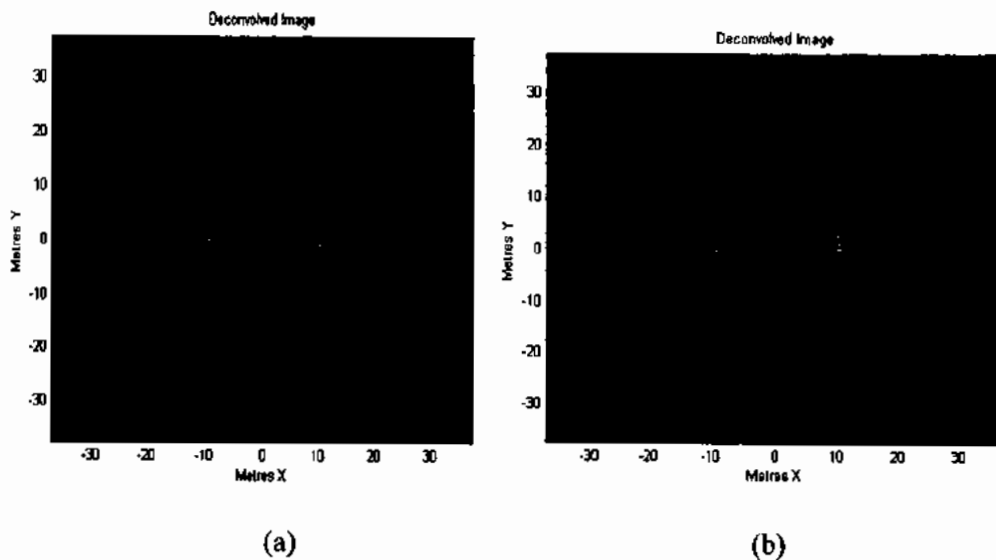


Figure 6. 18 Comparison of results for T_s of (a) 4500 s (b) 2400 s

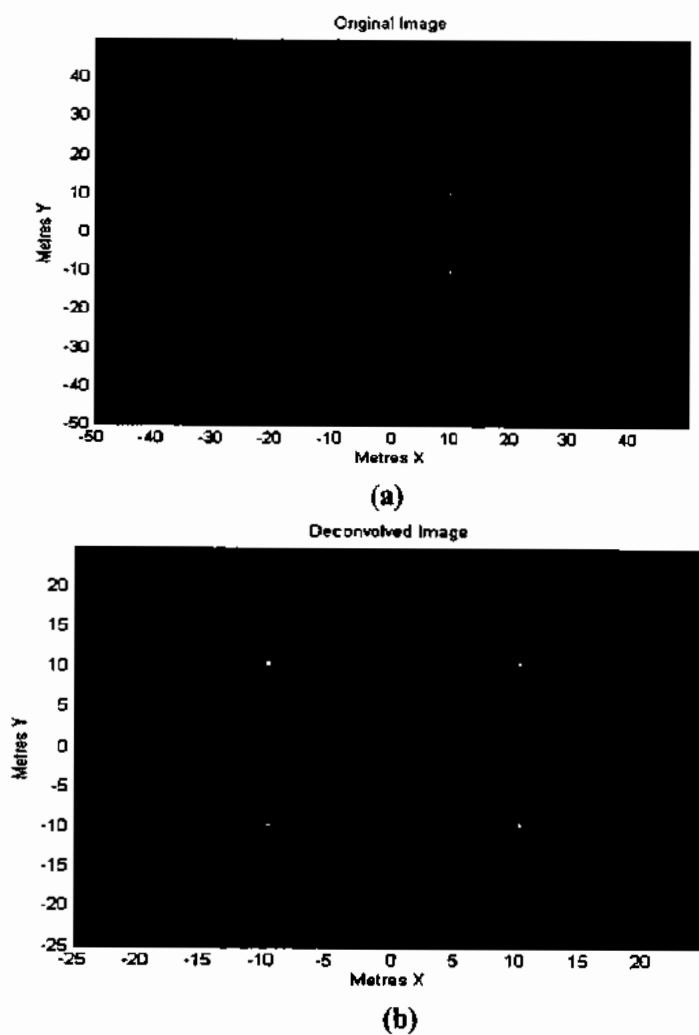


Figure 6. 19 (a) Reconstructed image (b) De-convolved Image

It can be deduced from the analysis of de-convolved images, obtained for various integration times and compared in figure 6.18 that the de-convolution processes involving a Fourier transform, furnishes improved resolution even at reduced integration time.

The images exhibit a range resolution comparable to the wavelength of GPS L1 frequency (0.2 meters). The azimuth resolution can be improved by acquiring data from two separate GPS satellites having different orbiting geometries and overlapping the results. It has been suggested in [56] that the method of non-coherently combining the output from all available satellites can be implemented to improve the results. However, it is just a suggestion and can be undertaken as part of a future research.

6.6.2.2 De-convolution using PSO (Particle swarm optimization)

Deconvolution of images using PSO has recently attracted attention. In current research endeavor PSO has been applied with multiple degraded observations of true image obtained at different time instances. These multiple observations of correlated images provide diversity and facilitate achieving improved results embedded in the degraded observations using PSO based deconvolution method.

Detail about PSO is given in [83]. In PSO method first of all a group of random 'particles' or solutions are initialized which are then updated in each iteration in order to find out the optimum amongst them. After every iteration, two optimum or best values are obtained from the generated particles. The first best value is called local best where its neighborhood is small. The second best value tracked by PS optimizer is the value best among all of the particles in the whole population and is known as global best where the neighborhood of the particle is the entire swarm. Its fitness value is also stored.

In our case steps involved during its implementation are depicted in Figure 6.20. As shown in figure 6.20 in first step all the necessary components/particles including the local and global variables of PSO method are initialized. The most important part of the technique that is cost function is calculated in the next phase. For getting optimal solution the cost function is minimized to permissible extent.

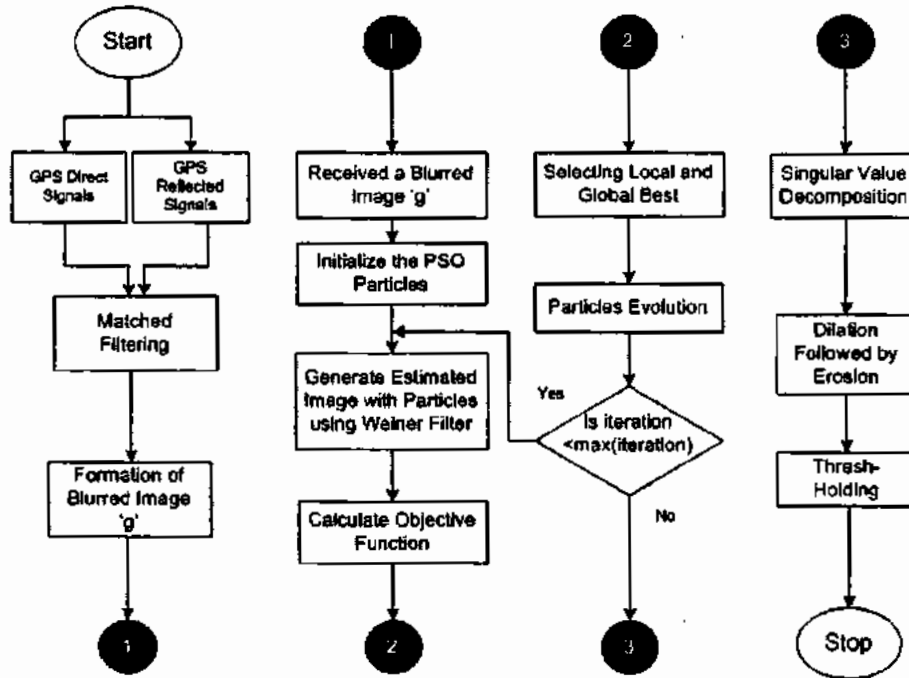


Figure 6. 20 PSO and SVD System Model Flowchart

After defining the cost function, in next phase population initialization is done. Each particle tries to reach the solution by minimizing the cost function. Since the image is in a matrix form or in $n \times n$ format, in order to apply PSO; it is converted to a vector form of $1 \times n$ to create the same length of particles vectors. Other parameters such as initial velocity vector, population size, learning factors values and the value of the maximum amount of the iterations are also initialized.

After focusing the targets using PSO method in the deconvolved image, for further noise reduction the technique of Singular Value Decomposition (SVD) was utilized. The simulation result is given in Figure 6.21.

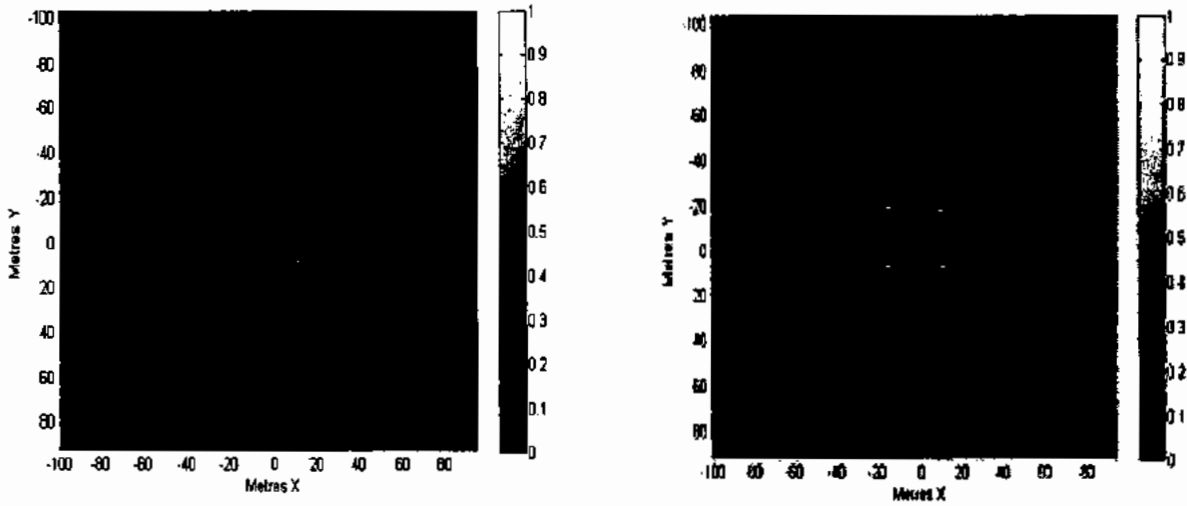


Figure 6. 21 (a) De-convolved Image after PSO (b) Restored image after SVD

The performance of both restoration techniques have been further compared by evaluating figures of merit such as Mean Square Error, Peak SNR, Improved SNR as given in table 6.3. A higher ISNR and lower MSE would normally indicate that the image reconstruction has improved.

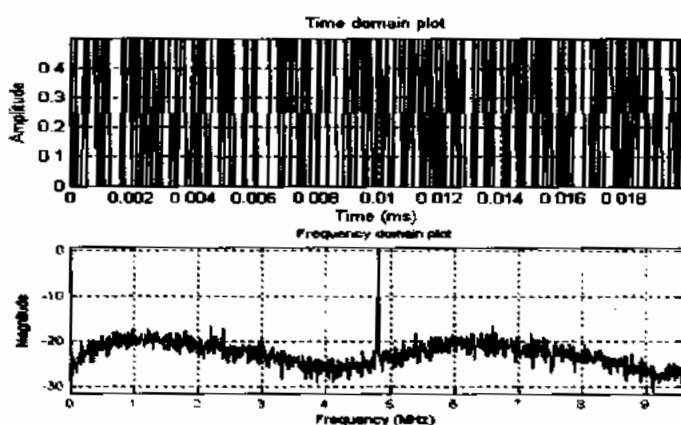
Table 6. 3 Performance evaluation of Restoration techniques

Method	MSE	ISNR(dB)	PSNR(dB)
Wiener Filter	6.9145e-005	0.2090	95.7930
P.S.O	3.9291e-006	4.8716	124.4710

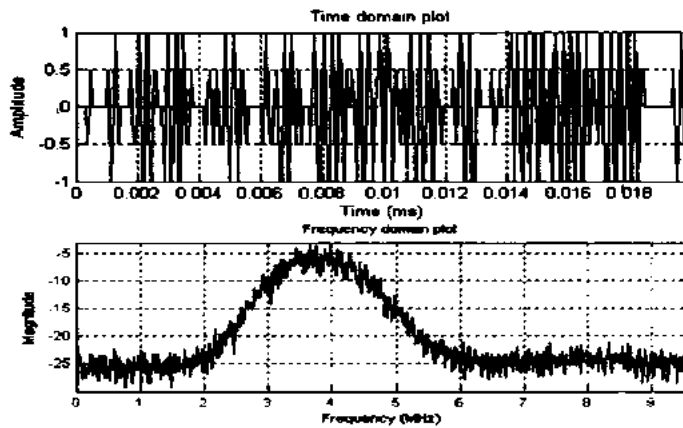
6.7 Analysis of GPS Data

The analysis of initial GPS data started with the generation of two types of plots as shown in the figure 6.22. The first sub-plot in the figure 6.22 (a) depicts the time domain plot for 1000 samples. As expected no discernable structure is visible despite the 4.78 MHz IF for the collected data, which is in line with the text explained earlier that GPS data set is a traditional CDMA signal, submersed in white noise and only with the help of correlation theory the data can be demodulated.

However, the frequency spectrum plot is unexpected and does not seem to exhibit an ideal response. Comparison was performed with the simulated data generated with the help of C++ software. The second sub-plot, as shown in figure 6.22 (b), revealed an obvious bulge centered around the IF. This is the 2.046 MHz bandwidth of the C/A code. We know that due to the CDMA nature of the GPS system, all the satellite signal power is overlaid at the resultant IF. Thus the spectrum shows the summation of signal power for all visible satellites.



(a)



(b)

Figure 6.22 Comparison of time and frequency domain plots (a) Actual GPS data (b) Simulated GPS data

It was observed that despite the distorted frequency response it is still possible to acquire the direct and reflected GPS signals and generate an image. This might be possible due to the robust and deterministic nature of the GPS signals. The GPS system is based on CDMA techniques and for signal detection a correlation peak of the direct and reflected signal is sufficient.

6.7.1 Acquisition and Tracking algorithms

In order to verify that the acquisition program works properly, the simulated data was first used as the input signal. Figure 6.23 (a), shown below, illustrates the result of the acquisition process for a simulated GPS signal (PRN 31) and an acquisition time of only one ms. The correlation peak can be observed where the estimated coarse carrier frequency and beginning of the C/A code is present for the particular PRN, as calculated by the acquisition program.

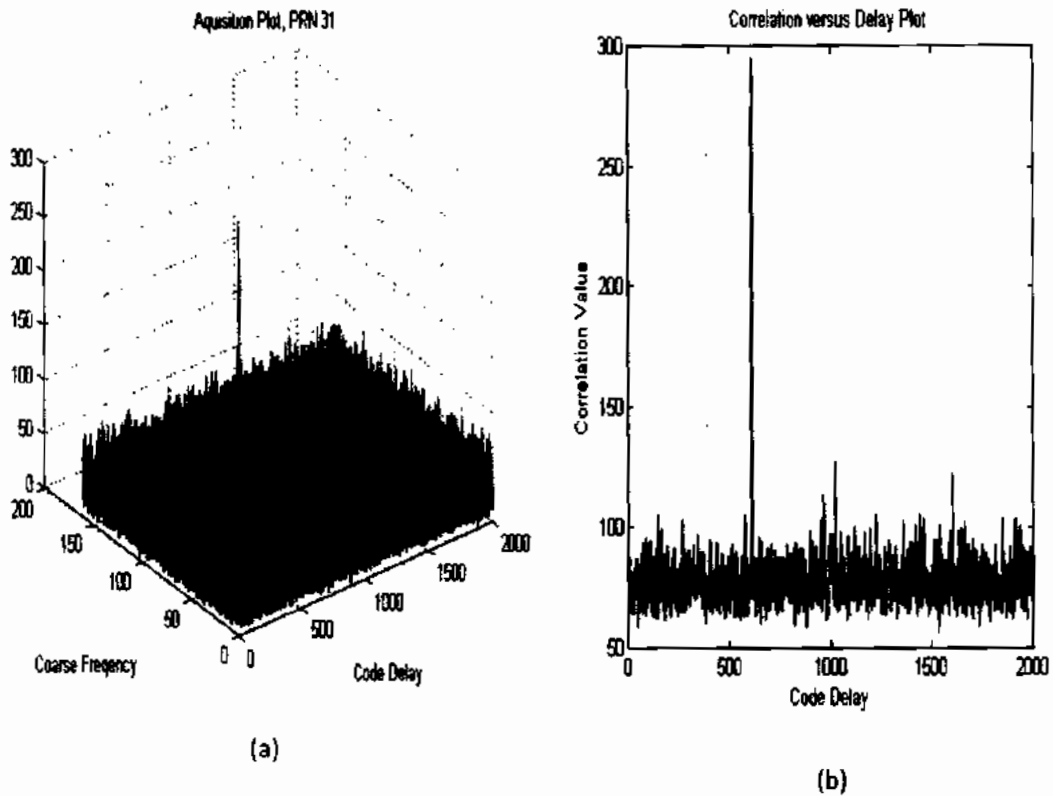


Figure 6. 23 (a) Acquisition plot for PRN 31 for one ms (b) Correlation versus delay plot for PRN 31 (one ms of simulated GPS data)

The actual GPS data was captured with a commercial active antenna having a specified gain of 35dB. An acquisition diagram for the data collected with the help of dual frequency GPS front end is shown in figure 6.24. The part (a) of the diagram shows the plot for 2 ms of coherent acquisition time. The results can be further improved by increasing the coherent acquisition time. Figure 6.24 (b) shows and compares the acquisition diagram for 20 ms of data, as evident from the figure the uncorrelated noise has been cancelled out and an ideal peak is observable.

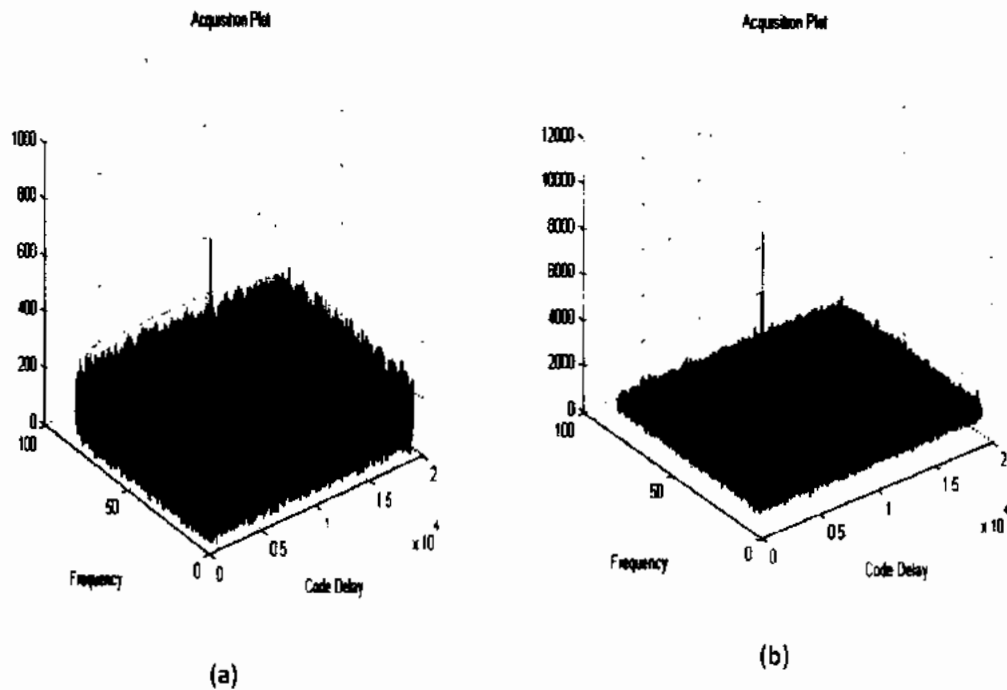


Figure 6. 24 Acquisition plots for PRN 2 with time (a) 2 ms (b) 20 ms

The position calculations were made from 37 seconds of data. This length made it possible to decode a complete frame of navigation data including all ephemerides for the visible satellites. During acquisition of data for position calculation purposes four satellites were visible. Position calculations were performed with the help of software GNSS receiver code with some modifications [11]. The acquisition diagram for the captured GPS data is shown in figure 6.25, depicting the satellites having strength greater than the acquisition threshold set at 2.5.

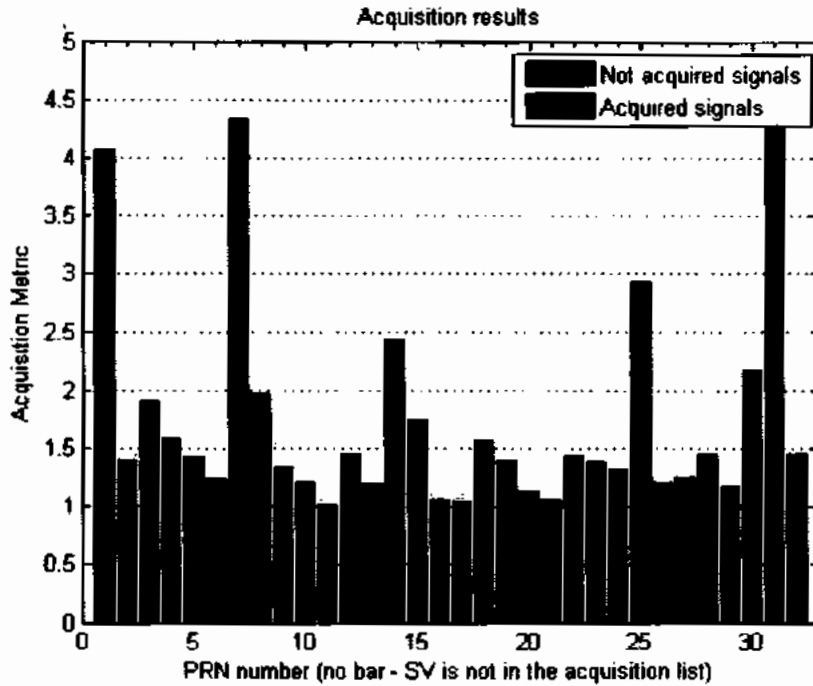


Figure 6. 25 Acquisition diagram for actual GPS data

Main purpose of the tracking process is to refine the coarse values of carrier IF frequency calculated by the acquisition algorithms and keep track and lock of the code phase as the signal properties change over time, thus the tracking algorithm runs continuously to follow the changes in frequency as a function of time.

The sky plot in figure 6.26, shows that satellites with PRN (1,7,15,25,31) were visible during the real data collection. Good observations are achieved when measurements involve at least five satellites which are evenly spaced [84].

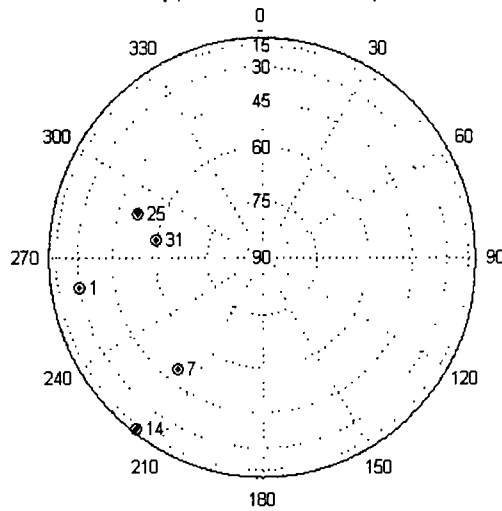
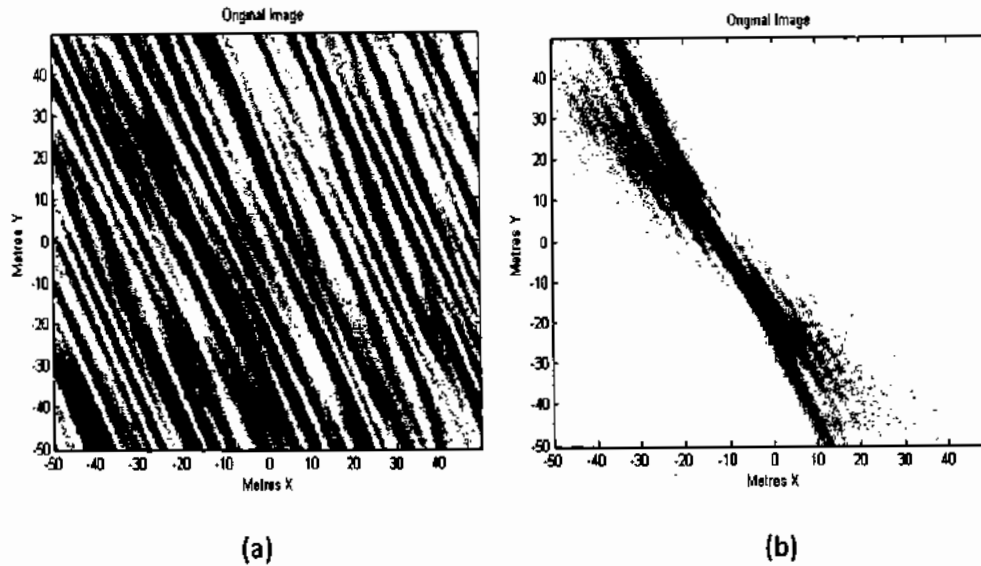


Figure 6. 26 Satellite polar plot, showing the visible satellites

6.8 Results for Actual GPS Data

A comparison has been made in figure 6.27 between the images obtained by processing 2400 seconds of actual and simulated data. The target can be seen in the middle of the diagram, as the antenna's main lobe was aimed roughly towards the target center. Unfortunately, an increase in the integration time also resulted in more signal being received by the highly directional antenna and some of the signal was not received from the target, but bounced off from nearby objects and building front. In radar terms, it is called ground clutter and the presence of excessive lines and noise can be partially attributed due to this phenomena.

Moreover, the resolution of the target is not impressive on account of the limited signal duration. It is expected that the availability of longer duration GPS signals (about two hours) will improve the target resolution by providing enhanced change in geometry for the orbiting GPS satellite and creating a larger synthetic aperture.



**Figure 6. 27 Comparison of image obtained by reconstructing 2400 sec of (a) Actual signal
(b) Simulated signal**

As evident from the results, although it is roughly possible to distinguish the target, there is excessive backscatter or clutter and noise exhibited in the images. Following reasons may contribute towards this factor.

- 1) The situation was exacerbated due to the fact that the high gain LHCP antenna was placed in front of a large brick building. The antenna was designed to acquire the weak reflected GPS signal, but returns from objects around the target were also received and displayed in the image.
- 2) As mentioned earlier that due to hardware limitations, the data files were acquired after an interval of every 30 seconds each, such low frequency for acquiring temporal samples induced an aliasing effect. In future it is recommended to modify the imaging hardware to acquire a small burst of GPS data after every three seconds.
- 3) The coordinates of the target and the antenna were calculated by a commercial GPS receiver and later converted from geographical (ϕ, λ, h) to Cartesian ECEF (X, Y, Z) coordinate with the help of code developed in Matlab[®]. These errors due to spatial referencing may have induced

further target and receiver position noise. In future it is recommended to perform receiver position calculation with the help of a high accuracy GPS receiver.

The images exhibited in this section may seem very primitive, but it has to be kept in mind that no dedicated radar transmitter was available during the experiments. The target has been detected in a hostile environment with the help of extremely weak reflected GPS signals that are omnipresent, but exhibit an appalling SNR.

It is further apprized that the change in geometry to process the data with the help of SAR technique was provided by the orbiting GPS satellite. This particular method has so far not been utilized in a practical environment for imaging purposes.

Chapter 7

Conclusion and Future Work

7.1 Conclusion

The ultimate objective of the PhD dissertation was to confirm the idea of utilizing the reflected GPS signals for target detection based on SAR principle. Feasibility of the concept has been confirmed by the Matlab[®] simulations and the obtained results have been encouraging. In order to demonstrate a practical system and carry out testing in real time environment, attempts were made and working “proof of concept” prototype of the system has been assembled and demonstrated.

As mentioned in the second chapter, there can be three different types of imaging scenarios based on the position of GPS receiver and the source that generates the requisite change in geometry. The imaging hardware can be kept airborne, placed on a ground vehicle or simply remain stationary. During the course of current research endeavour all three imaging arrangements have been studied and simulated in a detailed manner. After thorough deliberation and based on the results and practical constraints, it was finally decided to perform the experiment for data acquisition with the hardware positioned at a fixed geographical location.

The suitability of L1 and L5 GPS signals for BSAR applications have been investigated in detail. The performance evaluation parameters considered during the analysis are: autocorrelation, power budget analysis, and power Level. From the obtained simulation results it can be deduced that L5 has superior detection characteristics as compared to L1 due to greater bandwidth, high

correlation peaks and better SNR. Hence better results can be achieved with L5 GPS signal as compared to L1 signal.

7.2 Future Work

The basic objectives set forth in the initial research proposal are almost achieved. However, in order to exploit the imaging system for potential applications and explore some additional feature, there is still lot of effort to be performed. The work required to further improve the imaging hardware and enhance quality of the image has been summarized below.

1. For a high resolution image more data is to be acquired at a suitable location that ensures visibility of the reference GPS satellite for at least two to three hours.
2. Some method/decluttering algorithm needs to be devised in the image processing algorithm that ensures removal of ground and other clutter. The excessive lines in the reconstructed image may be partly generated due to ground clutter.
3. Efforts are to be made to increase the total number of segments, thus increasing the frequency at which samples are acquired for processing in the reconstruction engine.
4. As mentioned in section (6.7) of this report the output of dual front GPS receiver and data acquisition device exhibits a poor frequency response. Despite this handicap the results are encouraging, most probably due to the robust and deterministic nature of the GPS signal. The issue needs to be further investigated in order to rectify the imaging hardware. It is expected that in the next generation and modified imaging hardware the results would be further improved. The reconstruction engine only requires a correlation peak from the target and if the reflected signal is present this peak can be detected.

5. More efficient correlation algorithms as mentioned in [80] based on the range migration algorithm to process SAR data in Fourier domain can be consulted in this regard. This should improve the computational efficiency of the simulation.
6. During the course of current research endeavours, the entire GPS signal generation and image reconstruction process has been simulated. The smeared image obtained due to poor quality PSF was improved by means of a Wiener filter and PSO based deconvolution method. It will be interesting to explore other deconvolution techniques like blind de-convolution and nature inspired Algorithms like Differential Evolution, Fire Fly etc.

References

- [1] E. Kaplan and C. Hegarty, *Understanding GPS: principles and applications*. Artech house, 2005.
- [2] A. Carlström, “Information content in reflected global navigation satellite system signals,” in *Proc. 2nd International Conference on Wireless Communication, Vehicular Technology, Information Theory and Aerospace & Electronic Systems Technology (Wireless VITAE)*, 2011, pp. 1–5.
- [3] M. Jianguo, C. Kejing, X. Jiangning, and Z. Yinbing, “GPS reflected signal analysis based on software receiver,” in *Proc. 2nd International Conference on Signal Processing Systems (ICSPS)*, 2010, vol. 2, pp. 172-176.
- [4] M. Usman and D. W. Armitage, “A remote imaging system based on reflected GPS signals,” in *Proc. International Conference on Advances in Space Technologies*, 2006, pp. 173–178.
- [5] Z. Zhaoming, F. Yang, X. Zhengang, and C. Hongguang, “Remote sensing of sea surface wind of Hurricane Michael by GPS reflected signals,” *Geo-spatial Inf. Sci.*, vol. 9, no. 1, pp. 24–31, 2006.
- [6] M. Soumekh, *Synthetic aperture radar signal processing*, vol. 7. New York: Wiley, 1999.
- [7] J. A. Richards, *Remote sensing with imaging radar*, vol. 1. Springer, 2009.
- [8] P. Z. Peebles, *Radar principles*. John Wiley & Sons, 2007.
- [9] B. Sklar, *Digital communications*, vol. 2. Prentice Hall NJ, 2001.
- [10] S. Y. Zheng, “Signal acquisition and tracking for a software GPS receiver.” M.S thesis, Virginia Polytechnic Institute and State University, USA, 2005.

- [11] K. Borre, D. M. Akos, N. Bertelsen, P. Rinder, and S. H. Jensen, *A software-defined GPS and Galileo receiver: a single-frequency approach*. Springer Science & Business Media, 2007.
- [12] T. Saleem and M. Usman, "Analysis and Mitigation of Tropospheric Error Effect on GPS Positioning Using Real GPS Data," *Int. J. Electron. Electr. Eng.*, vol. 2, no. 3, pp. 249–253, 2014.
- [13] L. Baroni and H. K. Kuga, "Analysis of navigational algorithms for a real time differential GPS system," in *Proc. 18th International Congress of Mechanical Engineering*, Sao Paulo: ABCM, 2005, pp. 45-53.
- [14] D. Wells, N. Beck, A. Kleusberg, E. J. Krakiwsky, G. Lachapelle, R. B. Langley, K. Schwarz, J. M. Tranquilla, P. Vanicek, and D. Delikaraoglou, "Guide to GPS positioning," in *Proc Canadian GPS Assoc*, 1987, pp. 113-121.
- [15] J. Malmström, "Robust navigation with GPS/INS and adaptive beamforming." Swedish Defence Research Agency System Technology Division Report, Stockholm, Sweden, April, 2003.
- [16] A. Leick, *GPS Satellite Surveying*, John Willey & Sons, Inc., New York, 1995.
- [17] J. A. Klobuchar, "Ionospheric time-delay algorithm for single-frequency GPS users," *IEEE Trans. Aerosp. Electron. Syst.*, no. 3, pp. 325–331, 1987.
- [18] A. Brown, E. Holm, and K. Groves, "GPS Ionospheric Scintillation Measurements using a Beam Steering Antenna Array for Improved Signal/Noise," DTIC Document, 2006.
- [19] C. Satirapod and P. Chalermwattanachai, "Impact of different tropospheric models on GPS baseline accuracy: case study in Thailand," *Int. J. Global Positioning*, vol. 1, no. 9, pp. 30-41, 2005.
- [20] H. S. Hopfield, "Tropospheric effect on electromagnetically measured range: Prediction from surface weather data," *J. Radio Sci.*, vol. 6, no. 3, pp. 357–367, 1971.

- [21] T. Saleem, M. Usman, A. Elahi and N. Gul, "Simulation and Performance Evaluations of the New GPS L5 and L1 Signals," *Journal of Wireless communication and Mobile computing*, Hindawi Publishing Corporation vol. 2017, pp. 1-4, 2017.
- [22] K. Krumvieda, C. Cloman, E. Olson, J. Thomas, W. Kober, P. Madhani and P. Axelrad, "A complete IF software GPS receiver- A tutorial about the details," in *Proc. 14th International Technical Meeting of the Satellite Division of the Institute of Navigation (ION GPS 2001)*, Salt Lake City, UT, 2001, pp. 789–829.
- [23] A. Komjathy, J. A. Maslanik, V. U. Zavorotny, P. Axelrad, and S. J. Katzberg, "Towards GPS surface reflection remote sensing of sea ice conditions," In *Proc. International Conference on Remote Sensing for Marine and Coastal Environments*, Charleston, South Carolina, 1-3 May 2000, vol 2, pp. 447–456.
- [24] J. L. Garrison, A. Komjathy, V. U. Zavorotny, and S. J. Katzberg, "Wind speed measurement using forward scattered GPS signals," *IEEE Trans., Geosci. Remote Sensing*, vol. 40, no. 1, pp. 50–65, 2002.
- [25] V. Behar and C. Kabakchiev, "Detectability of air targets using bistatic radar based on GPS L5 signals," in *Proc. International Radar Symposium (IRS)*, 2011, pp. 212–217.
- [26] B. Mojarrabi, J. Homer, K. Kubik, and I. D. Longstaff, "Power budget study for passive target detection and imaging using secondary applications of GPS signals in bistatic radar systems," in *Proc IEEE International Symposium Geoscience and Remote Sensing*, 2002, vol. 1, pp. 449–451.
- [27] M. Cherniakov, D. Nezlin, and K. Kubik, "Air target detection via bistatic radar based on LEOS communication signals," in *Proc. IEEE Conf. on Radar, Sonar Navig.*, vol. 149, no. 1, pp. 33–38, 2002.
- [28] M. Martin-Neira, "A passive reflectometry and interferometry system (PARIS): Application to ocean altimetry," *J.ESA.*, vol. 17, pp. 331–355, 1993.
- [29] C. Zuffada and V. Zavorotny, "Coherence time and statistical properties of the GPS signal

- scattered off the ocean surface and their impact on the accuracy of remote sensing of sea surface topography and winds,” in *Proc. IEEE International Symposium Geoscience and Remote Sensing*, 2001, vol. 7, pp. 3332–3334.
- [30] J. L. Garrison, S. J. Katzberg, and M. I. Hill, “Effect of sea roughness on bistatically scattered range coded signals from the Global Positioning System,” *Geophys. Res. Lett.*, vol. 25, no. 13, pp. 2257–2260, 1998.
- [31] J. L. Garrison, “Simulation of wind speed retrievals from an orbiting bistatic GPS receiver,” in *Proc. IEEE International Symposium Geoscience and Remote Sensing*, 2001, vol. 3, pp. 1515–1517.
- [32] W. Xin, S. Qiang, Z. XunXie, L. DaRen, S. LianJun, H. Xiong, R. Giulio, D. Stephen, and F. Soulat, “First China ocean reflection experiment using coastal GNSS-R,” *Chinese Sci. Bull.*, vol. 53, no. 7, pp. 1117–1120, 2008.
- [33] X. Wang, Q. Sun, X. Zhang, D. Lu, and X. Hu, “Applications of GPS-R Technique for Ocean Remote Sensing: Results of Coastal Experiment in China,” in *Proc. International Conference on Multimedia Technology (ICMT)*, 2010, pp. 1–4.
- [34] S. Tay, F. Maussang, A. Coatanhay, T. Chonavel, and R. Garello, “Near sea surface target tracking by extended kalman filtering of the GPS reflected signals,” in *Proc. IEEE International Conference on OCEANS*, 2011, pp. 1–4.
- [35] S. T. Gleason, “INNOVATION-Reflecting on GPS-Sensing Land and Ice from Low Earth Orbit-An out-of-the-ordinary application of GPS uses signals reflected off the Earth’s surface to sense land and ice, as well as,” *J. GPS World*, vol. 18, no. 10, pp. 44–49, 2007.
- [36] W. J. Emery, P. Axelrad, R. S. Nerem, D. Masters, M. Armatys, and A. Komjathy, “Student reflected GPS experiment (SuRGE),” in *Proc. IEEE International Symposium on Geoscience and Remote Sensing*, 2001, vol. 3, pp. 1518–1520.
- [37] D. Entekhabi, E. G. Njoku, P. E. Neill, K. H. Kellogg, W. T. Crow, W. N. Edelstein, J. K. Entin, S. D. Goodman, T. J. Jackson, and J. Johnson, “The soil moisture active passive

(SMAP) mission,” In *Proc. IEEE International Symposium on Remote Sensing*, 2010, vol. 98, no. 5, pp. 704–716.

- [38] Y. H. Kerr, P. Waldteufel, J.-P. Wigneron, J. Martinuzzi, J. Font, and M. Berger, “Soil moisture retrieval from space: The Soil Moisture and Ocean Salinity (SMOS) mission,” *IEEE Trans. Geosci. Remote Sens.*, vol. 39, no. 8, pp. 1729–1735, 2001.
- [39] Y. Jia, P. Savi, Y. Pei, and R. Notarpietro, “GNSS reflectometry for remote sensing of soil moisture,” in *Proc. IEEE 1st International Forum on Research and Technologies for Society and Industry Leveraging a better tomorrow (RTSI)*, 2015, pp. 498–501.
- [40] Y. Jia and P. Savi, “Polarimetric GNSS-R measurements for soil moisture and vegetation sensing,” in *Proc. IEEE International on Geoscience and Remote Sensing Symposium (IGARSS)*, 2016, pp. 5260–5263.
- [41] N. R. Alvarez, A. Monerris, X. B. Lluís, A. Camps, M. V. Llosera, J. F. Marchan-Hernández, I. R. Perez, E. Valencia, J. M. Fernández, and N. S. Martin, “Soil moisture and vegetation height retrieval using GNSS-R techniques,” in *Proc. IEEE International Symposium on Geoscience and Remote Sensing*, 2009, vol. 3, pp. 860-869.
- [42] N. R. Alvarez, A. Camps, M. V. Llosera, X. B. Lluís, A. Monerris, I. R. Perez, E. Valencia, J. F. M. Hernandez, J. M. Fernandez, and G. B. Turrichia, “Land geophysical parameters retrieval using the interference pattern GNSS-R technique,” *IEEE Trans. Geosci. Remote Sens.*, vol. 49, no. 1, pp. 71–84, 2011.
- [43] P. Ferrazzoli, L. Guerriero, N. Pierdicca, and R. Rahmoune, “Forest biomass monitoring with GNSS-R: theoretical simulations,” *J. Adv. Sp. Res.*, vol. 47, no. 10, pp. 1823–1832, 2011.
- [44] S. Fujita, P. Holmlund, I. Andersson, I. Brown, H. Enomoto, Y. Fujii, K. Fujita, K. Fukui, T. Furukawa, and M. Hansson, “Spatial and temporal variability of snow accumulation rate on the East Antarctic ice divide between Dome Fuji and EPICA DML,” *Int. J. Cryosph.*, vol. 5, no. 4, pp. 1057–1081, 2011.

- [45] E. Cardellach, F. Fabra, A. Rius, S. Pettinato, and S. D'Addio, "Characterization of dry-snow sub-structure using GNSS reflected signals," *J. Remote Sens. Environ.*, vol. 124, pp. 122–134, 2012.
- [46] F. Fabra, "GNSS-R as a source of opportunity for sea ice and dry snow remote sensing." Ph. D. Dissertation, Polytechnical University of Catalonia (UPC), Barcelona, 2013.
- [47] S. Jin, J. Park, J. Cho, and P. Park, "Seasonal variability of GPS derived zenith tropospheric delay (1994–2006) and climate implications," *J. Geophys. Res. Atmos.*, vol. 112, no. 9, pp. 191–201, 2007.
- [48] S. Jin and O. F. Luo, "Variability and climatology of PWV from global 13-year GPS observations," *IEEE Trans. Geosci. Remote Sens.*, vol. 47, no. 7, pp. 1918–1924, 2009.
- [49] T. Schmidt, J. Wickert, and A. Haser, "Variability of the upper troposphere and lower stratosphere observed with GPS radio occultation bending angles and temperatures," *J. Adv. Sp. Res.*, vol. 46, no. 2, pp. 150–161, 2010.
- [50] C. O. Ao, "Atmospheric sensing using GNSS radio occultations," *J. GNSS Appl. Methods*, Springer, vol. 978, pp. 1–5, 2009.
- [51] S. Jin, J. U. Park, J. L. Wang, B. K. Choi, and P. H. Park, "Electron density profiles derived from ground-based GPS observations," *J. Navig.*, vol. 59, no. 3, pp. 395–401, 2006.
- [52] S. Jin, O. F. Luo, and P. Park, "GPS observations of the ionospheric F2-layer behavior during the 20th November 2003 geomagnetic storm over South Korea," *J. Geod.*, vol. 82, no. 12, pp. 883–892, 2008.
- [53] I. A. Nesterov and V. E. Kunitsyn, "GNSS radio tomography of the ionosphere: The problem with essentially incomplete data," *J. Adv. Sp. Res.*, vol. 47, no. 10, pp. 1789–1803, 2011.
- [54] S. Jin, G. P. Feng, and S. Gleason, "Remote sensing using GNSS signals: Current status and future directions," *J. Adv. Sp. Res.*, vol. 47, no. 10, pp. 1645–1653, 2011.

- [55] Y. Li, C. Rizos, E. Donskoi, J. Homer, and B. Mojarrabi, "3D multi-static SAR system for terrain imaging based on indirect GPS signals," *J. Global Positioning System*, vol. 1, no. 3, pp. 10-15, 2002.
- [56] E. P. Glennon, A. G. Dempster, and C. Rizos, "Feasibility of air target detection using GPS as a bistatic radar," *J. Global Positioning System*, vol. 1, no. 10, pp. 50-60, 2006.
- [57] V. Behar, C. Kabakchiev, and H. Rohling, "Air target detection using navigation receivers based on GPS L5 signals," in *Proc. of ION GNSS*, 2011, pp. 333–337.
- [58] T. Zeng, M. Cherniakov, and T. Long, "Generalized approach to resolution analysis in BSAR," *IEEE Trans. Aerosp. Electron. Syst.*, vol. 41, no. 2, pp. 461–474, 2005.
- [59] M. Cherniakov, T. Zeng, and E. Plakidis, "Analysis of space-surface interferometric bistatic radar," in *Proc. IEEE International Symposium on Geoscience and Remote Sensing*, 2003, vol. 2, pp. 778–780.
- [60] M. Cherniakov, R. Saini, R. Zuo, and M. Antoniou, "Study of BSAR with non-cooperative transmitter," in *Proc. EMRS DTC*, 2005, vol. 1, pp. 7-15.
- [61] M. Cherniakov, R. Saini, R. Zuo, and M. Antoniou, "Space surface bistatic SAR with space-borne non-cooperative transmitters," in *Proc. European Radar Conference*, 2005, pp. 9–12.
- [62] O. Nogués, A. Sumpsi, A. Camps, and A. Rius, "A 3 GPS-channels Doppler-delay receiver for remote sensing applications," in *Proc. IEEE International Symposium on Geoscience and Remote Sensing*, 2003, vol. 7, pp. 4483–4485.
- [63] S. T. Lowe, P. Kroger, G. Franklin, J. L. LaBrecque, J. Lerma, M. Lough, M. R. Marcin, R. J. Muellerschoen, D. Spitzmesser, and L. E. Young, "A delay/doppler-mapping receiver system for GPS-reflection remote sensing," *IEEE Transaction on Geoscience and Remote Sensing*, vol. 40, no. 5, pp. 1150–1163, 2002.
- [64] L. Dong, *IF GPS signal simulator development and verification*. National Library of Canada, 2005.

- [65] D. Manandhar, R. Shibasaki, and H. Torioto, "Prototype software-based receiver for remote sensing using reflected GPS signals," in *Proc. ION GNSS*, 2005, pp. 226-233.
- [66] D. Manandhar, R. Shibasaki, and P.-L. Normark, "GPS signal analysis using LHCP/RHCP antenna and software GPS receiver," in *Proc. 17th International Technical Meeting of the Satellite Division of The Institute of Navigation (ION GNSS 2004)*, 2001, pp. 2489–2498.
- [67] M. Antoniou, R. Saini, and M. Cherniakov, "Results of a space-surface bistatic SAR image formation algorithm," *IEEE Trans. Geosci. Remote Sens.*, vol. 45, no. 11, pp. 3359–3371, 2007.
- [68] R. Saini, M. Cherniakov, and V. Lenive, "Direct path interference suppression in bistatic system: DTV based radar," in *Proc. International Radar Conference*, 2003, pp. 309–314.
- [69] D. K. P. Tan, H. Sun, Y. Lu, M. Lesturgie, and H. L. Chan, "Passive radar using global system for mobile communication signal: theory, implementation and measurements," in *Proc. IEEE Radar, Sonar Navig.*, 2005 vol. 152, no. 3, pp. 116–123.
- [70] P. E. Howland, D. Maksimiuk, and G. Reitsma, "FM radio based bistatic radar," *IEE Proceedings-Radar, Sonar Navig.*, vol. 152, no. 3, pp. 107–115, 2005.
- [71] M. Usman, T. Saleem, and D. W. Armitage, "Design, Assembly and Testing of a High Gain Lhcp Helical Antenna for Reception of Reflected GPS Signals," *J. Prog. Electromagn. Res. C*, vol. 44, pp. 161–174, 2013.
- [72] J. D. Kraus, "The helical antenna," in *Proc. IRE*, 1949, vol. 37, no. 3, pp. 263–272.
- [73] J. D. Kraus, *Antenna theory*. McGraw Hill International Edition, (ISBN 0-07035422-7), New York, 1988.
- [74] A. R. Djordjević, A. G. Zajić, M. M. Ilić, and G. L. Stüber, "Optimization of helical antennas," *IEEE Antennas Propag. Mag.*, vol. 48, no. 6, pp. 107–115, 2006.
- [75] H. King and J. Wong, "Characteristics of 1 to 8 wavelength uniform helical antennas,"

IEEE Trans. Antennas Propag., vol. 28, no. 2, pp. 291–296, 1980.

- [76] D. T. Emerson, “The gain of the axial-mode helix antenna,” *J. Antenna Compend.*, vol. 4, pp. 64–68, 1995.
- [77] M. Bavaro, “SdrNav20 Manual.” Available: <http://www.onetalent-s.com/ideas/software-defined-radio/sdrnav20>.
- [78] J. R. Clynch, *Earth Coordinates*, McGraw Hill International Edition, Feb., 2006.
- [79] J. Ackeret, F. Esch, C. Gard, F. Gloeckler, D. Oimen, J. Perez, J. Simpson, D. Specht, H. Rossander, and D. Stoner, *Handbook for Transformation of Datums, Projections, Grids, and Common Coordinate Systems*, DTIC Document, 2004.
- [80] X. He, T. Zeng, and M. Cherniakov, “Signal detectability in SS-BSAR with GNSS non-cooperative transmitter,” in *Proc. IEEE Radar, Sonar Navig.*, vol. 152, no. 3, pp. 124–132, 2005.
- [81] R. C. E. Gonzalez, S. L. Woods and S. L. Eddins, *Digital image processing using MATLAB*, McGraw Hill International Edition. 2004.
- [82] A. K. Katsaggelos, *Digital Image Restoration*, volume 23, Springer Series in Information Sciences, Heidelberg, Germany, 1991.
- [83] J. Kennedy and R. Eberhart, “Particle swarm optimization (PSO),” in *Proc. IEEE International Conference on Neural Networks*, Perth, Australia, 1995, pp. 1942–1948.
- [84] P. Massatt and K. Rudnick, “Geometric formulas for dilution of precision calculations,” *J. Navigation*, vol. 37, no. 4, pp. 379–391, 1990.